Fall 2019

Molecular Dynamics Study of Creep Deformation in Nickel-based Superalloy

Sabila Kader Pinky
Missouri State University, SabilaKader760@live.missouristate.edu

MOLECULAR DYNAMICS STUDY OF CREEP DEFORMATION IN NICKEL-BASED SUPERALLOY

A Master's Thesis

Presented to

The Graduate College of

Missouri State University

In Partial Fulfillment

Of the Requirements for the Degree

Master of Science, Materials Science

By

Sabila Kader Pinky

December 2019

MOLECULAR DYNAMICS STUDY OF CREEP DEFORMATION IN NICKEL-BASED SUPERALLOY

Physics, Astronomy and Materials Science

Missouri State University, December 2019

Master of Science

Sabila Kader Pinky

ABSTRACT

The present study employs molecular dynamics simulations of Ni-based superalloy to investigate the creep behavior under uniaxial compression test. Dislocation dynamics is analyzed for the nickel-based single crystal superalloy with the presence of void and with varying the distribution of gamma-prime phase The results show that multiple-void systems are more prone to yield than single-void systems and single-void systems are more prone to yield than the system without-void. From the simulations, it has been determined that the creep mechanism in Ni/Ni3Al is subject to change on the applied stress depending on the distribution of gamma-prime phases change. Dislocation behavior is also observed in addition to the time evolution of dislocation nucleation and growth to quantify the propensity and mechanism of creep in nickel-based single crystal superalloy. The studies confirmed that dislocation length prior to plastic deformation decreased as the number of voids increased. In addition, the deformation behavior for fine-grained nickel-based polycrystalline superalloy upon grain size variation is also investigated. Our findings show that both the movement mechanisms of the grains and grain boundaries and the relationship between grain size and yield strength are highly affected by the grain size of the materials. All the databases have then been classified to accurately predict the target class vi machine learning using the data mining tool WEKA.

KEYWORDS: creep, nickel-based superalloy, molecular dynamics, void, WEKA, gamma-prime, polycrystal

MOLECULAR DYNAMICS STUDY OF CREEP DEFORMATION IN NICKEL-BASED SUPERALLOY

By

Sabila Kader Pinky

A Master's Thesis
Submitted to the Graduate College
Of Missouri State University
In Partial Fulfillment of the Requirements
For the Degree of Master of Science, Materials Science

December 2019

Approved:

Ridwan Sakidja, Ph.D., Thesis Committee Chair

Kartik C. Ghosh, Ph.D., Committee Member

Tiglet Besara, Committee Member

Julie Masterson, Ph.D., Dean of the Graduate College

ACKNOWLEDGEMENTS

I would like to thank my advisor, Dr. Ridwan Sakidja for all his guidance, support and encouragement throughout this journey. I offer my sincere appreciation for the learning opportunities provided by all the faculties, and staff in the Physics, Astronomy and Materials Science Department. Many of my fellow graduate students in the department and all the group member of my research group deserve appreciation for their cordial help and support. Special thanks to my husband Abdullah Al Shafe for his constant encouragement and inspiration.

I am grateful for the support of DOE's National Energy technology laboratory (DEFE0031554) and for the computing support of the National Energy Research Scientific Computing Center (NERSC).

I dedicate this thesis to my father Golam Kader

TABLE OF CONTENTS

LIST OF FIGURES

INTRODUCTION

Nickel-Based Superalloy

Development of nickel-based superalloys began in the United States in 1930. This development process primarily involved determining the right alloying components with a workable manufacturing method. Throughout these studies, nickel-based superalloys include more than 10 alloy additions in the present time. Some alloys are for upgrading hot corrosion resistance (Si, Th, La, Co, Cr), some are for grain boundary strengthening (Cr, Nb, Ti, W, Mo, Hf, Ta) with carbides, for solid solution strengthening (Re, W, Fe, Co, Mo, Ta, Cr), for getting oxidation resistance (Ce, Y, Al, La, Cr), and as a boundary refiners (Hf, C, B, Zr). A third-generation nickel-based superalloy is Hynes 282, which is our prime focus in this dissertation, and below is the nominal composition of this alloy:

Nominal composition of Hynes 282 superalloy

Component (weight %)	Ni	Al	Cr	Co	Mo	Ti	Fe
Hynes 282	57	1.5	20	10	8.5	2.1	1.5

Nickel-based superalloys are quite popular as high-temperature materials already for several decades. They are primarily used for rotating turbine blades in the gas turbine engines or in jet engines. Because of the existence of two-phase γ/γ’ matrix–precipitate microstructure, Ni-based superalloys show excellent mechanical behavior even at high temperature. The crystal structures of γ and γ’ phases are FCC and L12, respectively. Figure 1 is a microstructure of a nickel-based superalloy. The main two phases are gamma (γ) and gamma prime (γ’) and both are

coherent with each other. The γ matrix phase primarily consists of pure nickel solid solution with around 0.1 um channel width, while the γ' precipitate phase is a coherent intermetallic Ni_3Al

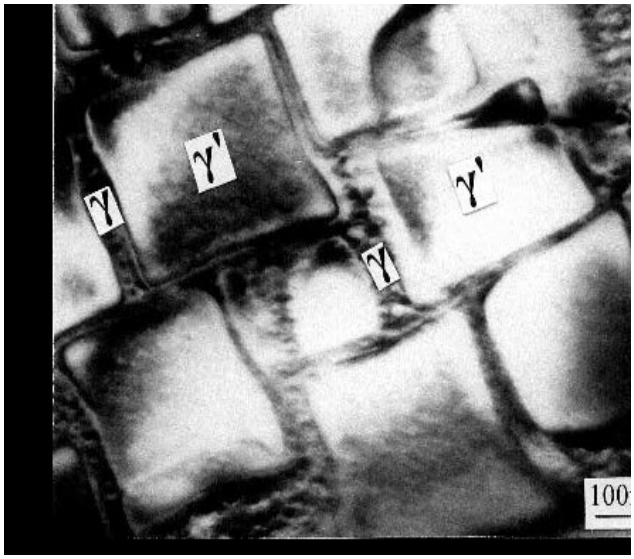

Figure 1 Microstructure of a nickel based single crystal superalloy

phase with around 0.5 um cube edge length separated by thin γ channels. The channels and edges of the cuboidal precipitates are oriented along <100> directions. The presence of the γ' precipitate phase in the γ matrix offers strengthening mechanisms for this system and contributes highly to improving the thermo-mechanical properties of Ni-based superalloys [1]. Advances in manufacturing engineering and the multitude of physical properties have made this alloy a reliable choice where a good creep resistance at high temperatures is required [2].

Creep Deformation

A very familiar fracture occurrence that is observed in the materials, which is exposed to a constant stress at high temperatures, is creep. Under mechanical stress, in most of the solid materials, creep effects are found. During creep, the non-linear performance is paramount in metal and the physical mechanism is clearly not similar from that in solids. This dissertation will

be discussing the creep of nickel-based superalloy, both single crystal and polycrystal and different factors that affect creep mechanism will be analyzed too.

In materials science, creep is defined as time-dependent strain, where solid materials deform slowly and permanently under the influence of constant mechanical stress which is lower than the yield point. It is an irreversible and permanent deformation process. Excessive temperature also triggers the rapid increase of a high creep deformation. At the temperature of about one-third to one-half of the melting point of metals, a noticeable creep behavior can be observed. Figure 2 is illustrating a typical creep curve for metals. In a continuous process of creep, three stages are present: primary stage, secondary stage steady-state creep and tertiary creep. Primary creep stage is generally explained as a transforming stage, secondary creep stage as the functional lifetime and tertiary creep stage is the predecessor to final rupture. The

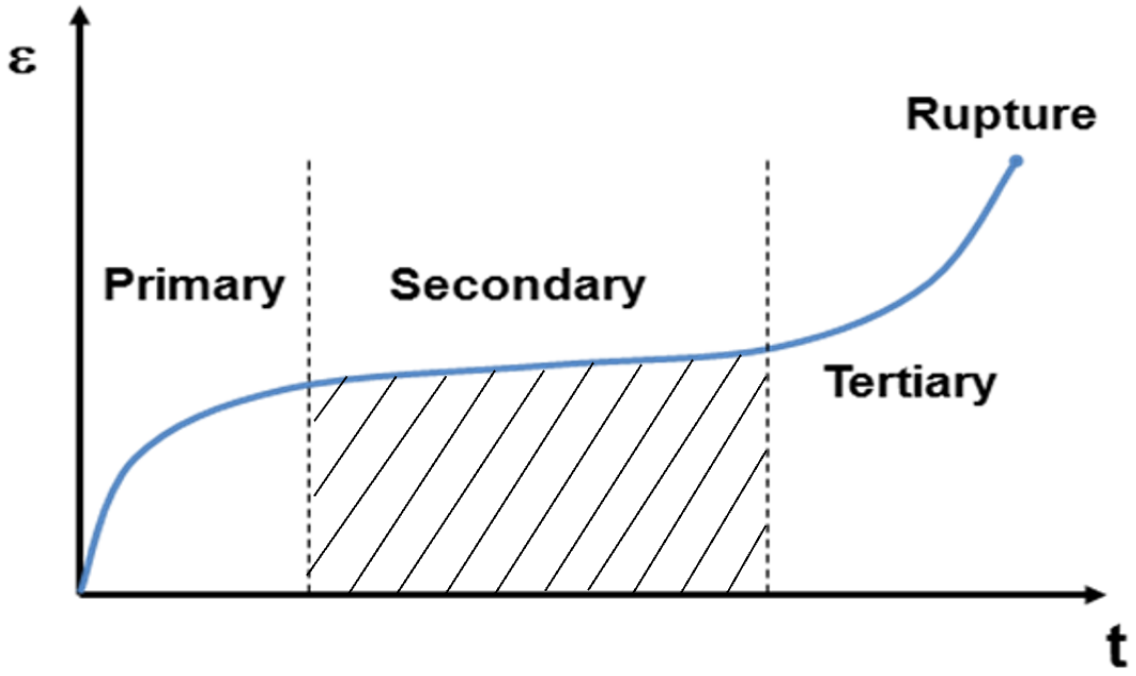

Figure 2 A typical strain vs time creep curve

deformation rates are also not the same at all three stages. Initially, the strain rate decreases with

time when the material is at the primary stage; we will find an almost constant strain rate at the steady-state stage, and the creep rate at the tertiary stage increases at a very fast rate with time till the material ruptures finally. The secondary stage (steady-state creep) is the longest segment of its life in this region, hence is of prime interest to researchers. To estimate the time for a material to reach a certain deformation stage, and to know when the material becomes unstable before it fails completely, the understanding of the creep and creep rate will be of most importance. However, knowing the creep rate will allow us to estimate the lifetime already spent by the materials, thus they can be substituted before the unrecoverable destruction takes place.

Creep Property of Nickel-Based Single-Crystal Superalloy

During operation, Ni-based superalloys are usually exposed to high cyclic loads at elevated temperatures. Therefore, enough damage-tolerance evaluation of components requires reliable knowledge of their mechanical properties, where the morphology of the dislocation network growth plays an important role. Moreover, the intricate behavior of dislocation networks under various loading conditions requires more attention. Nevertheless, these dislocation networks enhance the creep resistance by preventing the matrix dislocation from cutting into the γ’ precipitate, hence increase the strength of the interface [3]. In fact, the corresponding parameters are determined by the microstructure. So, a comprehensive knowledge of the underlying microstructure–property relations are required to control the creep rates. However, creep is characterized by time-dependent plastic deformation exhibiting a nonlinear dependence on stress (power-law) and temperature (Arrhenius relation). And an investigation of these characteristics is difficult on both the level of macroscopic scale and the level of the dislocation and phase microstructure. However, the exceptional creep resistance behavior is the most

beneficial mechanical property of nickel-based superalloys. This specific property of the superalloy prioritizes them while choosing a material with excellent structural integrity in a high fatigue environment in conjunction with high temperatures. Two factors are playing a prime role behind this high creep resistance: one is the solid solution and precipitation strengthening of the two phases – gamma (γ) and gamma prime (γ'), and another one is the control of grain size and shape.

Deformation Mechanism in Nickel-Based Polycrystalline Superalloy

Polycrystalline materials have a huge dissimilarity in deformation behavior than single-crystal materials overall. According to the Hall-Petch relationship, polycrystalline materials have high strength and low ductility. It is their low hardening rate that inhibits substantial plastic deformation via strain localization. For polycrystalline materials, different types of deformation mechanisms have been demonstrated by the researchers [4]. Some of them are:

- Grain-boundary dislocation annihilation.
- Gradient models.
- Pile-up breakdown.
- Grain-boundary rotation and grain coalescence.
- Core and mantle effect.
- Shear band formation.
- Grain-boundary sliding.
- Twinning.

During the compression simulations in nickel-based polycrystalline superalloy under high pressure-high strain rate exhibits highly localized plastic deformation and the evolution of nano-grains inside the material because of the introduction of voids. Later, these voids serve as dislocation sources while grain formation happens. As the porosity decreased, the combined interactions between these two factors assist in the production of very high dislocation density, hence they reduce the dislocation velocities [5].

Effect of Microstructure on Creep

Studies have found that creep behavior of nickel-based superalloy differs in a large amount with the change in microstructure, i.e. single crystal and polycrystal superalloy. Nevertheless, grain boundaries have an exceptionally large influence on the creep mechanism of any materials. In fact, primary and steady-state creep rates in polycrystalline nickel-based superalloys can be brought down by increasing the frequency of grain boundaries, where grain size fulfills the Hall-Patch range [6]. However, the material with grain size less than the range will exhibit a high deformation rate with increasing the frequency of grain boundary. This takes place because due to the presence of a very high volume of atoms into the grain boundary that increases grain boundary sliding [6]. Additionally, the active creep mechanisms and the creep rate can be affected by the volume fraction of secondary γ' precipitates. Unocic et al [7] demonstrated that the favorable condition for the grain boundary shearing mechanism is the low volume fractions of secondary precipitates. However, Locq et al [8] claimed that alloys show faster creep rates when they have a higher volume fraction of secondary γ' phases due to the process of climb by-pass as the operative mechanism. Also, lengthening the creep test time can reckon with precipitate coarsening, hence can alter the active mechanism as well [7].

Another key factor that can have a large effect on the creep life of superalloys is the high-stress or high-strain and temperature and can alter the deformation substructure and mechanism. Explicitly, a different values of high-stress or high-strain in polycrystalline alloys can produce planar or non-planar mechanisms with different dislocation dynamics [9].

Literature Review

Considerable prior work [10]-[50] on modeling and simulation of dislocation dynamics have been carried out in the last 50 years, which showed that the creep mechanism is closely related to the evolution of the interfacial dislocation networks. Depending on the initial phase of void growth and crack nucleation, recent investigations of fracture propagation have employed different methods, such as the crystal plasticity finite element [10]–[15], and dislocation dynamics and molecular dynamics [16]–[25]. Also, the primary mechanism of the creep deformation of Ni-based superalloys are well-studied, i.e. dislocations inside the channels [26]–[28], dislocation networks formation around γ' cubes [29], [30], misfit stresses [31]–[33] and the cutting of γ' particles by dislocations [34]–[37]. Also, there are numerous work concentrating on the factors that affect the creep behavior in nickel-based superalloys, for example, volume fraction and size of γ' phase [38]–[40], effect of crystal orientation [38], [41], [41]–[47], varying the temperature and/or stress [39], [42], [43], [48]–[50] including directional γ' coarsening or rafting.

Comparatively some of these studies concentrate on the void growth phenomenon. Furthermore, the modeling of void interaction between neighboring voids has received less attention than void growth. But only limited efforts were made to analyze dislocations in the γ' phase, rather the prior studies had been focusing primarily on the role of cube size and shape. Void coalescence has the most pronounced effect on the deformation of the material concerning the interaction of defects [10], [25]. Although investigation of void coalescence has been done only for tensile stress, there is no significant study on the creep behavior of Ni-based superalloy under compression. Notably, structural evolution has been studied successfully at an atomic scale using MD simulation which includes dislocation motion and atomic diffusion [51], [52]. Hence,

MD simulation of void coalescence provides vital functionality over larger scales of modeling. Considering the above facts, our present study employs MD simulations to investigate void growth and coalescence behaviors for different conditions under uniaxial compression to study creep deformation in Ni-based superalloy.

Outline of Dissertation

The main mechanism inside a crystalline material, that is under extreme environment, to locally relax the stresses of the entire body induced by deformation, is the dislocations evolution. In the case of polycrystalline and nanocrystalline structures, dislocations emanate from grain boundaries and grain junctions. However, depending on the orientations of adjacent grains in polycrystalline material, dislocations alter direction and plane. There needs to be a systematic statistical study to evaluate the effect of different dislocation multiplication rate and/or dislocation annihilation rate when they run into each other. Therefore, summarizing these statistics will help to predict the time at which time the failure is more likely to occur. Since, the creep deformation is a time-dependent phenomenon, getting a huge amount of information is only possible with molecular dynamics (MD) simulations. Alternatively, simulations deliver complete information about how the evolution of microstructure morphology and stress generates inside the material, including resolved tensorial stress and strain on the microstructure scale, and the initiation and propagation of dislocations. In this case, molecular dynamics (MD) have become very helpful tools for analyzing the morphology and growth of the dislocation networks under different conditions at the atomic level. As a result, the atomistic view of exploring the correlation between the evolution of dislocation networks and the mechanical properties of alloys has become easier [3], [53].

COMPUTATIONAL APPROACH

Structure Generation

A microstructure-sensitive crystal-plasticity-based model has been developed in this work to comprehend the deformation behavior of Ni-based superalloys at different temperatures and physical conditions. We have used the Atomsk [54] command to create and manipulate our structure. Atomsk is an open-source command-line program dedicated to the creation, manipulation, and conversion of data files for atomic-scale simulations. Atomsk provides options to create single crystal, bicrystal, and polycrystal structures with the predefined angle, position, and length. Figure 3 is the 3D view of both single crystal Figure 3(a) and bicrystal Figure 3(b) supercell. Blue region is the pure Ni with FCC crystal structure, which is called γ phase. And red cubes inside the γ-phase are called γ'-phase, which are Ni_3Al. In Ni-based superalloy, γ-phase is

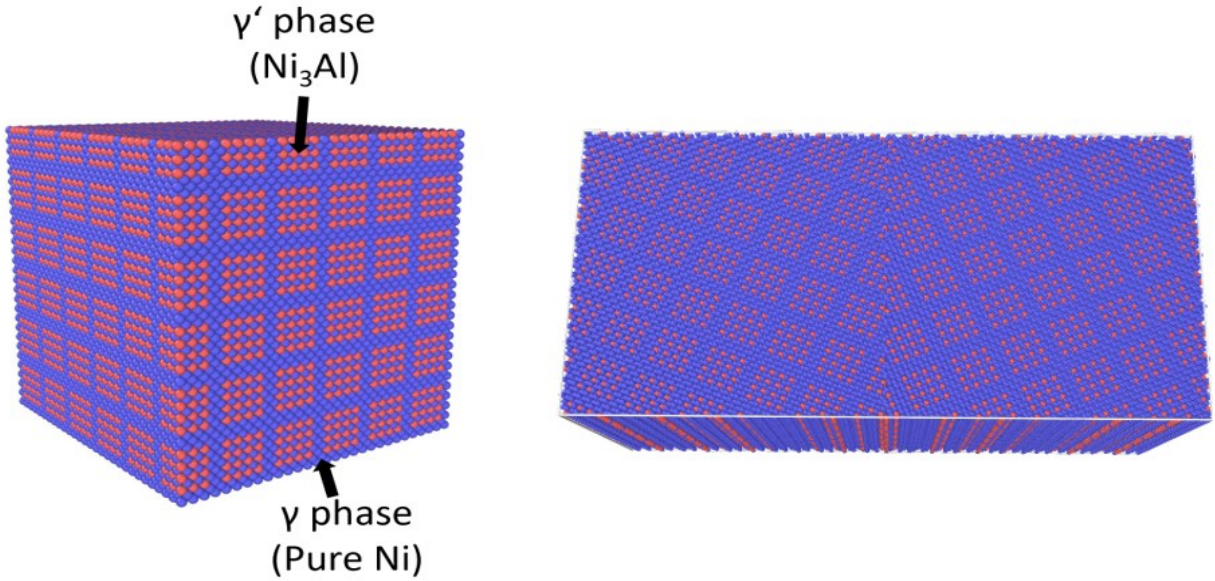

Figure 3 Schematic view of supercell (a) single crystal (b) bicrystal

the soft or weaker phase, whereas γ'-phase is the hardest phase that is mainly responsible for the high strength of superalloy.

Figure 3(a) is a periodic single-crystal structure containing 108,000 atoms with 216 γ'-nanophase cubes. The volume fraction between these two phases is 51%, which is standard for commercial Haynes 282 alloy. While producing the bicrystal [Figure 3(b)] we used our single-crystal supercell as a unit cell and created bicrystal with 15^0 grain boundary mismatches. This bicrystal supercell contains 212,910 atoms which are not exactly double of the single crystal supercell because all the overlapped atoms (due to the mismatch in grain boundary) have been removed.

For the later part of the work, polycrystalline supercell [Figure 4] had been created using Atomsk. To develop our model, we have used our single-crystal supercell as a unit cell and kept all the grains random without mentioning grain angle alignment or grain size. Our polycrystal supercells contain 311,000 – 338,651 atoms (depending on the no. of grains and grain size) with a box size of 160Å x 160Å x 160Å, that makes them ultra-fine grain nano-polycrystal ranging

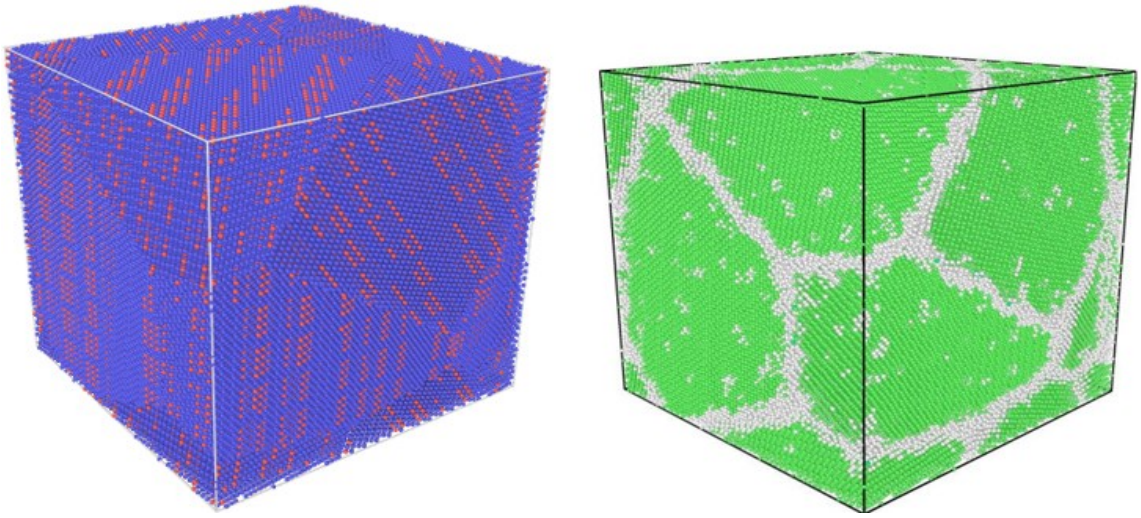

Figure 4 Schematic view of polycrystal supercell

grain size from 16nm to 5nm. Also, after creating the polycrystal supercell, we deleted all the overlapped atoms (due to the grain boundary mismatches) to make the structure stabled.

Energy minimization

Ni-based superalloy is mainly comprised of two types of phases – γ-phase and γ'-phase, where γ'-phase (Ni_3Al) is an ordered FCC structure with both Nickel and Aluminum present. Because of the different atomic size (refers lattice mismatch) a local strain is produced inside the material. Also, a local strain can be introduced inside the model while packing the individual grain into the bicrystal configurations or polycrystal structures. This local strain can interfere with our global strain given to the model while doing the compression test through MD simulation. Therefore, removing the local strain inside the model is essential to get a bias-free output depending solely on the given parameters only. In order to accurately analyze the properties, we have done the energy minimization [Appendix A.1] at 0K to adjust atom coordinates in local potential energy minimum.

The minimization algorithm is the total potential energy of the system as a function of the N atom coordinates:

$$E\ (r_1,\ r_2,\ \ldots.,\ r_N) = \sum_{i,j} E_{pair}\left(r_i, r_j\right) + \sum_{ij} E_{bond}\left(r_i, r_j\right) + \sum_{ijk} E_{angel}\left(r_i, r_j, r_k\right) + \sum_{ijkl} E_{dihedral}\left(r_i, r_j, r_k, r_l\right) + \sum_{ijkl} E_{improper}\left(r_i, r_j, r_k, r_l\right) + \sum_{i} E_{fix}\left(r_i\right)$$

Where the first term is the sum of all non-bonded pairwise interactions including long-range Coulombic interactions, the 2nd through 5th terms are bond, angle, dihedral, and improper interactions respectively, and the last term is energy due to fixes which can act as constraints or apply force to atoms, such as through interaction with a wall. See the discussion below about how fix commands affect minimization.

Simulation

An uniaxial compression test [Appendix A.3] was performed by Large-scale Atomic/Molecular Massively Parallel Simulator (LAMMPS) [55] for all the systems throughout the research. All simulations were performed at a constant strain rate of 5×10^{9} s^{-1} and a Nose–Hoover thermostat [56] was applied to maintain the system temperature at a constant value. Periodic boundary conditions were applied in three directions of the simulation box. Before applying the compressive load, a full relaxation was performed to the system. To lower the stress level the systems were equilibrated for 200 ps with a constant time step of 1 fs under an NPT ensemble. This equilibration step allows the lattice to expand at each simulation cell boundary to a temperature of 300 K with a pressure of 0 bar. Then, the simulation box is exposed to an applied constant engineering strain-rate in the x-direction, while the lateral boundaries are controlled to zero pressure using the NPT equations of motion.

In MD simulations, this strain-rate control is understood by atoms to move via allowed transformation. At this circumstance, an atom at a position $r_i = (x, y, z)$ in the system is relocated by a constant velocity in a given time-step before merging the dynamic equilibrium equations. At the same time, the pressure in the x and z directions are kept fixed to $p_x = 0$ and $p_z = 0$ by an NPT canonical ensemble to perform uniaxial compression. The following formula is used to calculate strain in the direction of the applied stress:

$$\varepsilon = \frac{l - l_0}{l_0}$$

Here l is the instantaneous length of the cubic sample under applied compressive stress and l_0 is the initial length of the cubic sample. Stress is calculated using virial theorem [57].

Atomistic simulations were performed using the embedded-atom method (EAM) since our focus is in metal and for this form of inter-atomic potential which adopts the functions that

describes both the electron gas and the pair potentials has been found to be the most suitable form of potentials for metallic systems. In our study, we have used the embedded-atom method (EAM) potential developed by Mishin et al. [58] to simulate the uniaxial compression behaviors for all the systems of Ni-based superalloy. This potential has been proven good for having accurate information to represent bonding in metallic systems and considering strength dependency of individual bonds on different features i.e. surfaces, defects, and extreme environment. Hence, it is expected that this potential will allow fair MD simulations of the uniaxial compression test. Moreover, this EAM can recreate almost all necessary material properties and is based on first-principle calculations. Numerous studies [31], [59]–[61] have been made to look into the deformation behavior using this EAM potential, making this a reliable potential to use.

Analysis

Analysis in research papers is necessary to present a comprehensive study with necessary proof on the specific topic. The purpose of our present research thesis is also to learn and gather information on our topic of interest. To fulfill our purpose, we have used a number of tools to analyze all the output data to find out a synchronized information on the dislocation dynamics in Ni-based superalloy. The open visualization tool (Ovito) developed by Stukowski [62] was employed to observe and analyze the atomic configuration throughout the uniaxial compression of the system. The local atomic structures were identified by Common Neighbour Analysis (CNA) [63], also for observing the evolution of slip bands, partial dislocations, and stacking faults during MD simulation. The Polyhedral template matching (PTM) by Larsen et al. [64] was applied for highlighting defective atoms, and the local structural environment of particles. The

PTM approach is reliable in the presence of high strain and provides a direct calculation of the local (per-atom) orientation, elastic deformation, strain, and alloy type. The slip system can be distinguished by adjusting the centrosymmetry parameter [65]. This parameter is useful to measure the local lattice disorder around an atom and can be used to characterize the atom of dislocation or stacking fault. However, dislocation analyses were also carried out using the Dislocation extraction algorithm (DXA) integrated into the Ovito software [63]. This analysis modifier identifies all dislocations in a crystal with their Burgers vectors, and represent them as a line.

RESULTS AND DISCUSSION

Creep Deformation in Nickel-Based Single Crystal Superalloy

As the microstructure of these alloys are made of primary γ matrix with embedded secondary γ′ precipitates, the stress-strain, as well as the creep deformation behavior at different physical conditions and environment, depend upon the microstructural features. The mechanical behavior of these alloys is sensitive to volume fraction, shape and size of the precipitates, defect types and amount, and their resistance to the dislocation motion.

In this work, compression tests were performed to analyze dislocation dynamics towards the creep deformation of nickel-based superalloy varying different parameters. Figure 5(a) shows the stress-strain curves of γ/γ' monocrystal superalloy under compression testing at room temperature with a constant strain rate of $5X10^{11}$ s^{-1}. The stress-strain curve shows that the yield stress of γ/γ′ monocrystal of superalloy has reached to 4.73 GPa as the strain reaches the level of 7.8%. Before the system reaches into yield strain, the γ/γ' monocrystal of nanophases is mostly in the elastic region. With the strain increases from 7.8% to 10.0%, the stress-strain curve decreases abruptly, hence the structure undergoes plastic deformation. After 10% strain, the stress-strain is quite linear, so the γ/γ' monocrystal appears to be steady after the plastic deformation.

The microstructural evolution was investigated by CNA with the strain amplifying in γ/γ' monocrystal under compression testing at room temperature [Figure 5(b)]. Here, the structural information was used to detect the slip plane from the system. The green presents atoms with FCC structure, whereas the red denotes the atoms with HCP structure indicating the shearing slip bands, as shown in Figure 5(b). During the compression process, the stress-strain curves exhibit

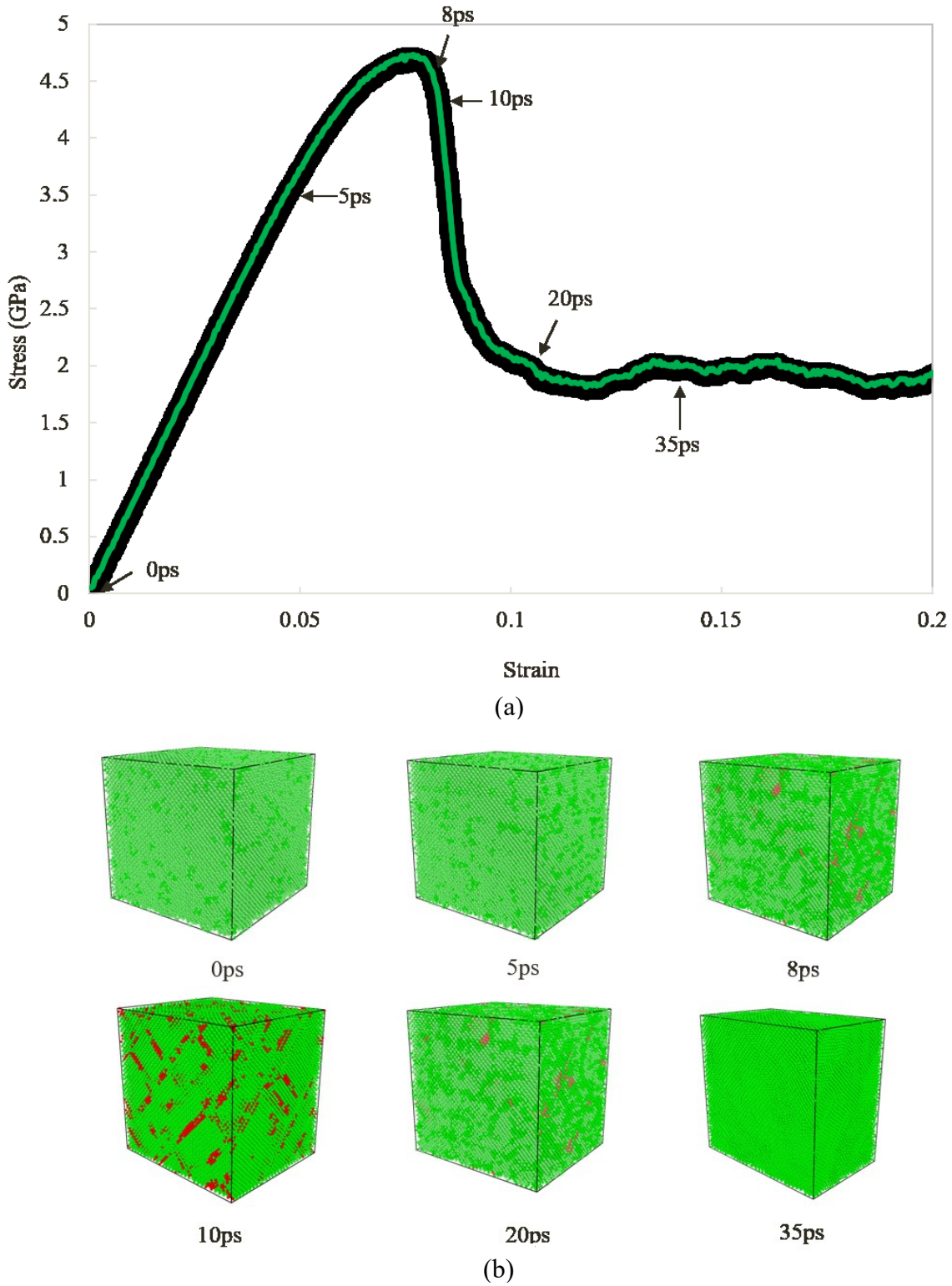

Figure 5 (a) Stress-strain curve at 300K; no void; 216 γ' cubes; single crystal (b) structural analysis in comparison with the stress-strain curve at different time

a significant elastic stage prior to dislocation nucleation (0ps and 5ps).

Dislocation nucleation is responsible for stress relaxation and stress redistribution. Therefore, at 8ps dislocation nucleation starts and the sample enters a period of plastic deformation, and the dislocation density grows, while the stress continues to decrease with increasing strain loading [10ps; 20ps]. Once the deformation is complete, a further hypothetical compression would lead to a potential disintegration of the crystalline structure which is beyond the scope of the analysis.

Effect of Strain Rate

Strain rates are found to affect the yield stress in single crystals superalloy. We have varied strain rate from $5X10^{9}$ s^{-1} to $5X10^{7}$ s^{-1}. Analyzing the stress-strain curve in Figure 6 we found that with decreasing strain rate yield stress of the system also decreases. Moreover, the deformation of the system starts earlier when the system is under compression at a lower strain rate. This takes place because the strain rate can be correlated with the dislocation velocity. When applying compression at large strain rates, micro-voids and dislocation nucleates inside the material and the single crystals start to deform plastically. However, a lower strain rate allows enough time for the diffusion-controlled dislocation process to counteract the effects of strain hardening. Also, dislocation has enough time for acceleration, resulting in a minimal deformation resistance. While the system undergoes deformation at a higher strain rate, the acceleration which the dislocation needs will also be increased, hence the dislocation will meet the obstacles and will increase the resistance of dislocation motion.

We should mention here that, on the other hand, applying strain rate very high is not always an effective way to get very high yield stress, because a very high strain rate beyond the

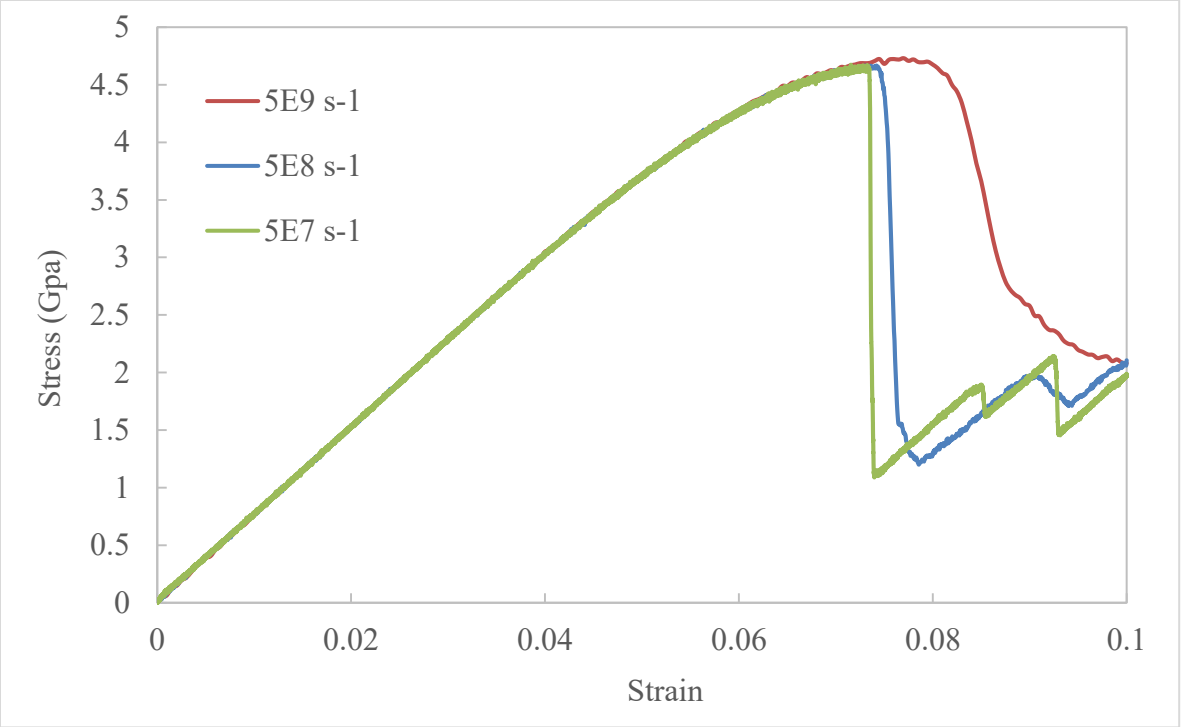

Figure 6 Stress-strain curve for single crystal nickel-based superalloy with 216 γ' nanophases for different strain rate at 300 K

limit will cause the instant deformation and tear inside the system. The sample may deform before it enters the plastic region due to the sudden shock of compression.

Effect of Temperature

While doing the compression test at high temperature, thermal stress may accumulate inside the sample and can relax later under compression by additional processes and can contribute to our creep calculation. Therefore, it is important to minimize thermally induced stresses inside the material by equilibrating the system at high temperature to reduce the thermal expansion mismatch. It is common that most materials expand while heating and shrink while cooling. During the expansion of materials, the change in length of the sample with temperature can be calculated by using the coefficient of linear thermal expansion (CTE) $\overline{\alpha}$:

$$\overline{\alpha} = \frac{l - l_0}{l_0 (T - T_0)}$$

Where l_0 is the initial length of the sample at initial temperature T_0, which is generally room ambient (300 K) and l is the expanded length of the sample at temperature T. The coefficient of thermal expansion (CTE) can also be expressed as the fractional increase in length per unit temperature increment:

$$\overline{\alpha} = \frac{1}{l}\frac{dl}{dT}$$

Where l is the expanded length of the sample at temperature T.

Lattice parameter measurements are presented as a function of temperature in Figure 7 before the compression test was done. The slope of tangent in the fractional length change versus temperature plot gives the thermal expansivity $\overline{\alpha}$. Slope of the curve in Figure 7 determines the coefficient of thermal expansion (CTE), which is $1.9X10^{-5}$ $/^0K$, however, the reference CTE for Hynes 282 at 1000K is $1.7X10^{-5}$ $/^0K$ [66]. This value complements our next work by proving that the lattice mismatch between two phases of nickel-based superalloy has no effect here at all.

The two main phases of our nickel-based single crystal superalloy sample are γ-phase (Ni) and γ'-phase (Ni_3Al). The ordered γ' phase (Ni_3Al) stays off-stoichiometric variations within a limited concentration band. Fortunately, the effect of Al on the CTE of nickel-based superalloy has been studied by several authors [67]. These studies report that the addition of the most common alloying elements decreases the CTE of Ni, with the exception of Fe and Mn. The thermal expansion coefficients differ in an order with $CTE_{Ni} > CTE_{Ni3Al}$. These variations in thermal expansion of Ni state that when the atomic volumes of the atoms in the alloy are close enough, only then the simple rule of mixtures work best. We should note that, however, the CTE of a material can also be influenced by some other factors such as grain size, homogeneity, and crystalline texture.

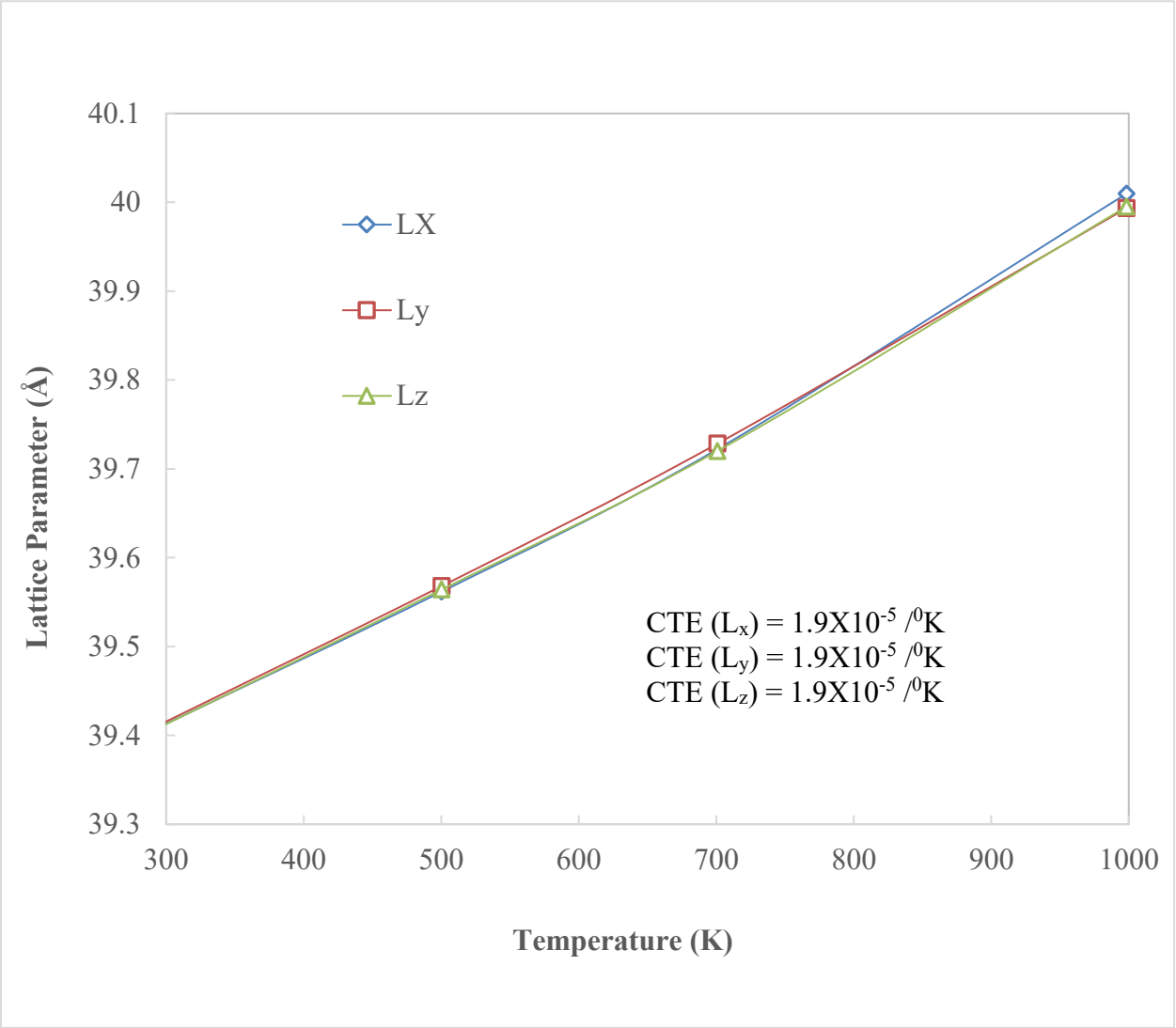

Figure 7 Coefficient of thermal expansion of nickel-based single crystal superalloy at high temperature

Figure 8 is showing the volume expansion of the lattice parameter of our sample with temperature from ambient temperature 300K to an elevated temperature of 1000K. During the equilibration lattice parameter of the system in all three directions exhibits similar increases as the temperature increased, confirmed that the lattice mismatch of γ and γ' phases are not affecting our further process.

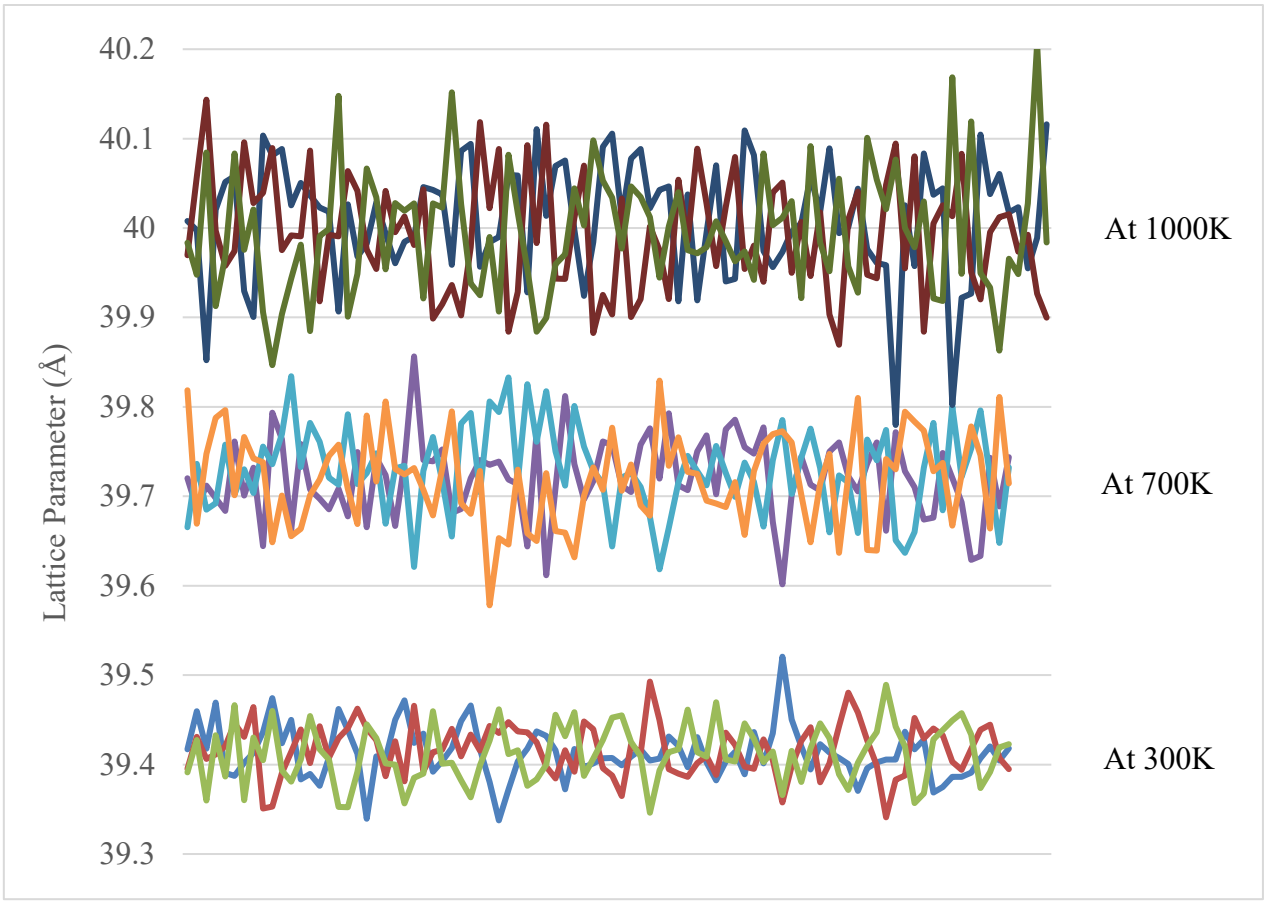

Figure 8 Volume expansion of nickel-based single crystal superalloy at different temperatures

With increasing temperature materials yield strength decreases and the strain value at which dislocation starts to nucleate also decreases, which means that at higher temperature materials deformation takes place very earlier than at room temperature. Figure 9 is presenting the stress-strain curve of nickel-based single crystal superalloy at 300K, 700K and 1000K, with a starting point of a downward trend at 8%, 7.5%, and 7% strain respectively. At higher temperature reduction of strain hardening is observed due to the softening mechanism i.e. dynamic recovery and thermally activated climb of dislocation, which enables overcoming of the obstacles for dislocation motion that was not possible otherwise at a lower temperature. The softening of the γ' phases together with the reducing strength of γ-phase at high temperature leads to the decrease of yield strength.

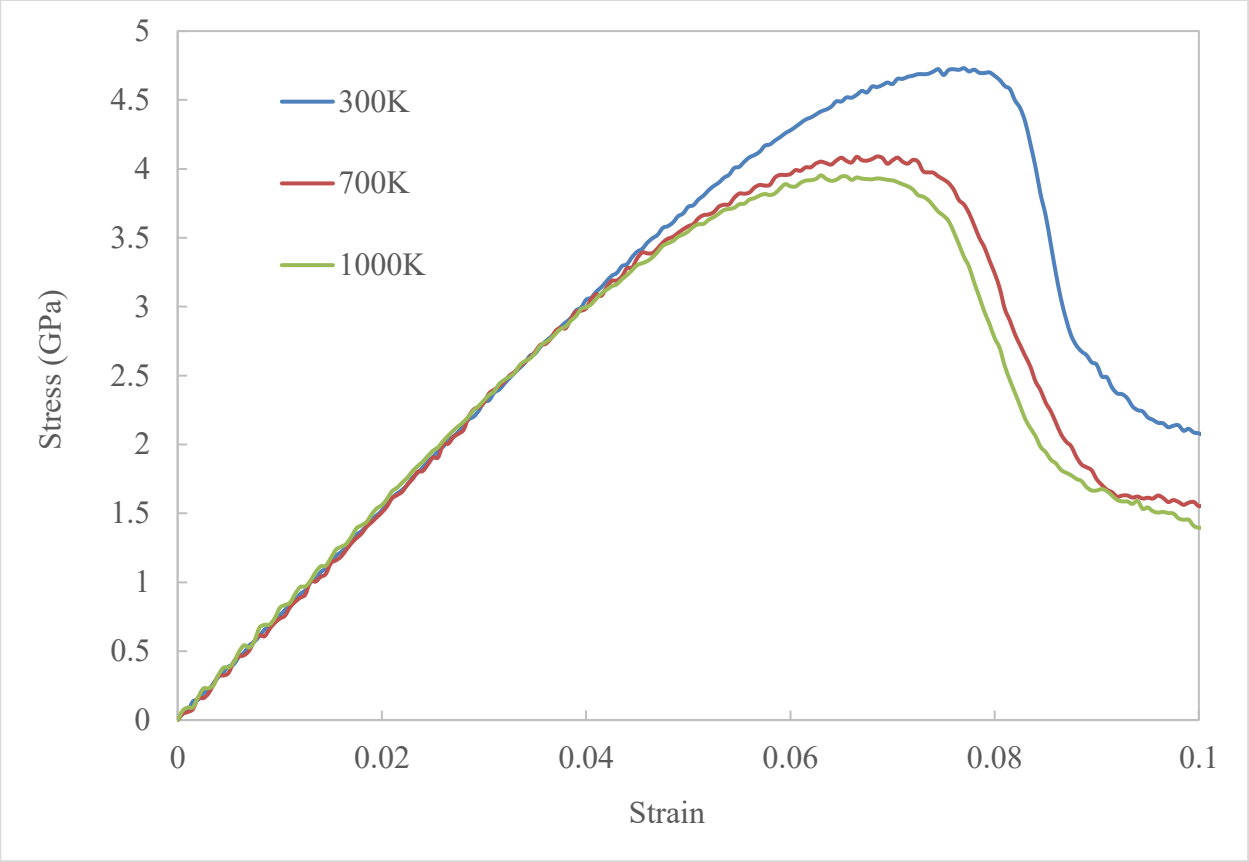

Figure 9 Stress-strain graph at different temperature for single crystal sample with 216 γ' nanophases

Effect of Void

Several studies have indicated that the addition of void considerably affects the yield strength and dislocation dynamics of the sample [68], [69]. To study the effect of void on dislocation behavior and the mechanical properties of monocrystal Ni-based superalloy, the stress-strain curves have been analyzed. The stress-strain plot in Figure 10 summarizes the difference amongst the mechanical properties of the sample without any void, sample with one void and sample with multiple voids. Therefore, definite differences are noticed from the stress-strain curves, such as single-void systems are more prone to yield than no-void systems, and the multiple-void systems are more prone to yield than single-void systems. Also, adding void(s)

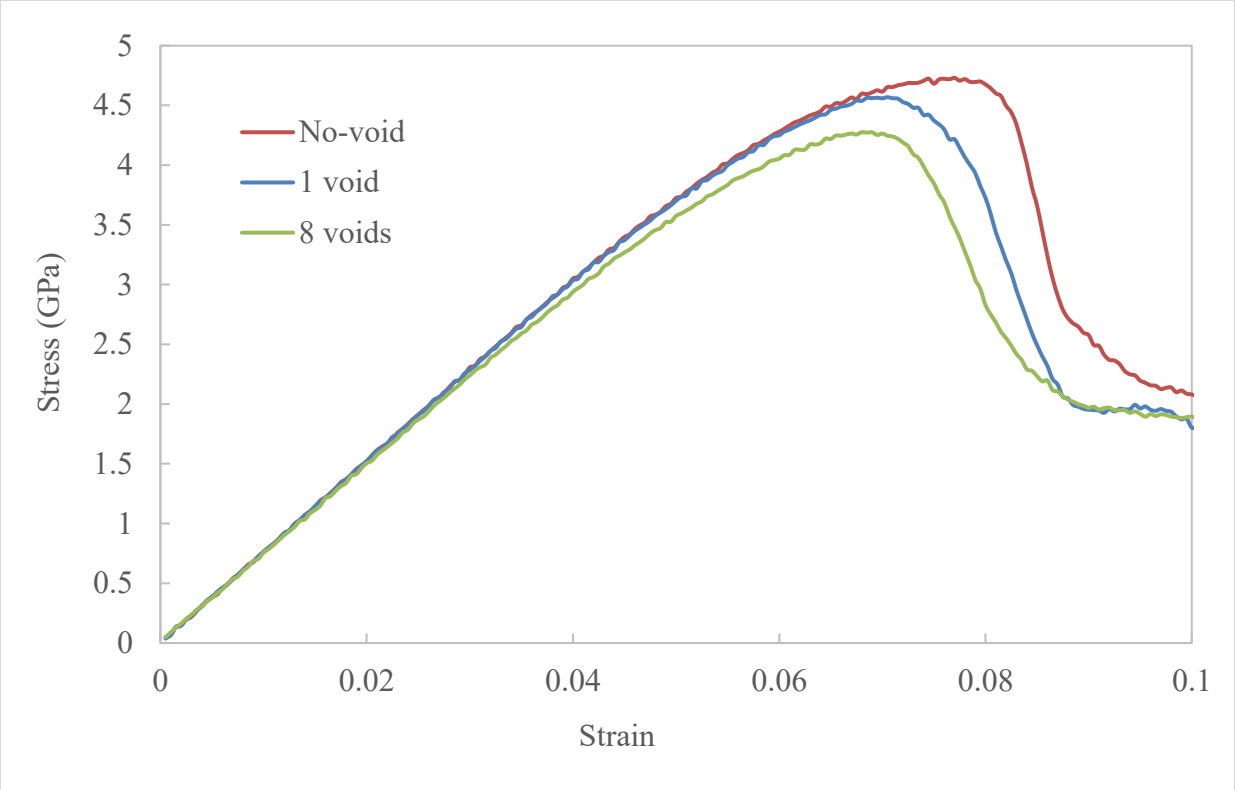

Figure 10 Stress-strain curve showing the effect of the presence of void

into the system lower the strain value, when dislocation appears, and yield stress starts to decrease. This phenomenon indicates the timing of the nucleation of dislocation inside the system. It is evident that dislocation nucleation is fastest when there are multiple voids present inside the system comparing to the other two different systems.

Dislocation nucleation and propagation. Figure 11 exhibits dislocation evolution and propagation with and without void inside the system. A surface atom has fewer neighboring atoms due to losing some neighbor atoms and electronic density, resulting in fracture of some atomic bonding and experiences fewer attractive interaction forces from its surroundings than an atom inside of the bulk. This consequence in the relaxation motion of atoms near and inside the surface and damages the balance of these atoms, which then reduces the total potential energy of the system [70]. Therefore, the earliest movement of atoms become easy to begin in the free surface,

resulting the free surfaces of the voids serve as the sites of the initial dislocation nucleation [Figure 11(b), Figure 11(c)] and the dislocation emerge and grow by a semicircular shear loop [71], [72]. When there is no defect or void inside the sample, dislocation can start from anywhere, generally, nucleates from the surface of the sample or from the γ/γ′ interfaces [Figure 11(a)].

The dislocation nucleation begins relaxation of the stress around the void, which is indicated as stress redistribution at a macroscopic scale. Surfaces in bulk materials form a

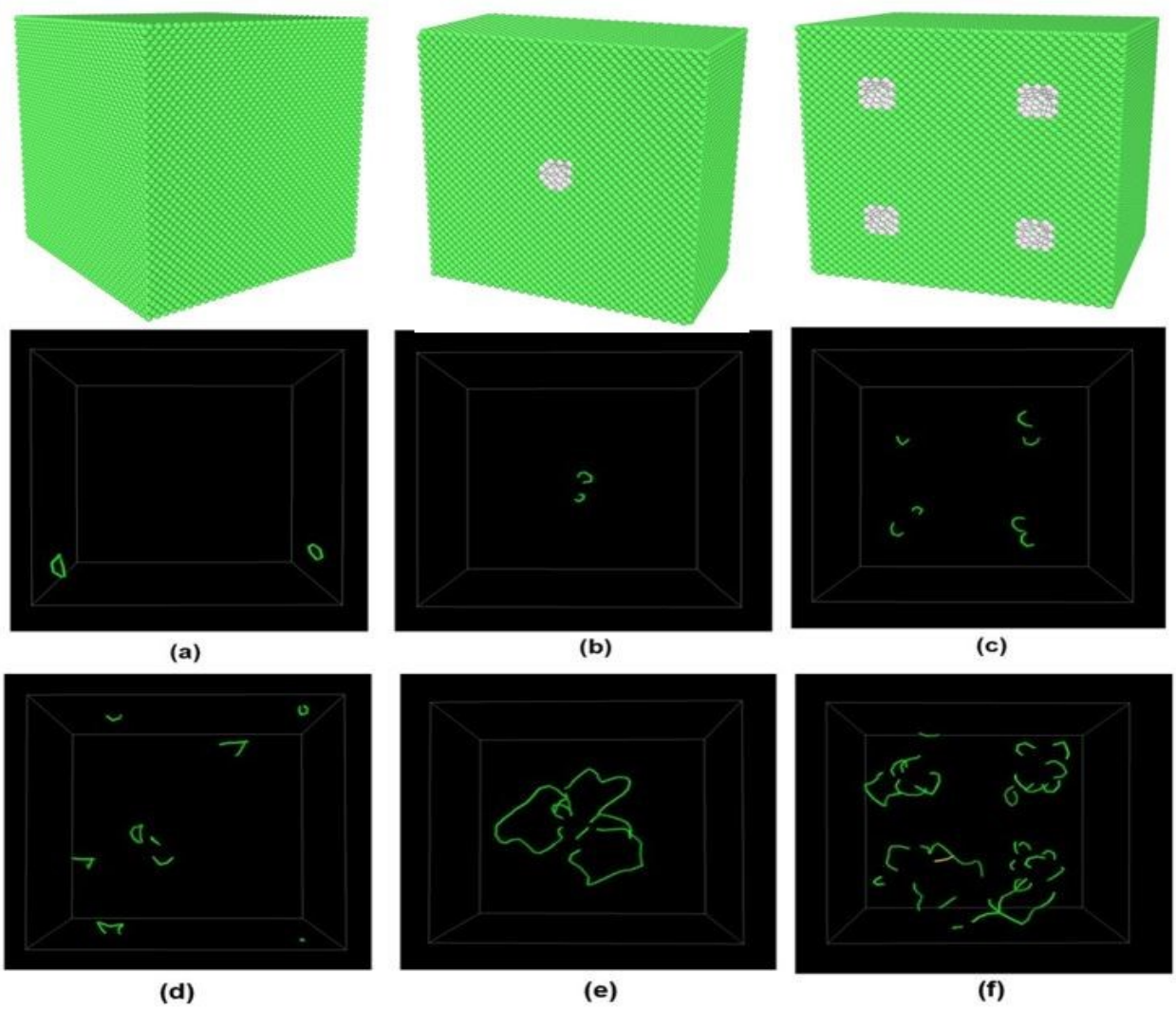

Figure 11 Snapshot of dislocation nucleation inside sample with 216 γ' cube at 300K with (a) no void, (b) 1 void, (c) 8 voids (d) Dislocation density after 4ps of nucleation with no void, (e) after 4ps of nucleation with 1 void, (f) after 4ps of nucleation with 8 voids

minimal fraction of the total volume, and the reaction of surface energy is inconsiderable. But for the nano system surface effect contributes a significant part into the system. With further loading, the dislocation starts to grow, and the dislocation length increases remarkably around the void surface [Figure 11(e), Figure 11(f)]. For the system with no void or defect inside the system, dislocation grow randomly without following the semi-circular loop [Figure 11(d)]. To see the change in dislocation density, analysis of the dislocation density evolution has been done around the voids during the overall simulation process. The analysis unveils that the dislocation density near to the voids is large, further confirming that the dislocation source comes from the free surfaces of the voids and is extended by the semi-shear dislocation loop. During the initial deformation stages, no apparent involvement is observed between the voids. Nevertheless, an inter-void interference effect can be observed after a period of loading, where local deformation of the voids might be observed.

Stress-strain curve and Dislocation length-strain curve. An overlapping plot of the stress-strain response curve and dislocation length-strain curve has been presented in Figure 12. In the stress-strain curve, the stress goes up almost linearly with increasing strain in the elastic deformation region prior to the dislocation initiation with no lattice distortion. The maximum stress in the stress-strain curve is defined as the initial yield strength [18]. Beyond this point, the sample into the yield stage starts to plastic deformation. The stress value at 7.8% strain for our sample is the yield section. Plastic deformation of material follows the following relationship:

$$\varepsilon = b\rho v$$

$$v = \left[\frac{\tau}{\tau_0}\right]^m$$

ε = The plastic strain rate of the material

ρ = Movable dislocation density in materials

ν = Dislocation movement rate

b = Burgers vector

τ = Shear stress acting on the slip plane

τ_0 = Reference shear stress

m = Stress sensitive factor

The above formula proves that to increase the velocity of dislocation, high stress is a must. Also, shows the relationship between yield phenomenon and dislocation movement. The dislocations multiply in a huge number after the plastic deformation of the system begins,

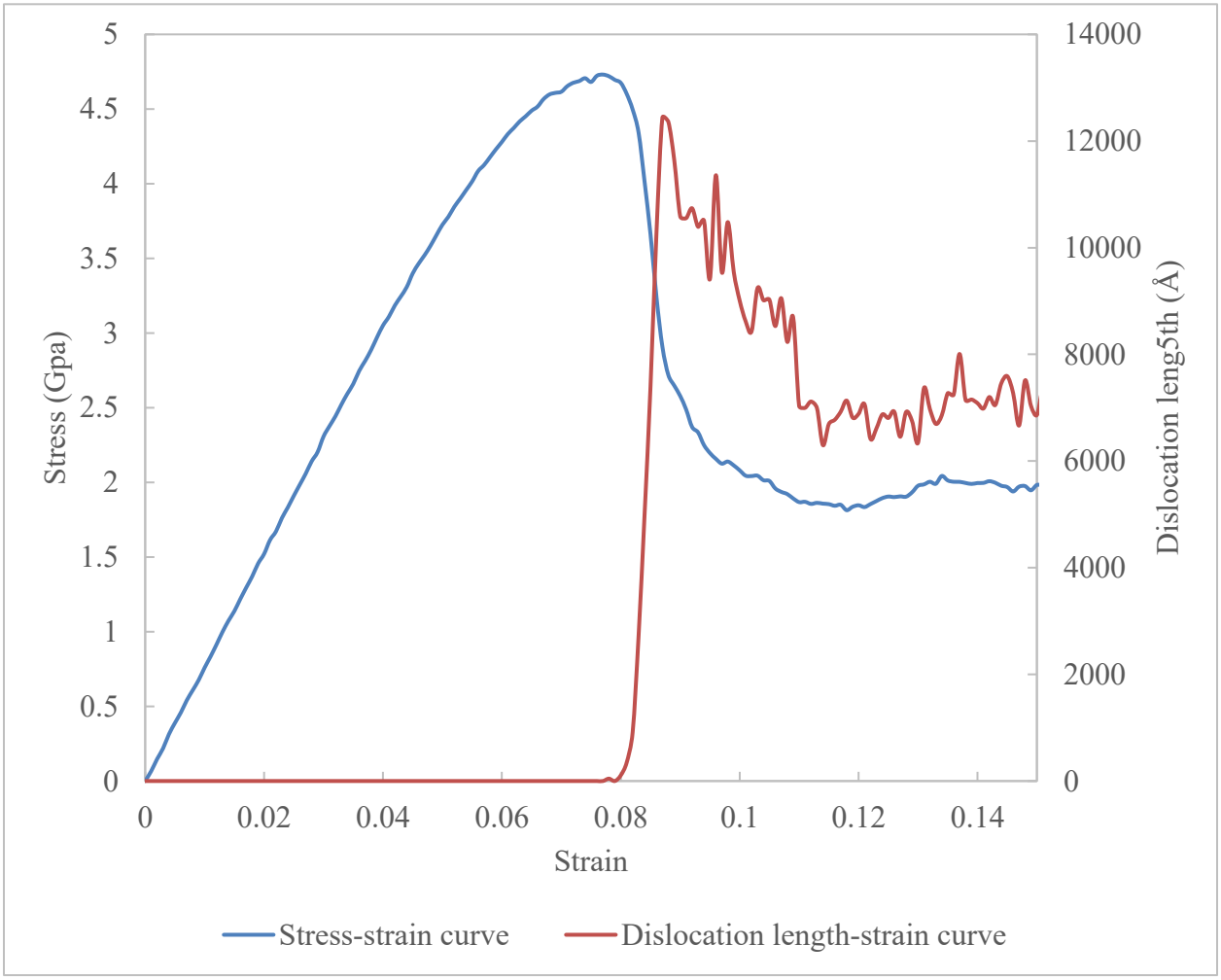

Figure 12 Stress-strain response curve and dislocation-length-strain curve for the sample with no-void; 216 γ' cubes; 300K

proliferating the density of movable dislocations and hence decreasing the rate of dislocation movement. Dislocation nucleates as soon as the yield stress inside the system reaches the threshold of dislocation nucleation, and the sample enters the period of plastic deformation where the stress level starts to come down with the growth of dislocation. Therefore, the corresponding stress becomes instantly lower, following in a yield phenomenon in the stress-strain curve. The segment between the strain of 7.8% and 8.2% on the stress-strain curve in Figure 12 evidently showed that a sudden increase in the dislocation length corresponds to a sudden drop in stress. The stress continues to reduce with increasing dislocation length. At 8.7% strain in the graph, the dislocation density increases to the maximum value and the stress decreases to minimum value; therefore, the total dislocations show a downward trend. After that position, the reduction of mobile dislocation and the increase of unmovable dislocations lead to the dynamic equilibrium of material deformation. In other words, the stress remains stable as the strain increases. Whereas, the generation of different types of partial dislocation is the reason for the increase in the dislocation length and the reduced rate of stress reduction after 8.7% strain. The small peak in the stress at 14% strain value of the stress-strain curve is caused by the emergence of another type of dislocation during the dislocation reaction between the voids [73].

Dislocation dynamics inside the material can be explained in terms of local strain. During the compression test, with continuous pressure, a local strain of atoms develops inside the material. Figure 13 is showing a bar of the range of strain from 0.0033 to 0.25 with a color-coding from black to white. At the very beginning of the test, the system shows only black screen as there is no other local strain accommodates after a successful equilibration. With time applied strain rate force the atoms to move from their original stable position, resulting a local strain inside the atoms of the system. At this moment color bar goes up from black towards the

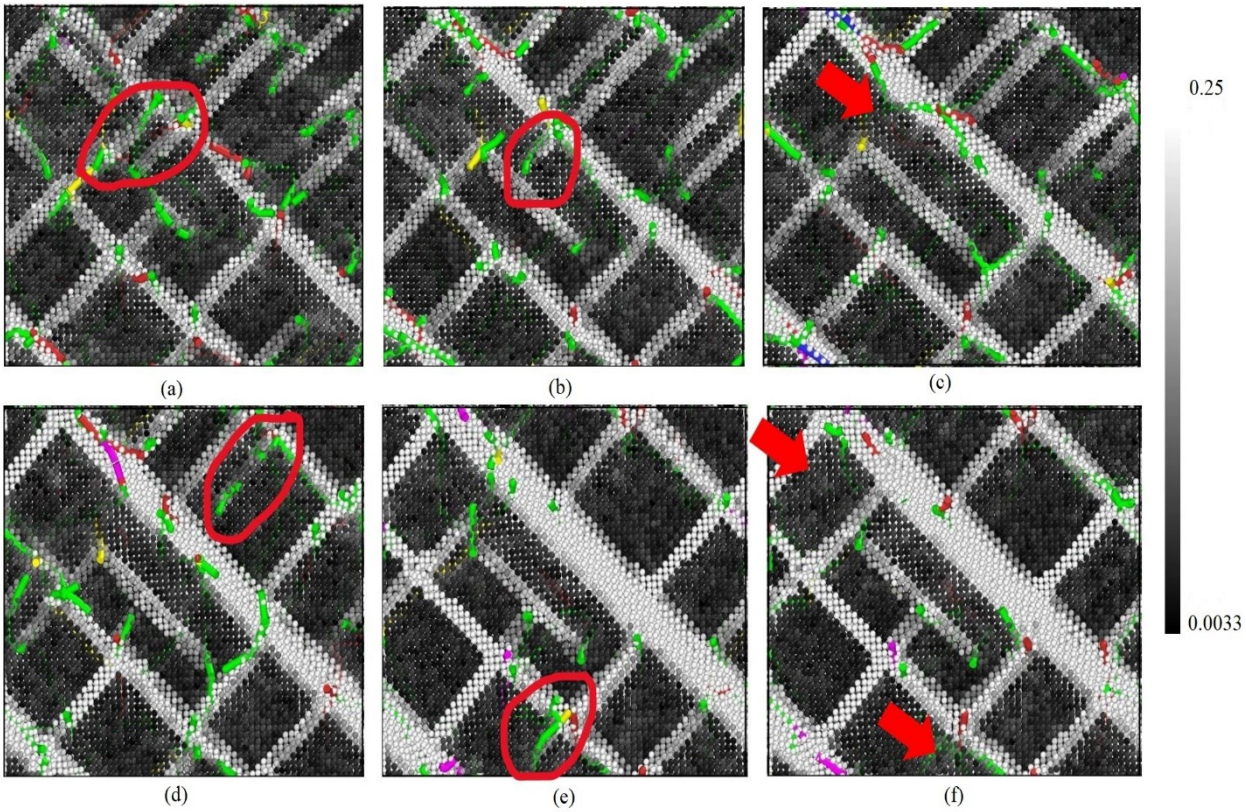

Figure 13 Dislocation dynamics with respect to strain (a) ε= 0.065 (b) ε= 0.07 (c) ε= 0.075 (d) ε= 0.09 (e) ε= 0.095 (f) ε= 0.1

white region, focusing the locally strained region on the {111} plane as this is the slip plane of face-centered cubic structure.

When the stress level inside the system becomes high enough to make the atoms move with high local strain, dislocation (green line) appears into locally high strained zone [Figure 13 (a), Figure 13 (b), Figure 13 (d), Figure 13 (e)]. As soon as the dislocation starts to grow, or in other word, atoms start to move from their original minimum energy position, local strain inside the atoms also start to come down. Therefore, with time atoms move on the {111] slip plane causing the stress level inside the system to have a downward trend; hence, dislocation propagates with time. Consequently, all the locally strained atoms find the next minimum potential energy position and the local strain inside the atoms disappear in this relaxed position,

which is reflected through the color-coding bar as the atoms color change from white to black again that is the minimum strain color of the system. As a result, the dislocation also disappears from that relaxed region confirming that the atoms are their new relaxed position.

Dislocation density. Dislocation densities resulting from the introduction of void(s) into the system as a function of strain are shown in Figure 14. Initially in the elastic region variations in dislocation density will be zero as the stress inside the material is not enough to move the slip plane, hence starting the dislocation. After a certain time when dislocation nucleates, and dislocation starts to propagate due to stacking fault and dislocation density starts to rise with strain. Once the dislocation density reaches in the peak position and then again comes down due to the reduction of mobile dislocation and the increase of the unmovable dislocation. Nevertheless, the generation of different types of partial dislocation during the dislocation reaction between voids is responsible for the fluctuation in the dislocation density after the peak point.

As we have stated in the previous section that dislocation nucleates first at the void surface, hence, dislocation nucleates fast in the sample having 8 voids compared to the samples having single void or no void. Because of having many nucleation sites in the sample with 8 voids should produce many dislocations through the compression test, and sample with no-void should produce the least dislocation as there is no potential nucleation site inside the system. But surprisingly the situation is completely vice-versa here in Figure 14. Dislocation density is way too high in the system with no-void comparing to the dislocation density in the systems with void(s).

While talking about the voids we should consider the dislocation reaction between the two voids that occur in the slip zone. The lower dislocation density in the system with void(s) is

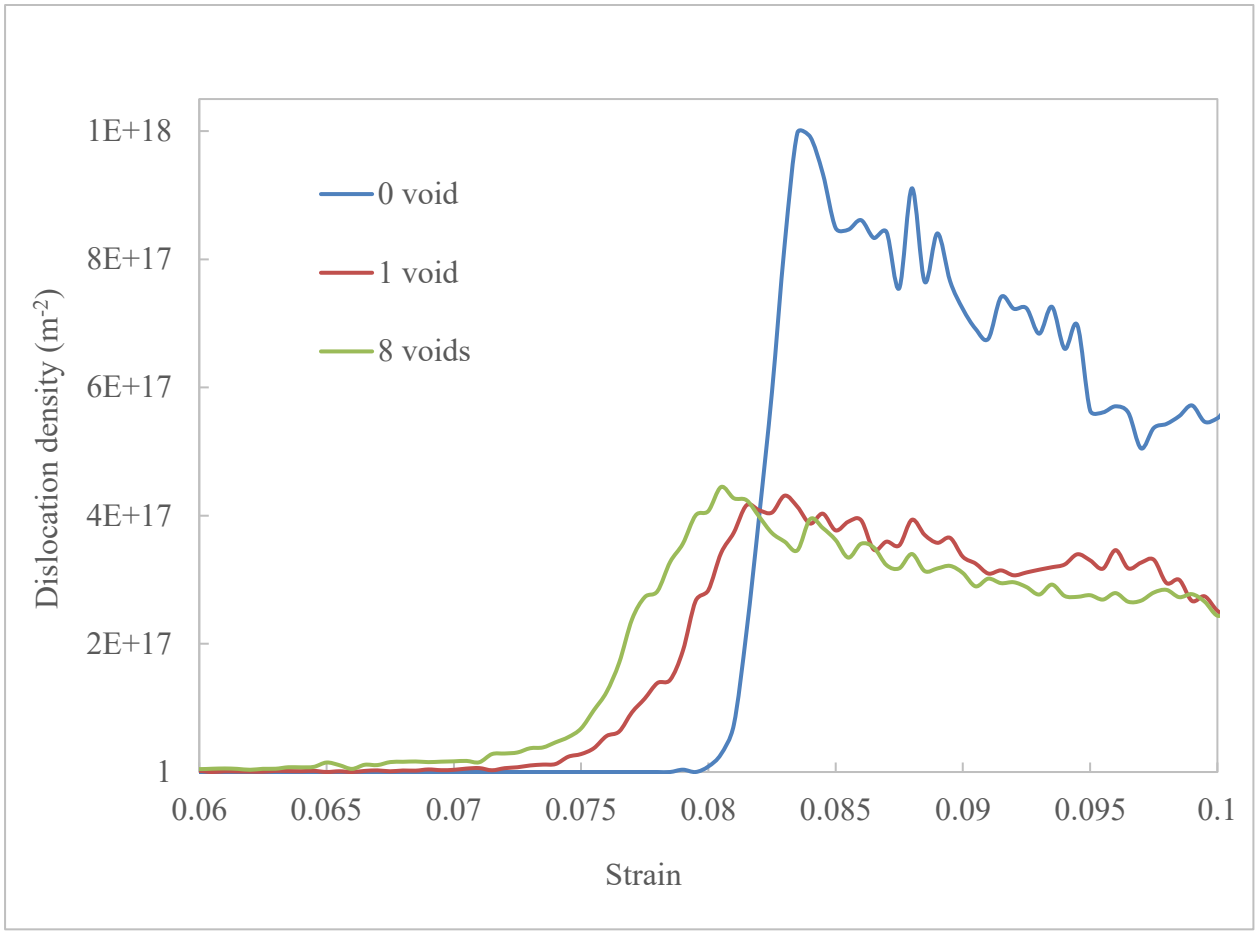

Figure 14 Comparison amongst dislocation density for the systems with no void, 1 void and 8 voids; 216 γ' cubes; 300K

due to the formation of dislocation interaction between two dislocation lines, as shown in Figure 15. Considering the influence of the voids into account, a dislocation joint easily forms between the voids, which obstruct the dislocation movement, causing a decrease of the total dislocation density inside the system. Whereas, for the system with no-void, though dislocation nucleates comparatively later due to the lack of the nucleation sites, but once the dislocation nucleates, it propagates without any obstacles inside the γ phase, resulting high dislocation density with time. In summary, the simulation results of the compression test of the system with void(s) indicate that the interaction between voids is mostly responsible for the lower dislocation density insidethe system. Nevertheless, dislocation nucleation is easy here, but the continuous hindrance

in the way of the dislocation propagation keeps the final dislocation density low into the system [73].

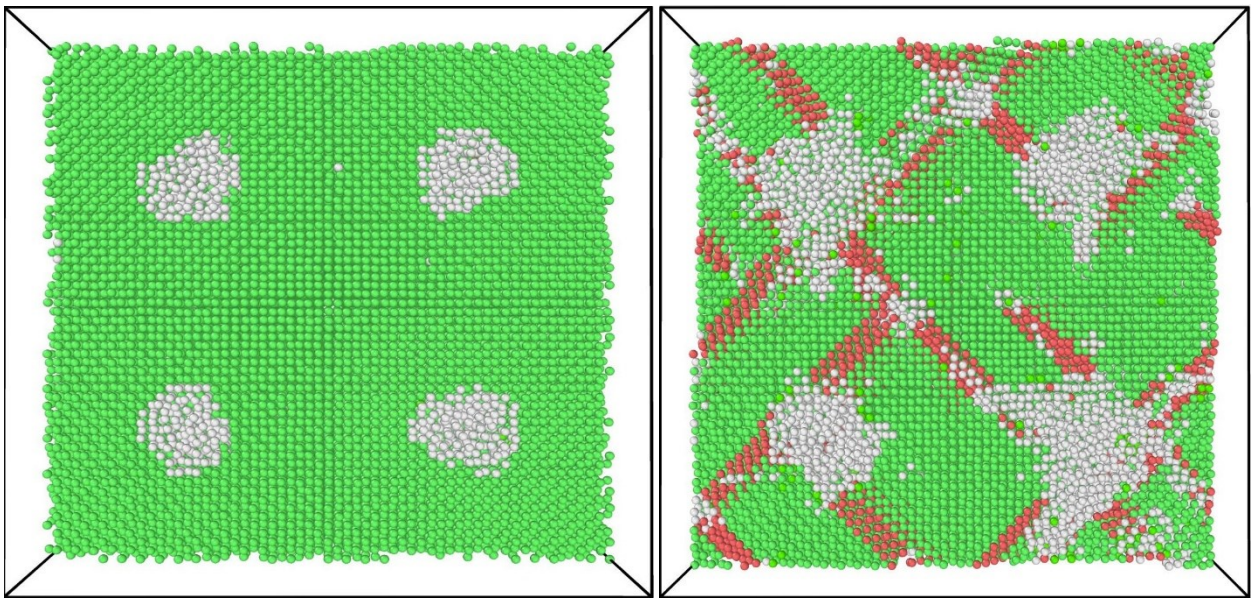

Figure 15 Snapshot of sliced sample with 8 voids at 0ps (left) and at 16ps (right)

Types of dislocation. Shockley partial dislocation and Frank partial dislocation are two important dislocations that occur in face-centered cubic crystals. Increment or decrement of the occurrence of stacking faults depends on the slip of {111} plane, which is the slip plane for face-centered cubic crystals. Comparing the results of Figure 16, Figure 18 and Figure 17, we found that at the initial stage of dislocation, the dislocation grows slowly the majority of the dislocation movement represents Shockley dislocation, which is mainly a/6 <112>. The dislocation growth rate rises suddenly after 8%, 7.5% and 7.1% strain in Figure 16, Figure 18 and Figure 17 respectively, where most of the dislocations are Shockley partial dislocation as well. Other partial dislocations are Hirth, Frank, and Stair-rod partial dislocation.

Nickel-based superalloy is comprised of γ-phase and γ'-phase, both are face-centered cubic structure, therefore, produce mostly Shockley partial dislocation because of having {111}

slip plane. Hence, it is easier to move through the slip plane and create stacking fault. Due to the movement of the slip plane, the stacking sequence of face-centered cubic crystal ABCABC becomes ABAB, which is the stacking sequence of hexagonal cubic crystal. Another partial dislocation type produced in the system is stair-rod, which is edge type dislocation 1/6<110>.

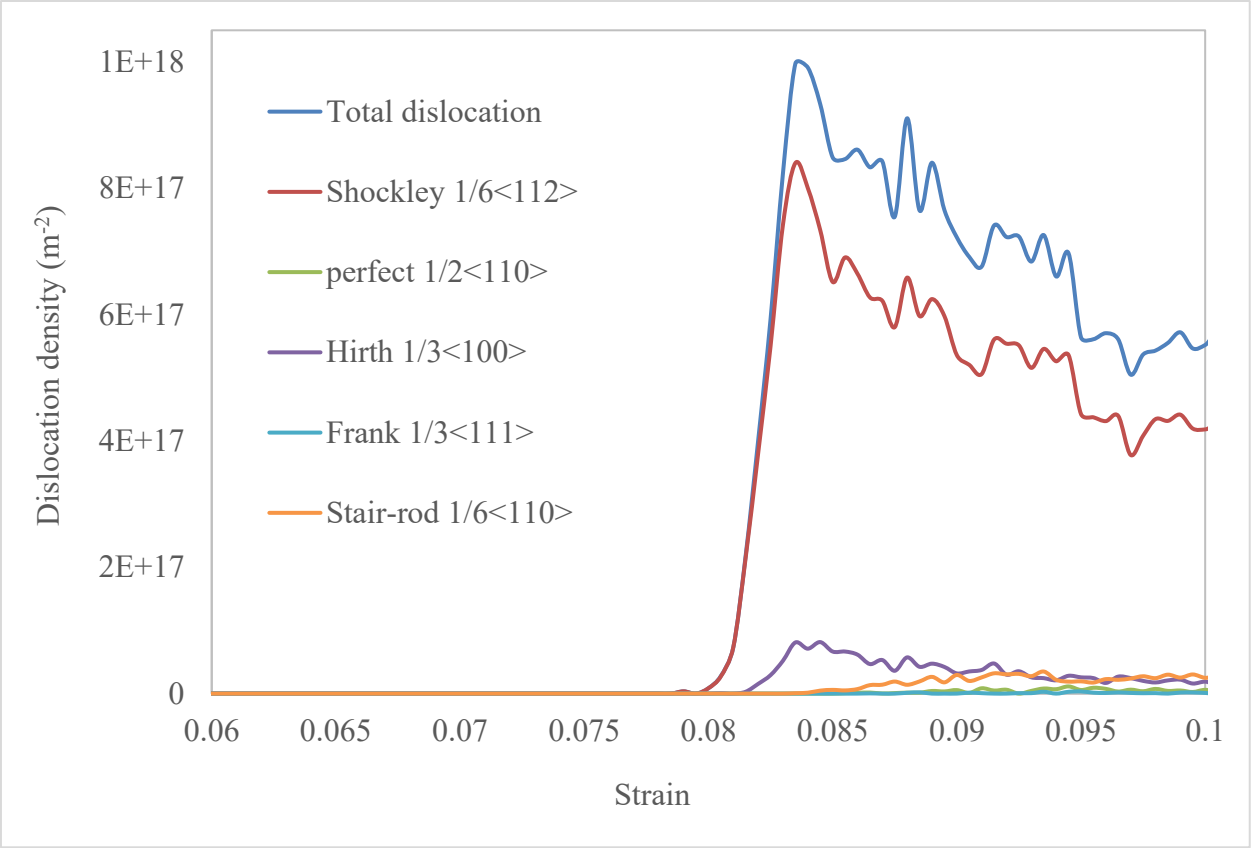

Figure 16 Types of dislocation appears in the system with no-void; 216 γ' cubes; 300K

Burgers vector of this type of partial dislocation is located on {100} plane, which is not a slip plane for face-centered cubic structure, which makes it difficult to slip and can only climb in nickel-based superalloy. Therefore, stair-rod dislocation is a fixed dislocation in our system and is guided by two partial dislocations 1/6<$\bar{2}$11> and 1/6<211>, respectively, and by two parts of misalignment on the (111) and ($\bar{1}$11) planes. This dislocation is consisting of two stacking faults

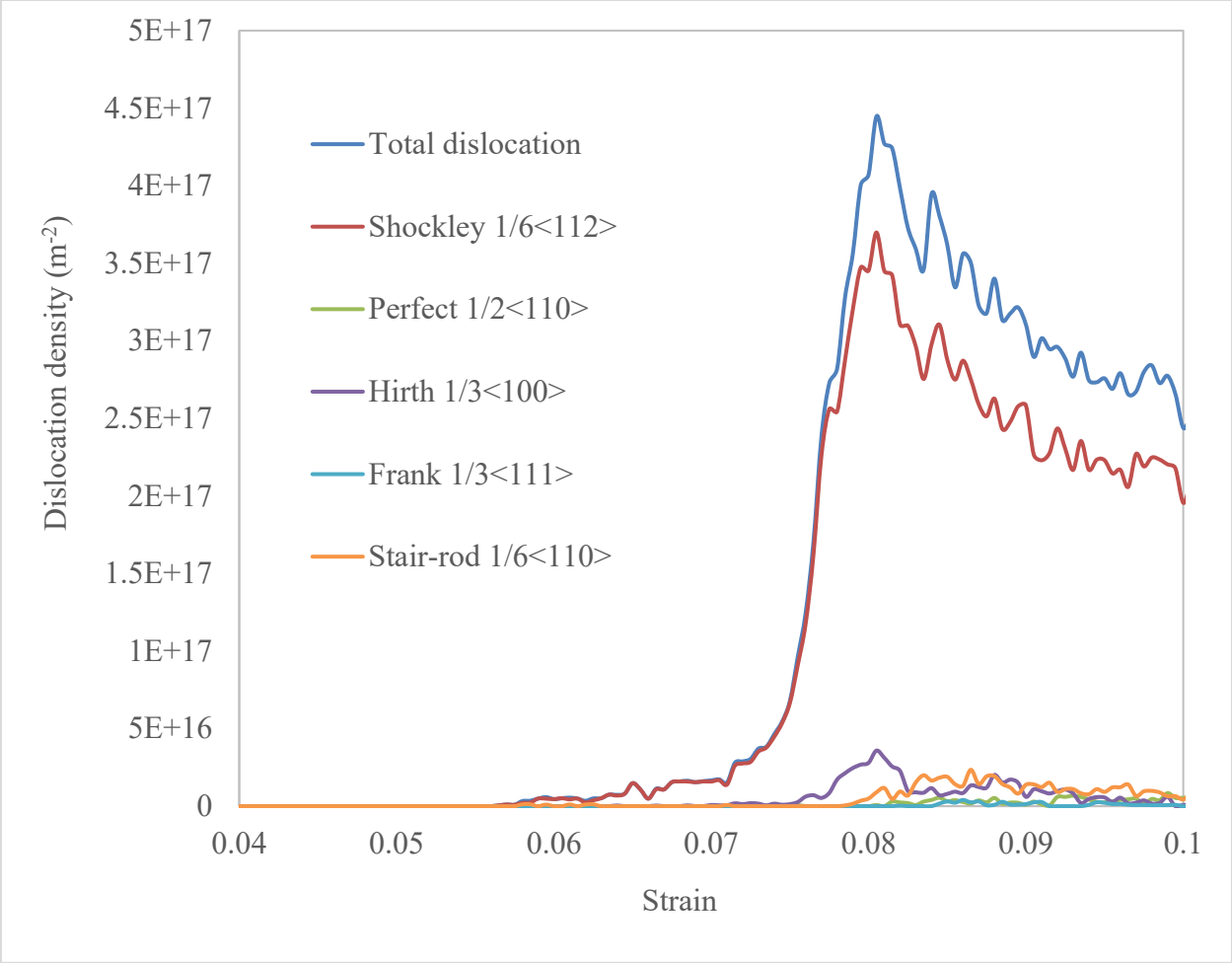

Figure 17 Types of dislocation appears in the system with 8 voids; 216 γ' cubes; 300K

and three partial dislocations is called Lomer-Cottrell dislocation, and the Lomer-Cottrell dislocation lock is:

$$1/6\langle 21\bar{1}\rangle + 1/6\langle \bar{2}11\rangle \rightarrow 1/3\langle 00\bar{1}\rangle$$

$$1/6\langle 0\bar{1}1\rangle + 1/6\langle \bar{2}11\rangle \rightarrow 1/3\langle \bar{1}00\rangle$$

Another common partial dislocation that occurs in face-centered cubic crystal is Frank dislocation, which is a pure edge dislocation, hence it can climb along the wrong surface through the point defects, but it cannot slip and expand on the slip plane. Frank dislocations are also immobile dislocations or fixed dislocations, whereas Shockley dislocations are referred to as

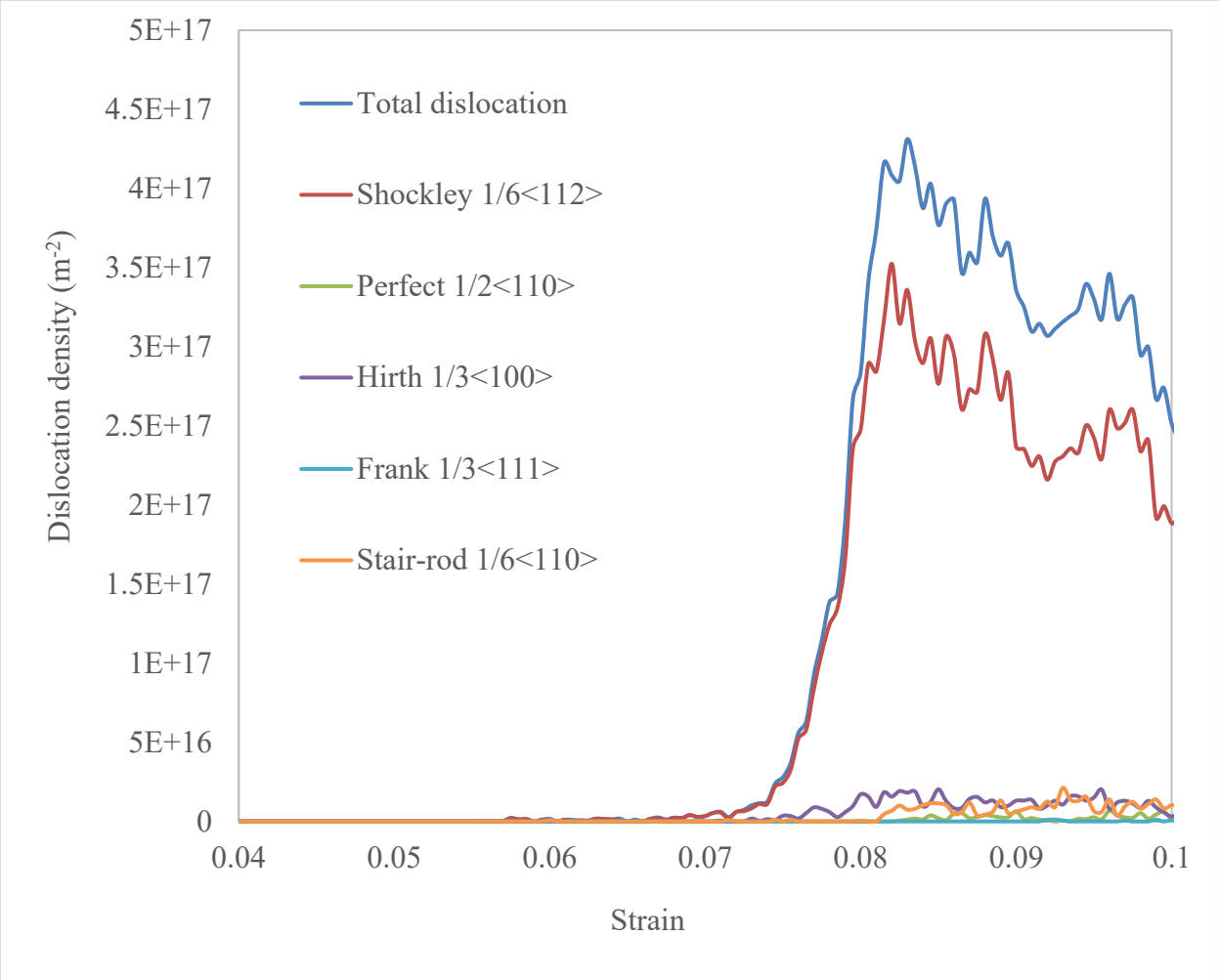

Figure 18 Types of dislocation appears in the system with 1 void; 216 γ' cubes; 300K

mobile dislocations. Another difference between Shockley partial dislocation and Frank partial dislocation is that the Burgers vector of Frank partial dislocation is perpendicular to the stacking faults layer, whereas the Burgers vector of Shockley partial dislocation lies parallel to the stacking faults layer [73].

The motion of two partial dislocations fulfills the movement of a perfect dislocation. The stacking fault nucleates on the (111) slip plane separates into two Shockley partial dislocations. The possible reaction is:

$$1/2\langle 1\bar{1}0\rangle \rightarrow 1/6\langle 1\bar{2}1\rangle + 1/6\langle 2\bar{1}\bar{1}\rangle$$

This reaction can be expressed from the Thompson triangle of face-centered cubic metal shown in Figure 19 [73]. From the triangle we can express the perfect dislocation as

$$\overrightarrow{BC} \rightarrow \overrightarrow{B\alpha} + \overrightarrow{\alpha C}$$

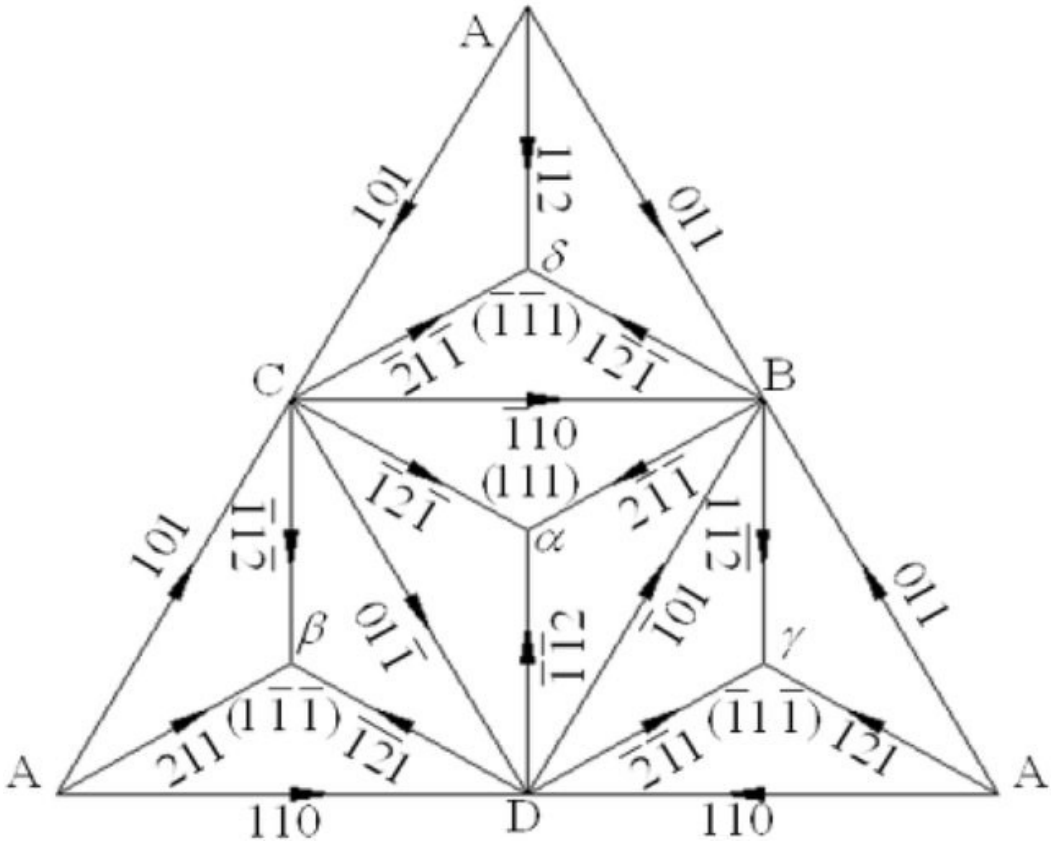

Figure 19 Thompson triangle of face-centered cubic metal

Effect of void radius. The radius of the void also has an influence on void growth and coalescence. The stress-strain curve for three different systems having different radius of the void were analyzed. The simulation results given in Figure 20 indicates that the critical yield stress and strain values σ_c and ε_c decrease with increasing void radius, and the initial nucleation of the dislocation occurs faster at the free surface of the larger void. An observable stress concentration occurs on the surface of the void with a larger radius while increasing the void radius, resulting in a critical shear stress of dislocation movement. Additionally, with increasing

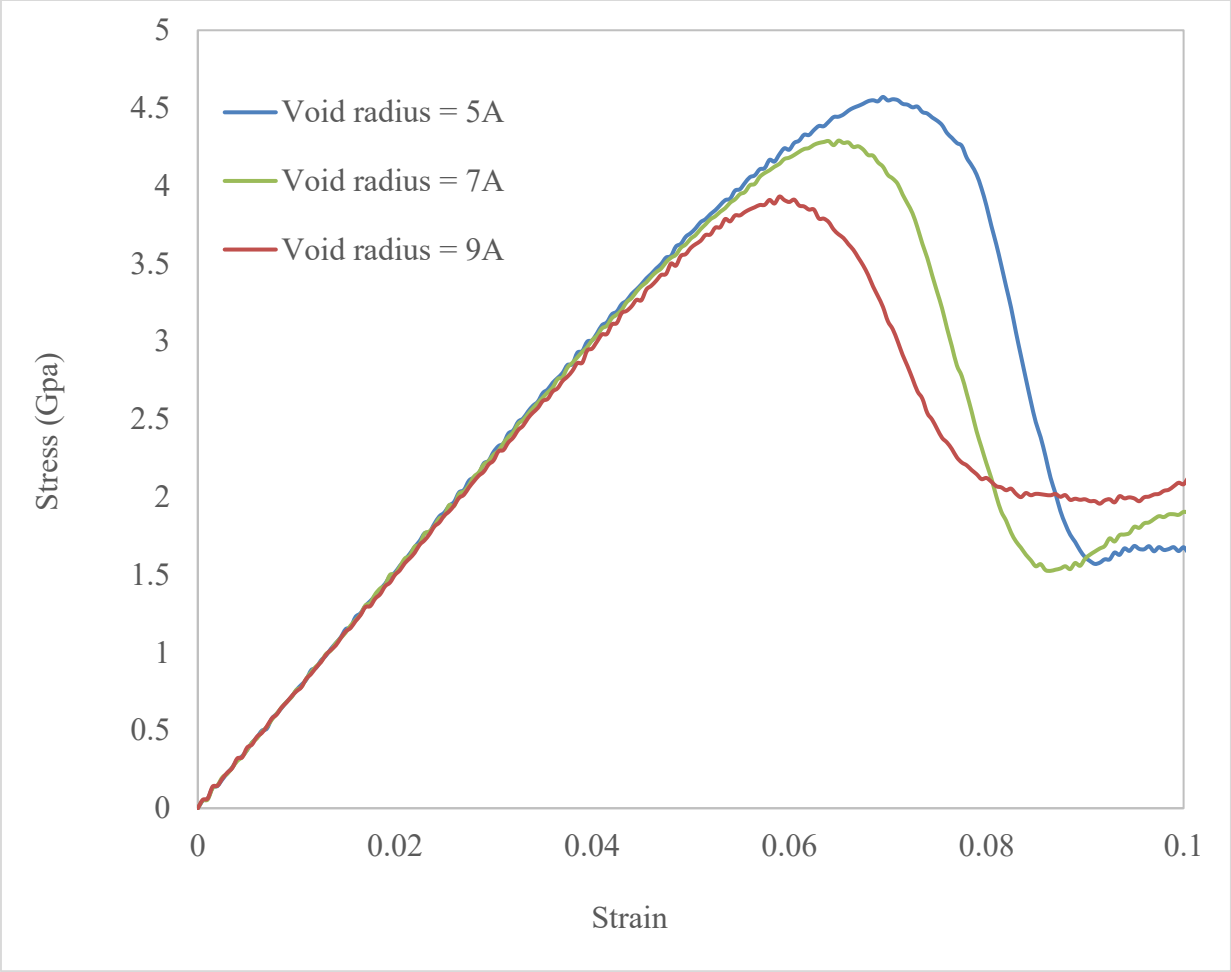

Figure 20 Stress-strain curve for nickel-based single crystal superalloy with 216 γ' nanophases for different void radius at 300 K

void radius the internal defects of the material also increase. This phenomenon justifies that the initial defect apparently affects the mechanical properties of materials. However, the deformation and creep resistance of the materials increases with the decreasing size of void defects. Thus, the void size inside the system significantly influence the dislocation evolution. Higher amount of free surface gives rise to higher stress concentration, hence makes the dislocation to initially nucleate and propagate on the free surface of the void with the larger radius [73].

Figure 21 is showing the dislocation evolution from the void surface of three different samples having void radius 3Å, 5Å and 7Å respectively. At $\varepsilon = 0.045$, dislocation has just started

to show up in the sample with the smallest void radius, whereas the sample with highest void radius already has multiples dislocations in the void surface and evaluating in a semi- circular

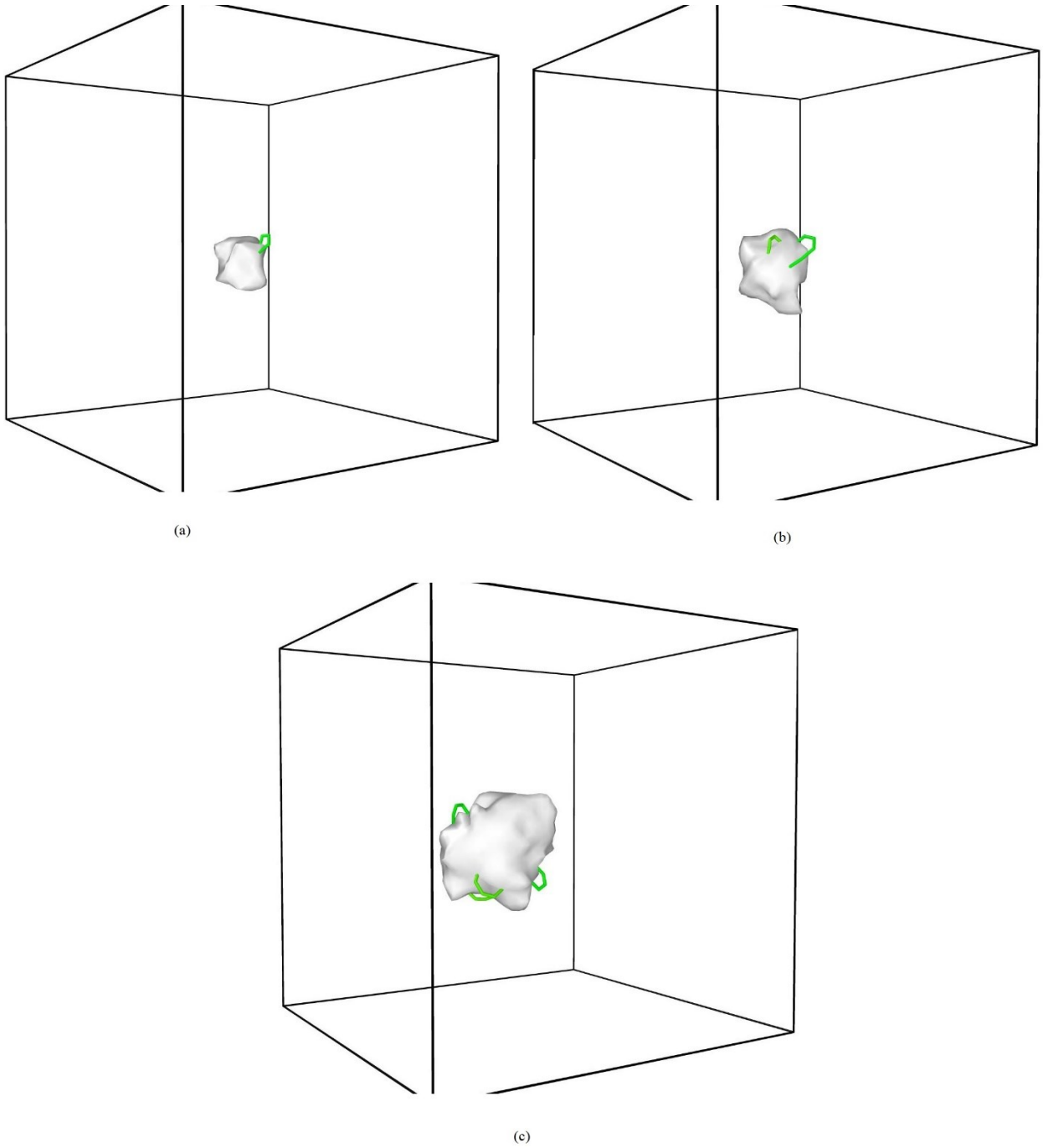

Figure 21 Illustration of dislocation evolution at ε = 0.045 from the void surface with different radius (a) $3A^0$ (b) $5A^0$ (c) $7A^0$

loop around the void. These illustrations are establishing our previous argument about the dislocation evolution being faster in the larger void surface.

Effect of Gamma-Prime Nanophase Size and Distribution

The anticipated creep performance is extremely sensitive to the distribution of the reinforcing phase, with a larger increasing the strength considerably. The predicted creep performance is very responsive to the number and distribution of the reinforcing phase. These observations are in qualitative agreement with the data reported in Murakumo's work [1]. In Figure 22 the number of γ' nanophases vary from 1 block to 216 blocks with constant Ni:Al ratio. As expected, the variation in reinforcing phase size and distribution improves the creep rupture life noticeably. One can understand from Figure 22 that reinforcing phases distribution effect is quite prominent. The system with only 1 block of γ' nanophase starts to yield at 4% strain, whereas the system with 216 blocks of γ' nanophases yield at 8% strain, which is double than previous. Presumably, with only 1 block there is enough space for the dislocation to move into the comparatively wider γ phase channel width before it faces any obstacle, which presents the system as a soft one. On the contrary, dislocation in the system with 216 γ' nanophases are being seized before it can move into the less spacious γ phase channel, therefore increase the strength of the system, which is reflected in the graph below.

This can be explained on the basis that a higher number of γ' phases mean finer γ' particle sizes with smaller γ matrix channel widths which gives less space for the dislocation to move & more reinforcing phases to hinder the path of dislocation movement [54]. All the γ' nanophases act like precipitation hardening and cause pinning effect so the dislocation can't move further, and their movement is seized by any reinforcing phase cube. Therefore, more is

the number of γ’ nanophase, more is the pinning effect and the sample shows higher yield strength as well.

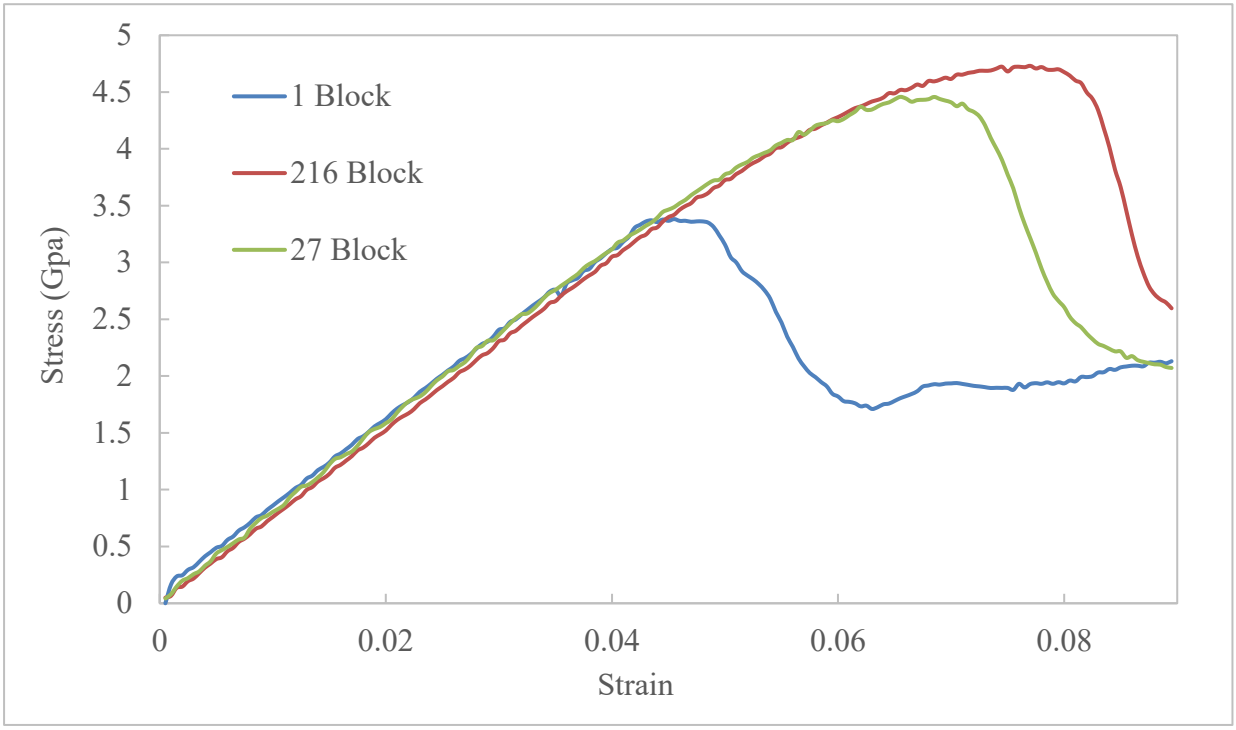

Figure 22 Stress-strain curve for nickel-based single crystal superalloy with different number of γ’ nanophases at 300K

Dislocation evolution of nickel-based single crystal superalloy with 1(one) γ’ nanophase inside. Superalloys failure is a process of a long time, the dislocation network is not suddenly and completely destroyed, but a local damage firstly occurs near the interface because of the high-stress concentration due to lattice mismatch that exists between the γ phase and γ’ phase. In the early stage of compression loading, no dislocation appears in the γ-phase and γ’-phase. Dislocations emanate first in the γ matrix phase as the loading continues [Figure 23(a)]. The figure reveals that the dislocation starts to get compressed into the neighboring γ channels when it approaches the γ’ nanophase. At the same time, the segments that are obstructed in their motion by the γ’ blocks, start to move along the γ/γ’ interface. With the continuation of loading

lots of dislocations in the γ phase move to the γ/γ' interface as the creep time increased to 8 ps, eventually, accumulate at the γ/γ' interface, conducts stress concentration. This phenomenon plays an important role in absorbing dislocations and obstructing sliding dislocations cut into the γ' nanophases. At ε = 4.2%, the γ matrix keeps filling with dislocations, and the deformation continues to be conducted by recurving the dislocations on {111} planes. Additionally, with an increase in the number of dislocations in the γ/γ' interface, the resistance of deformation of the accumulating the two dislocations of opposite sign along the two γ/γ' interfaces. Nevertheless, it seems that, with more compression loading, the released segments cannot get into the next γ phase channel through the periodic boundary condition. As soon as the stress concentration exceeds γ' strength, dislocations in the γ matrix then cut into the γ' precipitates from the γ phase. From the bottom-right corner of the γ' cube, the dislocation is then entered, interfaces where dislocation network is damaged and the deformed dislocations in the γ matrix channel shear, as shown in Figure 23(b).

One can notice that the dislocations on the edges and corners of the γ' cube in Figure 23(b) form the nano-sized dislocation loops. Due to the insufficient stress at the early stage of deformation, the dislocations do not enter the γ channels when their line direction meets the γ' cube. Therefore, some long-bent dislocations are formed in the creep process along the edges and faces of the γ' cube. This type of reaction mainly occurs in the area near the corners of the interface of γ/γ' cube. However, the formation of different types of junctions occurs due to the dislocation's reaction with each other, which can be terminated later by recombination with other incoming dislocations.

The dislocation network appears to be damaged successively with the continuous loading, resulting in the loss of the capability to absorb dislocations in the γ matrix. As plenty of

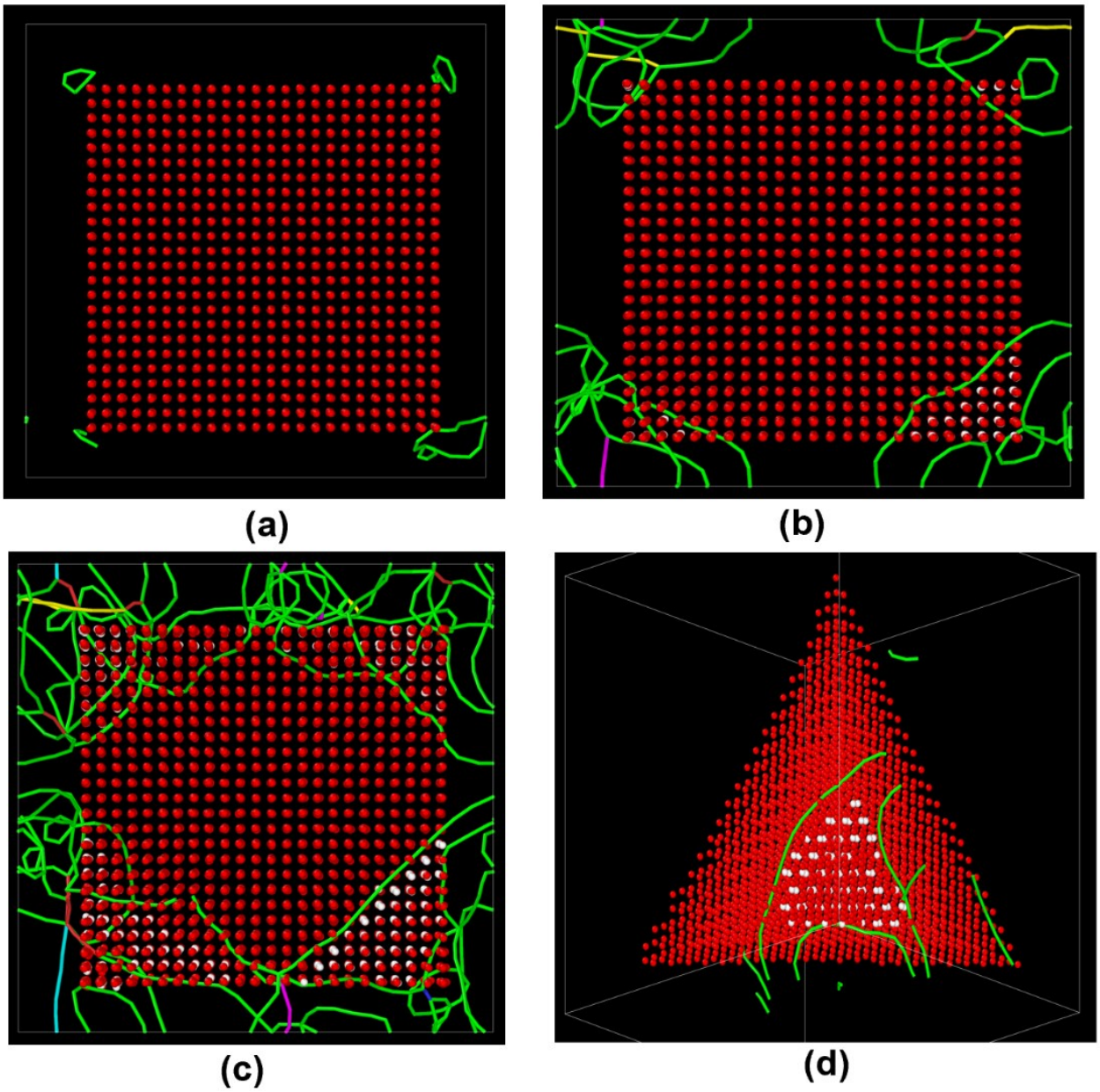

Figure 23 Dislocation evolution of nickel-based single crystal superalloy with 1(one) γ' nanophase inside (a) at 4.8 ps (b) at 8 ps (c) at 24 ps (d) dislocation cutting on the (111) plane

dislocations within the γ phase moved to the γ/γ' interface, high dislocation density generates stress concentration in the γ/γ' interface. As a result, the slip dislocations in the γ matrix will successfully cut into the γ' precipitates from the γ/γ' interface close to the highest dislocation concentration area, as shown in Figure 23(c), due to the local damage of the dislocation network

[74]. The resistance of deformation of the γ’ phase lowered with a rise in the number of dislocations in the γ’ phase. One can see that the dislocation is cutting through the γ’ phase in (111) plane, which is the most densely-packed plane for face-centered cubic structure Figure 23(d) [75].

Dislocation density. The mechanical properties of nickel-based single crystal superalloys highly depend on the formation and evolution of the interfacial dislocation network. The ability of the formed dislocation network to reduce the mismatch stress successfully prevents the dislocation from cutting into the γ’ phase, thus complement the creep resistance of superalloys. In this work, we tried to find out the interfacial dislocation network evolution process and then present them in detail to understand the creep behavior of nickel-based single crystal superalloy with different number of γ’ nanophases. Doing the simulation for a system with 216 γ’ particles guides to a different dislocation configuration by averaging and making the various microstructure mechanisms ease around each particle. Again, simulation of a sample containing only one γ’ particle confine the dislocation self-interaction consequence to an area next to the simulation cell boundaries. Additionally, different dislocation self-interaction consequences can take place with the use of periodic boundary conditions comparing to the system where a non-periodic boundary condition is used, resulting in a larger variation in the plastic strain and dislocations density compared with the multiple simulation box.

Dislocation densities resulting from the different number of γ’ nanophase and distribution as a function of strain are shown in Figure 24. When the system is in the elastic region, dislocation density will be zero as the stress inside the material is not enough to move the slip plane, so no dislocation is appearing at this moment. As soon as the dislocation starts to nucleate around the corner of the γ’ cubes, dislocation density starts to rise with strain. With time, the

dislocation density reaches in the peak position and then again comes down due to the reduction of mobile dislocation and the increase of the unmovable dislocation. However, the fluctuation in the dislocation density after the peak point takes place because of the generation of different types of partial dislocation.

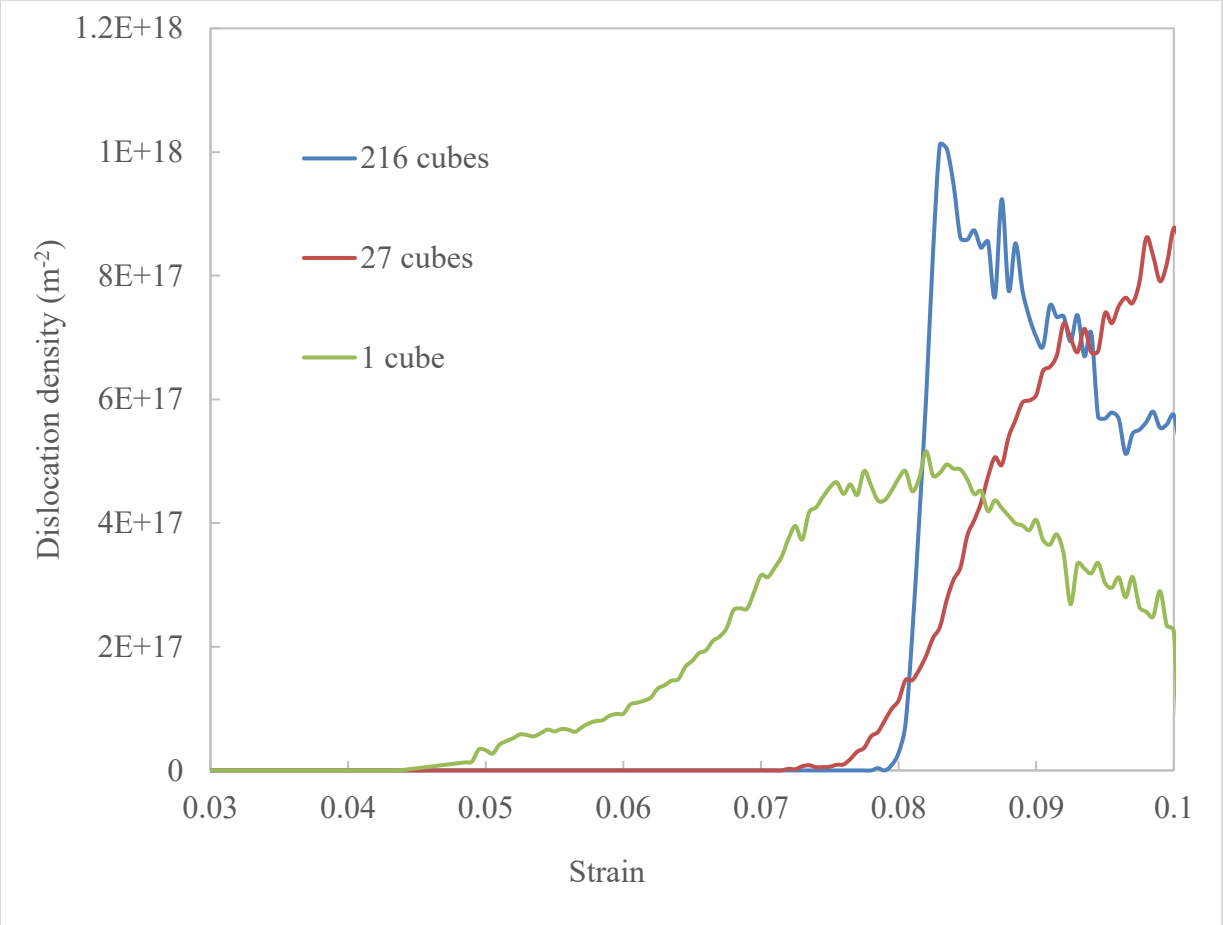

Figure 24 Comparison of dislocation density for the systems with different γ' cubes at 300K

As we know from the previous section that the system has only 1 γ' nanophase shows lowest yield strength amongst three of the systems, dislocation density also starts to grow very early for 1(one) γ' cube system. With the continuation of loading lots of dislocations in the γ phase move to the γ/γ', eventually, accumulate at the γ/γ' interface, increases the dislocation density. Eventually, the γ matrix keeps filling with dislocations, and the deformation continues

to be conducted by recurving the dislocations on {111} planes. Because of the sample structure, having a big γ' phase, hinders the movement of dislocation and dislocation get deformed at the γ/γ' interface. Having said that, we observed the highest dislocation density for the sample with 216 γ' nanophases.

Dislocation type. Similar to our discussion in previous section about the dislocation type production in the system with the presence of voids, types of dislocation that produces in the samples having different types of γ' phases are mainly Shockley partial dislocation and Frank partial dislocation, as our sample is face-centered cubic structure. Comparing to Figure 25 and Figure 26, it is evident that partial dislocation type depends on the sample structure only. At the

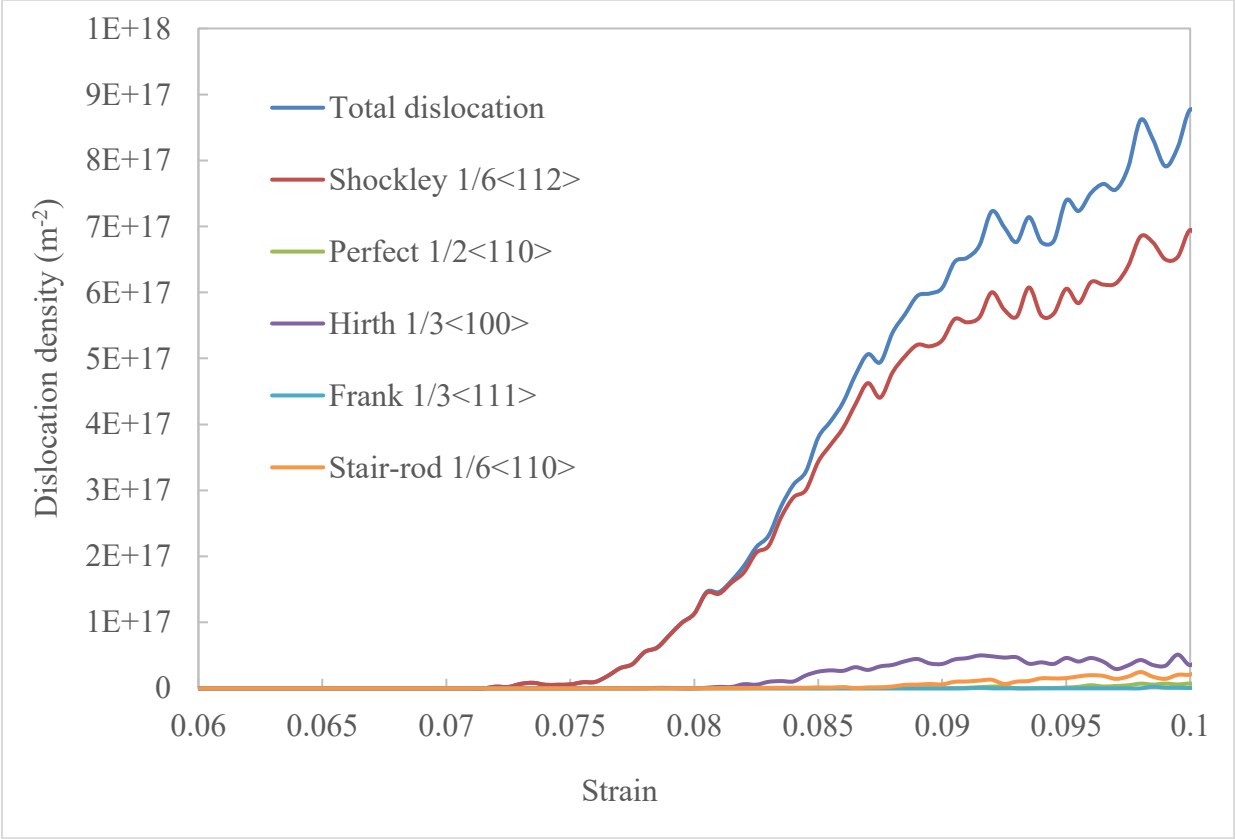

Figure 25 Types of dislocation produced in the sample with 27 γ' nanophases at 300K

beginning of the loading, Shockley partial dislocation is the only type that appears after 7% strain. This partial dislocation type dominates till 8.2% of strain, after that Hirth partial dislocation appears and contribute to the total dislocation density. At the initial stage of dislocation, the dislocation grows slowly and most of the dislocation movement represents Shockley dislocation. For both cases, Hirth partial dislocation is the 2nd dominating type and appears after 8.2% strain, when the stress is enough to make a dislocation climb. It seems that for the system with 216 γ' nanophases, density of Hirth partial dislocation is little higher than the system with 27 γ' nanophases. This amount of difference in the density is understandable considering the fact, that total dislocation density for higher distributed reinforcing phases is also higher than the lower distributed reinforcing phases. Other partial dislocation types are Frank

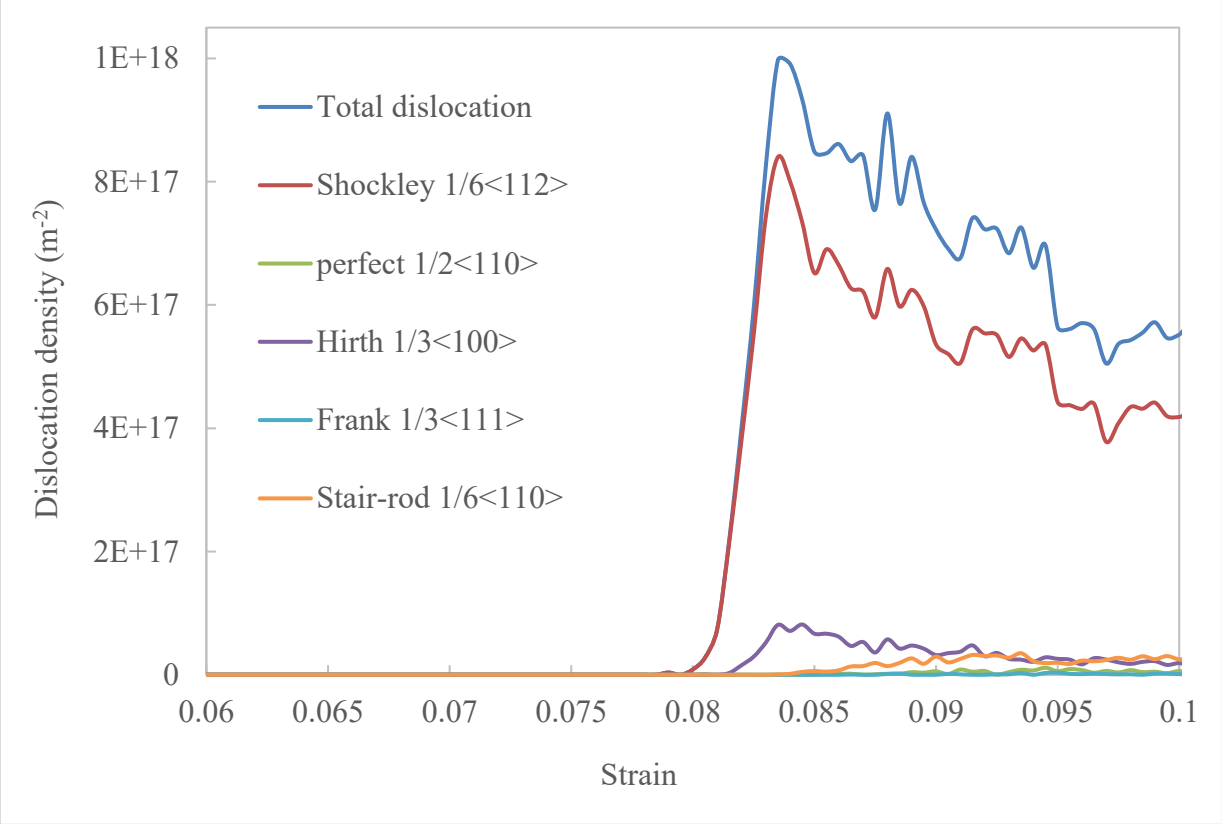

Figure 26 Types of dislocation produced in the sample with 216 γ' nanophases at 300K

partial dislocation and Stair-rod partial dislocation, contributing in a less amount to the total dislocation density.

Creep Deformation in Nickel-Based Polycrystal Superalloy

To identify the atomic behavior and governing creep mechanism of nickel-based polycrystal superalloy some attempts have been found to study the mechanical properties of polycrystalline metals using MD simulation as a tool [4]. These studies reveal that grain size, temperature, and applied stress accompanying the creep deformation in polycrystalline materials. Bird-Dorn-Mukherjee equation exhibits the relation of these three parameters with the steady-state creep rate [76]:

$$\dot{\varepsilon} = \frac{AD_oGb}{k_BT}\left(\frac{b}{d}\right)^p\left(\frac{\sigma}{G}\right)^n \exp\left(-\frac{\triangle Q}{k_BT}\right)$$

Where $\dot{\varepsilon}$ is the steady-state creep rate, A is a dimensionless constant, D_0 is the diffusion coefficient, b is the Burgers vector, G is the shear modulus, k_B is the Boltzmann's constant, T is the absolute temperature, d is the grain size, σ is the applied stress, ΔQ is the activation energy for thermal-activated process, p and n are the grain size and stress components, respectively. According to the equation, grain size decrement tends to increase the tendency of ultra-fine-grained polycrystal to suffer creep deformation. We can predict an idea about the underlying creep process from the grain size exponents. For instance, if $p = 2$, the governing creep mechanism will follow Nabarro Herring creep or lattice diffusion creep, while $p = 3$ follow grain boundary diffusion creep. Therefore, the value between $2 < p < 3$ suggests an addition of lattice diffusion, grain boundary diffusion, and grain boundary sliding creep [77]. Figure 27 is showing the confirmation of interaction. Presence of the high volume of grain boundary in the nanocrystalline sample is the main reason for this type of creep mechanism. Grain size

dependence of power-law creep is not observed in bulk materials due to the little interaction of dislocation activities with grain boundaries and their restriction inside the grain. On the contrary, this situation is complete vice-versa in fine-grained nanocrystalline material. Because of the very

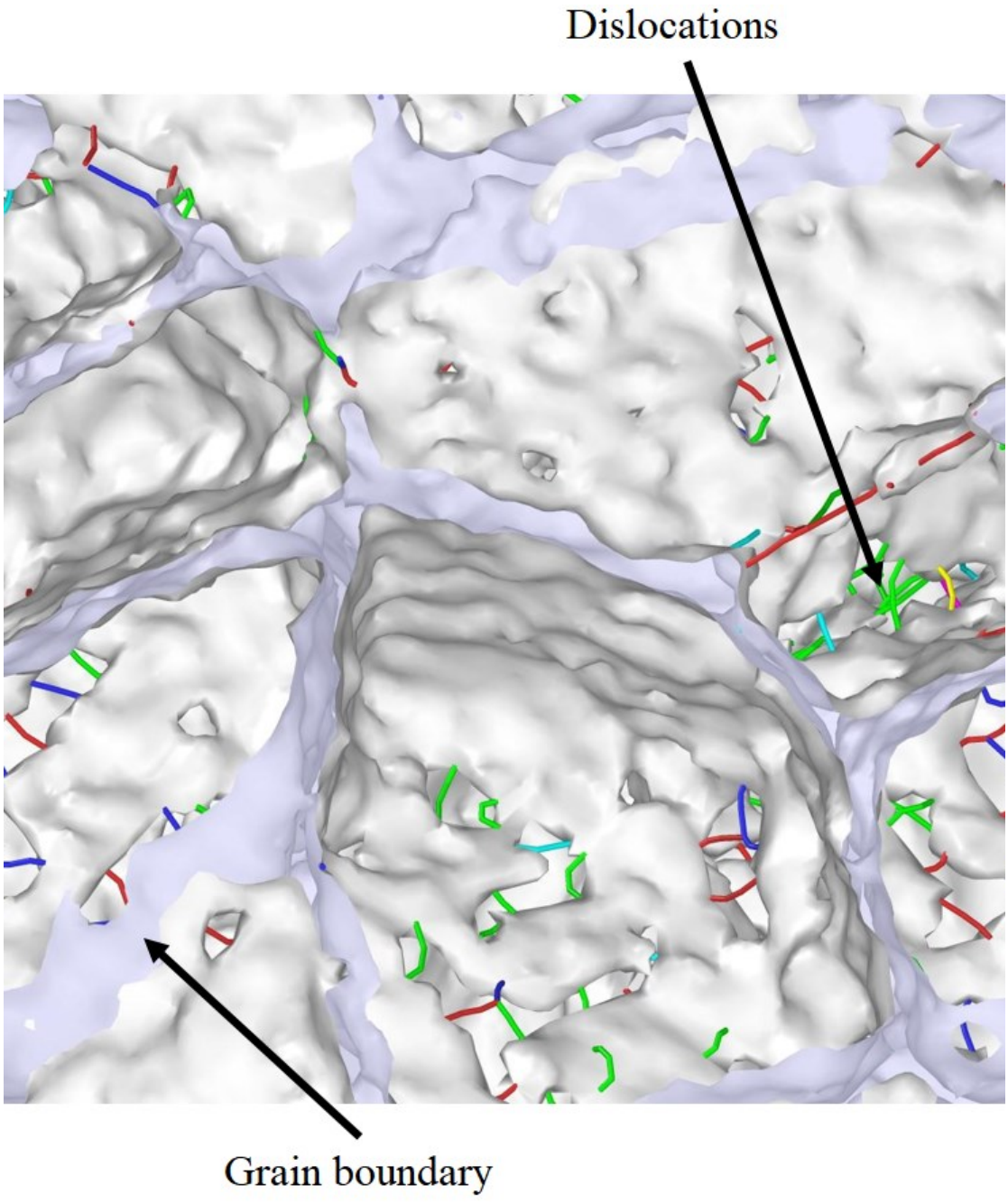

Figure 27 Dislocation and grain boundary interaction inside a polycrystalline sample

small grain size, dislocation and grain boundary interaction takes place all the time. Here, the compression on an ultra-fine-grained polycrystalline sample of 9.54 nm is considered at 300 K temperature. From almost every side of the grain boundaries dislocations emerging, hence, interacting with the grain boundaries. This phenomenon is very uncommon for larger grain sized polycrystalline structure as there is adequate space for the dislocations to move within the grain. Thus the grain size highly controls the creep phenomenon [78].

For polycrystalline materials, when they are under loading dislocations emanate from the grain boundary and all the mobile dislocations inside the grains tend to pile-up at grain boundaries. This act demands higher stresses to make the dislocations move further, thus the materials plastically deform. However, according to the Hall-Petch relationship [79], [80], materials lose strength at smaller grain sizes in ultra-fine-grained nanocrystalline metals, which is referred to as inverse Hall–Petch relationship [81], [82]. Figure 28 (illustration Ref. [83]) is showing the schematic view of this transition in strengthening with grain-size-depending. Strength is inversely proportional to grain size for large grain sized polycrystal, which is labeled as ‘‘Hall– Petch’’ region on the plot. The scenario is completely opposite when the grain sizes are 20 nm and below, i.e. the strength of nanocrystalline metals increases with grain size, which region is labeled as ‘‘inverse Hall–Petch’’ on the plot. The center/middle region is for metals with approximate grain sizes between 20 nm and 30 nm, where strength is maximum [84]. There are some arguments on the specific deformation mechanism behind this inverse Hall-Petch relationship phenomenon. Some proposed mechanisms are partial dislocation emission and absorption at grain boundaries [85], [86], grain boundary sliding [87], [88], grain rotation [89]–[91], and grain boundary migration followed by grain growth.

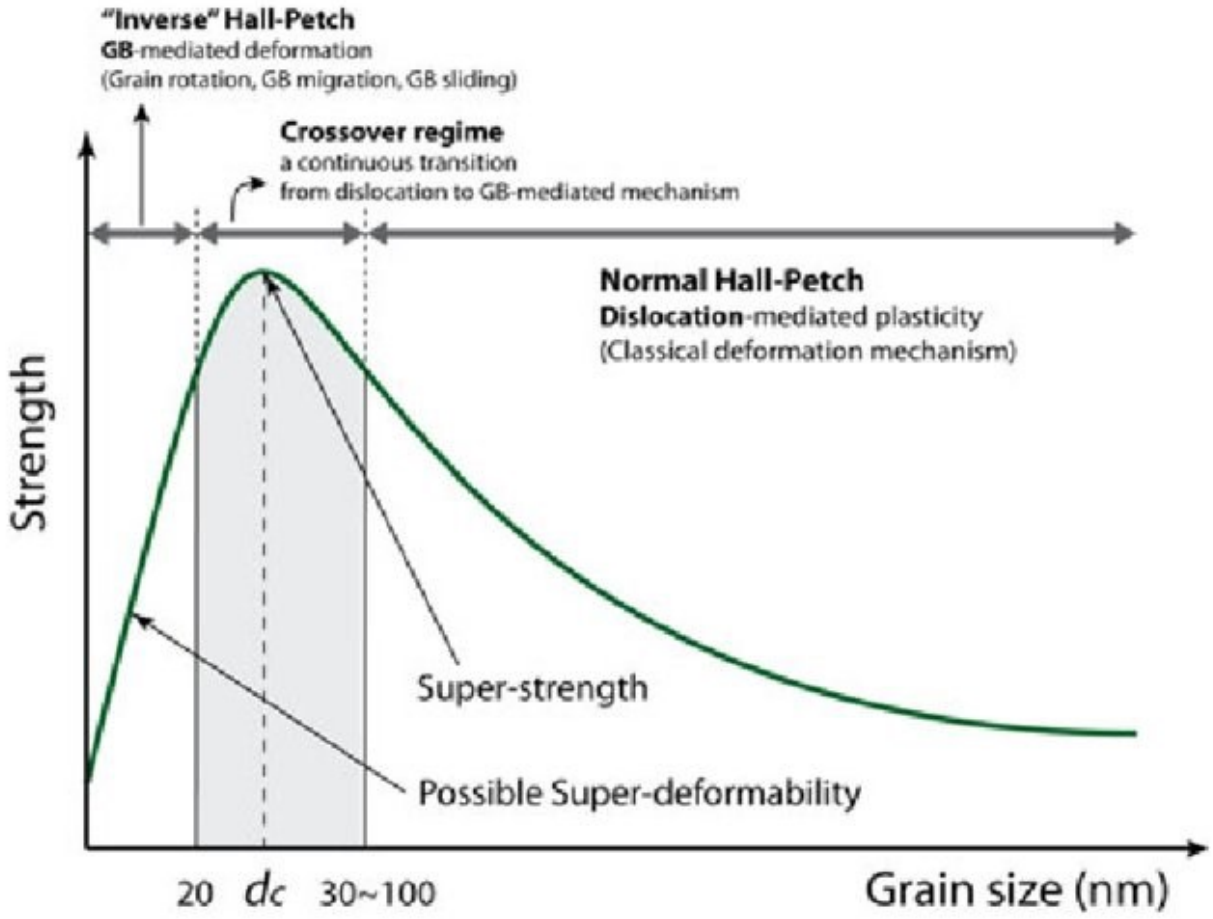

Figure 28 Inverse Hall-Petch relationship showing the dependency of the strength of polycrystalline metals on grain

Effect of Grain Size in Compression

Grain size has a notable effect on the mechanical behavior of a polycrystalline material, especially its yield stress. In this work, nickel-based polycrystalline superalloy with grain size 16 nm, 9.54 nm, 7.5 nm, and 5 nm have been used to observe the change in their dislocation dynamics, hence the creep behavior. Figure 29 is representing the stress-strain curve of nanocrystalline nickel-based superalloy with varying grain size.

For ultra-fine-grained polycrystalline materials, dislocations are not the main mechanism in plastic deformation. In this case, the mechanism of creep deformation is highly driven by the mobile dislocation density saturation and the dislocation density interactions within the grains and the grain boundaries [92]. These grain boundaries are mostly responsible for the ultra-fine-grained polycrystalline structures to lose their yield strength under compression. These grain boundaries can be the fragile part for materials to fracture within the material, also source of dislocations as well. A comparison of MD simulations varying the grain size can allow a better understanding of the effect of grain boundaries on the strength of ultra-fine-grained polycrystalline materials, refers to Figure 29. At the beginning of the compressive loading, the nanostructure behaves elastically, but this elastic period shortens with decreasing grain size.

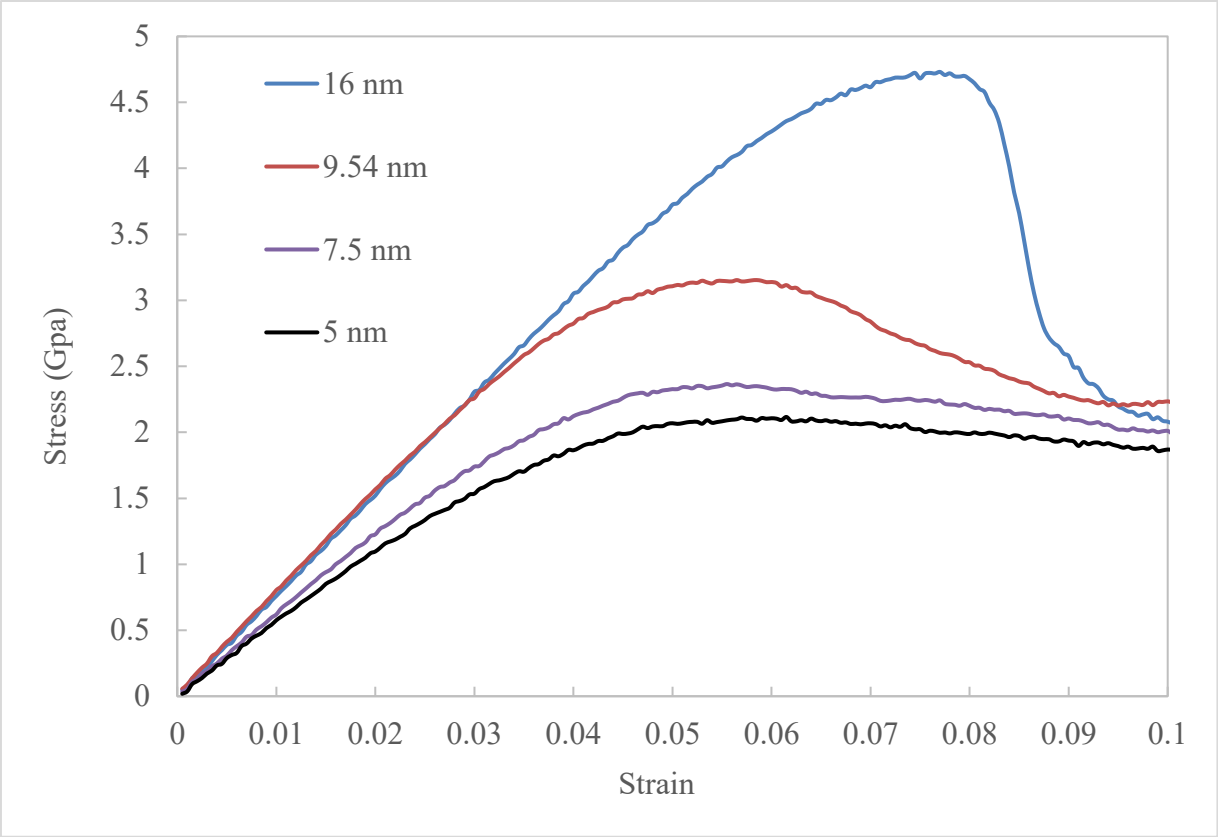

Figure 29 Stress-strain curve for ultra-fine-grained polycrystalline nickel-based superalloy varying the grain size at 300 K

After the elastic region materials start to deform plastically following the mechanisms within the grain boundary, i.e. grain boundary sliding. Plastic deformation becomes less distinguishable when the grain size decrease. This plastic deformation can be a concomitant act of dislocation activity and a significant amount of grain sliding and rotation. The study showed that grain boundary sliding or rotation is mainly responsible for most of the plastic deformation in nanocrystalline materials [93]. While the grain size increases, dislocation activity plays a dominant role instead of grain sliding in the region of the plastic deformation, therefore the yield strength of the materials also increases.

The increasing grain-boundary to volume ratio with the grain-boundary related plasticity with decreasing grain size is the reason for the inverse Hall–Petch relationship. This is in a good agreement with the study where an inverse Hall-Patch slope was generated with intensified grain boundary sliding below a critical grain size using MD predictions for FCC metals [94], [95]. This generated slope was different from conventional deformation and fracture mechanisms. The study reveals how the Hall-Petch relationship fails to explain the deformation mechanism when the grain size is reduced into the nanometer regime. Since the grains are too small, the pileup of dislocation is incapable of being a hardening mechanism anymore, resulting in grain boundary sliding as a possible option for plastic deformation in nanocrystalline metals [94]. Some MD simulations have been performed before on this phenomenon on different grain size samples while having the same random grain orientation, for example, Vo et al. [96].

Another major parameter for the decrease in stress and starting the plastic deformation earlier while grain size decrease is the nucleation of dislocation. The grain boundaries act as source and sink for dislocation inside the grain. Hence, finer grain boundaries permit more dislocation segments. This phenomenon can be described from Figure 30. This figure indicates

that different partial dislocation segments are increasing while the grain size is reducing. The sample with a larger grain size of 16 nm (Figure 30(a)) are making very few dislocation segments in the grain boundaries, whereas in the sample with the smallest grain-size of 5 nm are producing a much larger number of dislocation segments. As a result, frequent interaction of grain boundary and dislocation are taking place in fine-grained nanocrystalline nickel-based superalloy.

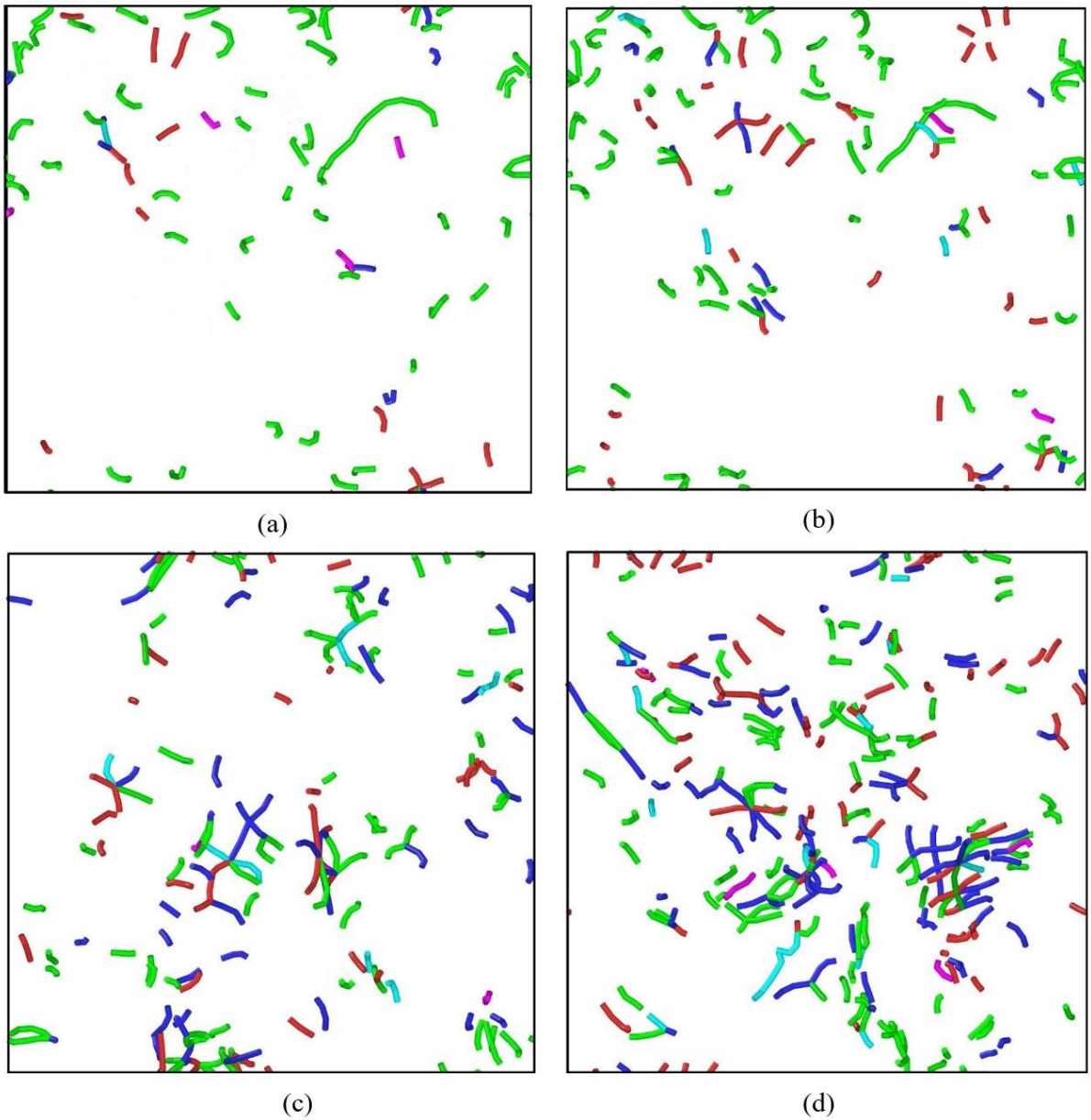

Figure 30 Dislocation multiplication with finer grain size at 300 K for (a) 16 nm (b) 9.54 nm (c) 7.5 nm (d) 5 nm grain size

Dislocation activity: dislocation density analysis. In this section the contributions of the grain sizes on dislocation density and yield strength will be discussed. The total shear strain inside the material can be composed of three components:

$$\varepsilon_t = \varepsilon_e + \varepsilon_d + \varepsilon_{GB}$$

where ε_e is the elastic strain, ε_d is the part of strain that is contributed by dislocations and ε_{Gb} is the part of strain that is contributed by grain boundary sliding. Again, the dislocation density ρ can be written as,

$$\rho = \frac{n}{d^2}$$

where n is denoted as the total number of dislocations in a grain of diameter d. we can assume that the plastic deformation $(\varepsilon_t - \varepsilon_e)$ is completely resulted by dislocation movement, the dislocation density ρ can be calculated theoretically from the above equations [97]. Figure 31 is presenting the change in dislocation density and yield strength by varying the grain size. The dislocation density is increasing from $2X10^{25}$ m^{-2} to $1.5X10^{26}$ m^{-2} with a corresponding increase in the yield strength from 2.1 GPa to 4.7 GPa. The dislocation density was determined straight from the atomistic simulation results to calculate the real contribution of dislocations quantitatively to plastic deformation in our nickel-based ultra-fined nanocrystalline superalloy. For this purpose, we have used the algorithm and software tool DXA developed by Stukowski and Albe [63].

Increasing dislocation density with increasing grain size is an indication of a large number of dislocation generation and motion during plastic deformation. This value is contradicting our theoretical equation where dislocation density should be inversely proportional to the grain diameter. This may occur because the grain-boundary dislocations contributions are also included the computed dislocation density and we are not separating other deformation

mechanisms i.e. grain boundary sliding that also contributes to the plastic deformation. The necessary dislocation density will vary from the calculated values, if plastic deformation also occurs by grain-boundary movement. Above all, for small grain sizes, notable grain-boundary dislocations could also be observed. Additionally, the orientation factor is another element that can take part in dislocation density increment due to the dislocation movement in more than one slip plane. Finally, it is understandable that the plastic deformation is concomitant of both dislocation movement and grain boundary sliding in a condition for grain sizes smaller than 30 nm. In our present work, we will try to discuss about some of the deformation mechanism that might be responsible for the inverse Hall-Patch phenomenon in our sample. Two major activities are dislocation diffusion and grain boundary thickening.

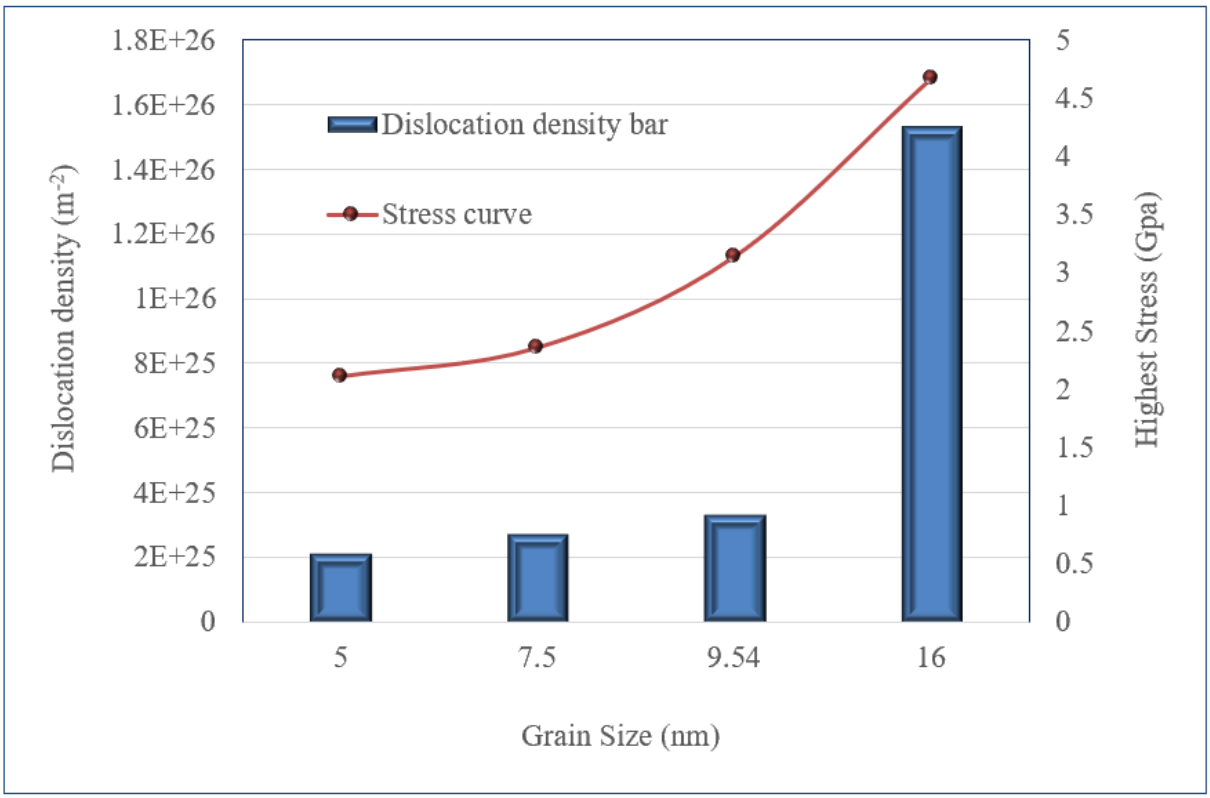

Figure 31 Dislocation density and highest stress variation with respect to different grain size at 300 K

Grain boundary activity: dislocation diffusion. To represent the creep process, the involvement of few deformation mechanisms can be considered. One of them is the dislocation diffusion into the grain boundary. The initial and final configurations of such diffusion processes are shown in Figure 32. The diffusion process of the sample has been observed to find out the operating deformation mechanisms so that we can analyze quantitatively the role of grain boundaries during compressive deformation of nickel-based fine-grained nanocrystal.

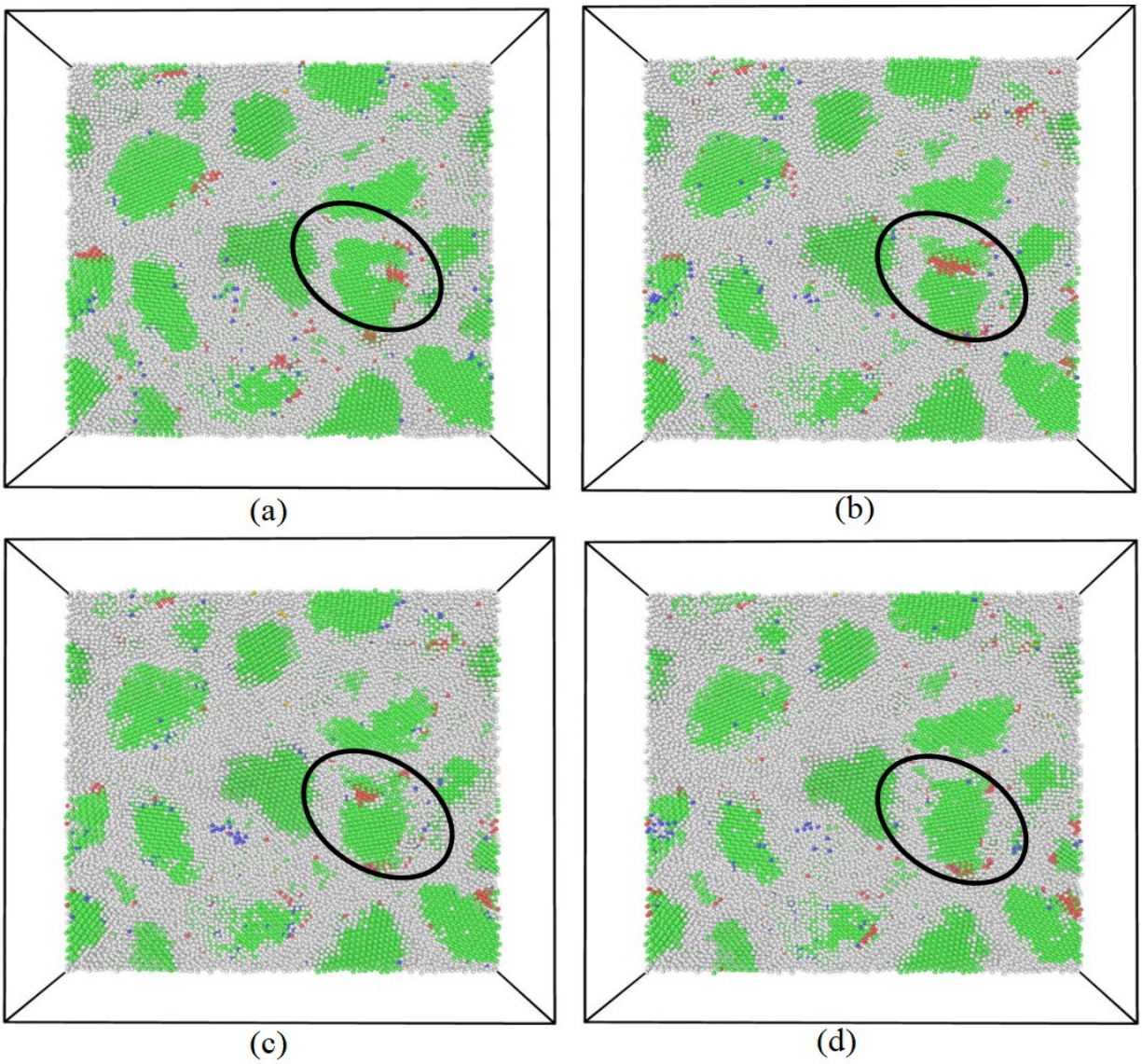

Figure 32 Dislocation diffusion to the grain boundary in the nanocrystal sample with average grain size 7.5 nm at 300 K (a) 8 ps (b) 11 ps (c) 16 ps (d) 18 ps

We have identified and separated the atoms with color-coding at the grain boundaries and inside the grains by determining the local crystalline order to make the simulation analysis ease [98], [99]. Atoms 'inside' the grains are in local face-centered cubic order (green color); atoms in local hexagonal close-packed order are considered as stacking faults (red color), and all the remaining atoms are considered as part of the grain boundaries (white color). In the grain of Figure 32(a) a few stacking faults have been emerged (refers to the marked grain), which means dislocation is starting to propagating from the grain boundary. The appearance of stacking faults is the indication of dislocation activity within the grains. Dislocations begin to progress across the grains and continues toward the next grain boundary [Figure 32(b)]. Gradually dislocation proceeds towards the grain boundary and successfully diffused in the next grain boundary, resulting in a deformed face-centered cubic grain [Figure 32(c), Figure 32(d)]. The shape of the crystal grain did not change much despite the obvious atomic diffusion at the grain boundary. Looking at the other grains of the snapshot, we can see that almost all the deformation occurs in the grain. Just like the nickel-based single crystal superalloy, that we discussed in previous section, a partial dislocation is emerged from a grain boundary and continues to move through a grain.

We can relate the deformation mechanism of the grain boundary with diffusional mass transport along the boundaries because the atoms in a grain-boundary are loosely organized. At room temperature diffusion mechanisms can play an important role to the deformation considerably as claimed by the deformation mechanism map for polycrystalline face-centered cubic metal [100]. The grain-boundary contribution to the creep rate was studied by Burton and Greenwood [101] at low-temperature range and found to be the dominant reason for the deformation. Though dislocation diffusion in fine-grained nanocrystal plays a minor part in the

event of the total deformation, they are necessary to permit for deformations of the grains in the absence of diffusion, as they slide past each other.

Our polycrystal superalloy structure has multiple γ' phases inside each grain. But we should note that when the volume fraction of the particles is comparatively small, second phase particles cannot control the lattice diffusion much. Nevertheless, the pinning of the grain boundary dislocations can take place due to the presence of the second phase particles on grain boundaries, which will influence the diffusional creep. In some cases, interaction may take place between second phase particles and grain boundary dislocations in the same way lattice dislocation interacts with matrix. Hence, the movement of mobile dislocations will be difficult because of the presence of these particles, and to make the dislocations move, a threshold stress must be overcome.

Grain boundary activity: thickening. The present discussion reveals the conductance of reverse Hall–Petch effect, which can be caused by grain boundary sliding without any thermally activated processes. We can point out that some considerable action has taken place inside the grain by seeing the Figure 33, which is illustrating how the grain boundaries have grown thicker and showing the schematic illustration of the grain-boundary deformation model by associating a diffusion mechanism. The atomistic configuration of a nanocrystalline nickel-based superalloy sample with a grain size of 16 nm has been presented after minimization (at t=0ps) in Figure 33(a). All the defined grain boundaries and the minute presence of stacking faults are clearly visible in the snapshot. Grain boundary thickening starts to be noticeable in Figure 33(b), which indicates the grain boundary diffusion in the structure currently. At t=18 ps the thickening of the grain boundary is observed with the accommodation of more diffusion in the grain boundary in conjunction with slight contraction of grain along the direction of applied compression loading.

This thickening phenomenon takes place due to the diffusion of the atoms to the boundaries of the grain from the inside of the grain. In addition to the fine grain size, applied compression along the grain axis triggers the atoms to travel. This mechanism of creep in nanocrystalline superalloy materials has been studied before [102].

Fine-grained nanocrystalline materials have a larger volume fraction of grain boundaries, which is responsible for the generation of dislocation that stimulates the diffusion creep mechanism. Deformation in ultra-fine-grained polycrystalline may occur by diffusion of defects [103]–[105] either through the lattice (Nabarro–Herring) or along grain boundaries (Coble) if dislocation activity is limited, which is the process referred as diffusion creep that require matter transport. Comparing the possible kinetic regimes of polycrystals with small grain size exhibits a huge number of diversity than larger grained polycrystals that is used in grain boundary diffusion experiments generally. The grain boundary migration of small-grained materials can be remarkable because of the unstable structure even at room temperature. Altogether, these findings demonstrate that for nanocrystalline nickel-based superalloy with small grain size, diffusion creep is one of the deformations controlling mechanisms.

Additionally, the amorphous volume fraction continuously increases with time during the creep process, which is a supportive occurrence for atomic diffusion. However, an increase in the volume fraction of grain boundaries with a decrease of grain size demonstrates rapid diffusion of the atoms positioned at the grain boundaries [82]. A larger fraction of the atoms is being introduced to the grain boundaries with the reduced grain size, resulting in an easier grain boundary sliding and ultimately soften the material with a high probability of being an amorphous structure. Our observed deformation in nickel-based polycrystalline superalloy is anyway close to the deformation of grain boundaries in superplastic deformation [106]. In fact,

low temperature superplasticity is an important and technologically influential observations in nanocrystalline materials. In fact, atomistic pictures can deliver additional confirmation for that conclusion.

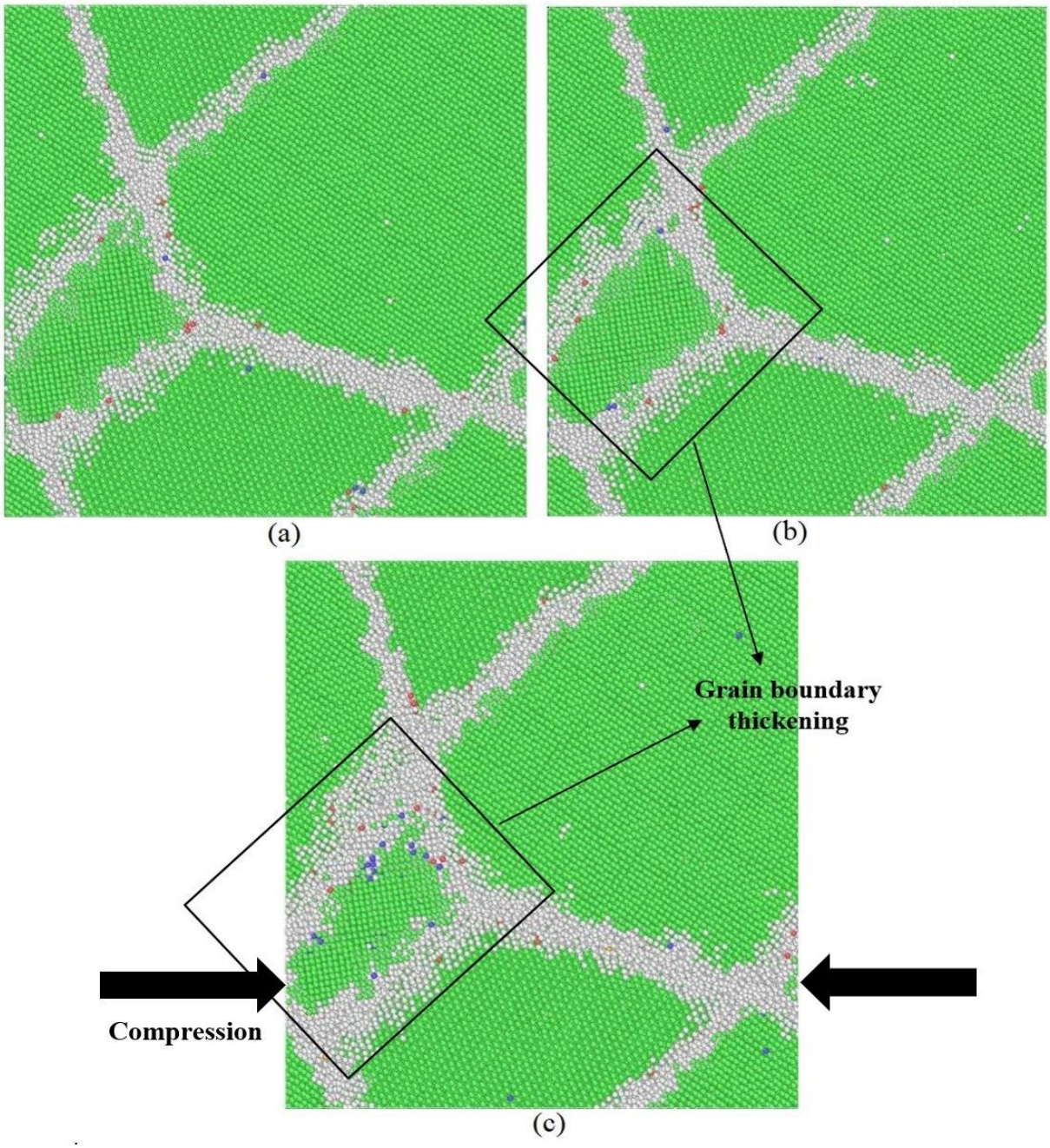

Figure 33 Atomistic configurations of nickel-based polycrystalline superalloy sample with grain size of 16 nm at 300 K (a) at 0 ps (b) at 5.5 ps (c) at 18 ps

Figure 34 is showing the atomic configurations of nanocrystalline nickel-based superalloy, how the grain diffusion or in other words, the grain boundary thickening varies with grain size at 300K temperature. All the four different samples with grain size 16 nm, 9.54 nm, 7.5 nm, and 5 nm are presenting changes in grain boundary thickness at t = 18 ps. Figure 34(a) is

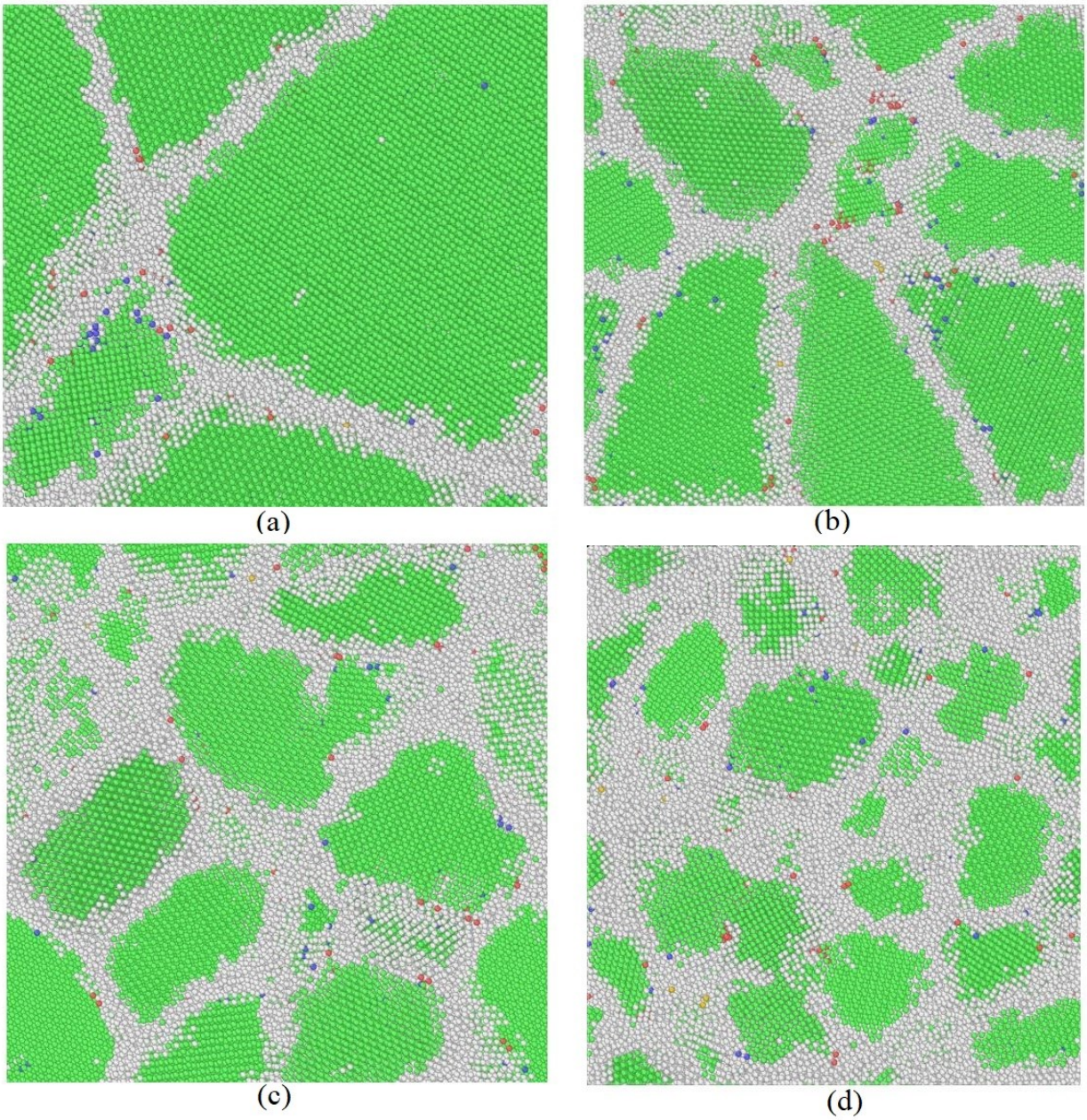

Figure 34 Atomistic configurations of nickel-based polycrystalline superalloy sample at 18 ps at 300 K with average grain size (a) 16 nm (b) 9.54 nm (c) 7.5 nm (d) 5 nm

representing the atomic configuration of the sample with an average grain size 16 nm, which is indicating the grain boundary thickening of this nanocrystalline sample. Figure 34(b) is showing a significant difference comparing to the previous sample. Relatively more grain boundary thickening and more stacking faults are present in this structure. This is expected since the higher volume fraction of grain boundaries is favorable to grain diffusion. When the grain size is smaller than the previous two samples (see, Figure 34(c)), diffusion along the grain boundary is obvious to be increased. This system is indicating a continuous occurrence of grain boundary diffusion. Lastly, in the sample with grain size 5 nm (refer to Figure 34(d)), extreme diffusion of atoms can be observed in the sample, resulting in a huge grain boundary thickening phenomenon.

This reveals the factor that under high strain rate and low temperature, grain boundary diffusion plays a dominating role in creep mechanism while dislocation nucleation intensifies the process as a supporting mechanism. In general, dislocation glide and climb become activated at high temperature, hence the effect of these two mechanisms were neglected. However, grain growth is another part that cannot be ignored but given the length and timescale considered. Due to the limited timescale considered in the work, this mechanism could not be observed.

Data Mining (WEKA)

We used WEKA machine learning workbench for the automatic classification of our research data. Multilayer perception algorithm has been used with 2(two) hidden layers using the training set. Also, the result was confirmed by using 10-fold cross-validation. Figure 35 is showing WEKA simulated results in comparison with our MD-simulated data. By classifying the data, we found a 97.86% correlation between experimentally gained stress values and predicted

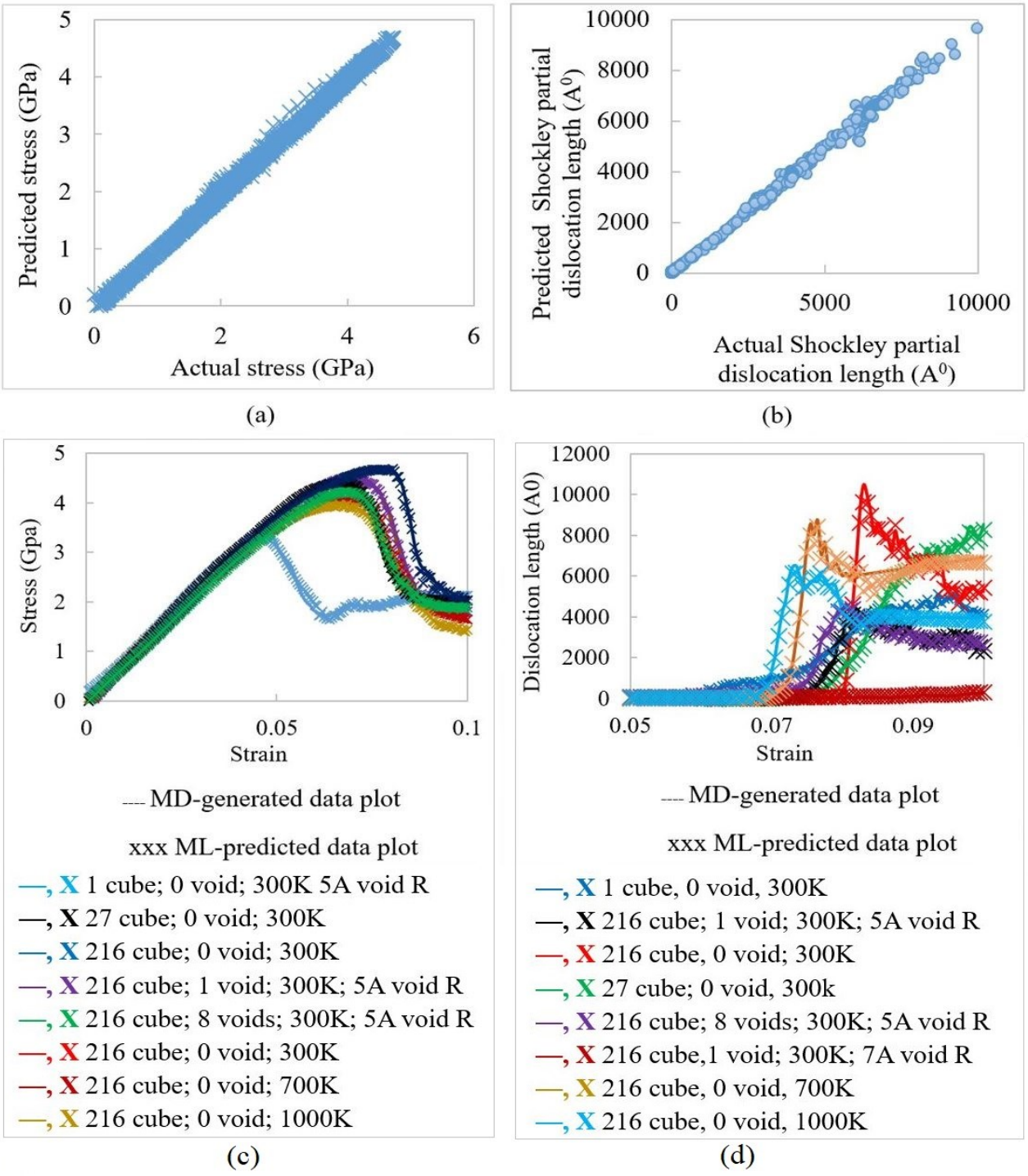

Figure 35 (a) Actual stress data vs predicted stress data (b) Actual Shockley length data vs predicted Shockley length data (c) Overlapped stress vs strain curve with actual stress and predicted stress (d) Overlapped dislocation length vs strain curve with actual dislocation length vs strain curve

stress values, where mean absolute error is 0.2942 [Figure 35 (a)]. By superimposing the MD-

generated data plot of strain-stress graph with ML-predicted data plot of strain-stress graph in Figure 35(c) proves the high percentage of correlation between these two data. By following the same procedure for Shockley partial dislocation length, 98.85% correlation was found between MD-generated and ML-predicted data [Figure 35 (b)]. Also, the superimposing of two plot of dislocation length vs strain was shown in Figure 35(d).

CONCLUSION

In the first part of this dissertation, a detailed analysis of the dislocation dynamics of single-crystal nickel-base superalloy was done under compressive loading with a constant $5X10^9$ s^{-1} strain rate at 300 K. Changes in the dislocation evolution were analyzed varying different parameters i.e. strain, temperature, defect, reinforcing phase size and distribution. Results showed that lower strain rate decreases the yield strength of materials and enhance the deformation of the material earlier. Slower strain rate allows enough time to the atoms for rearranging themselves into a lower energy level by moving from their position and dislocation starts somewhat earlier. However, a very high strain rate will tear the material before the dislocation can even nucleate. Therefore, we utilized a safe strain rate of $5X10^9$ s^{-1}, and kept it constant for our further investigation. The addition of high temperatures with a high strain rate decreases the creep resistance of the superalloy. Increasing the temperature from 300 K to 1000 K decreases the yield strength of the system, also dislocation starts to nucleate at a lower strain value. It is evident that with increasing temperature different softening mechanism starts acting and dislocation becomes thermally activated, resulting dislocation to cut through the γ' phase which is the hardest phase in nickel-based superalloy.

Molecular dynamics simulations in nickel-based single crystal superalloy were conducted to study the evolution of void growth and dislocation dynamics around the void surface. We have employed single-void and multiple-void into our systems to analyze the inter-void interference-effect. Additionally, dislocation nucleation and propagation with dislocation density identifying different types of partial dislocation were also investigated. The brief conclusions of the study are: the free surfaces of the voids are the sites of the initial dislocation nucleation as the stress concentration in the void surface is highest, and the atoms on and near-surface are easier to move

due to some loss of atoms. Therefore, dislocation nucleates and expands as a semicircular loop around the void surface.

Calculating the dislocation density, we found a relationship between the evolution of the dislocation density and the stress-strain curve. At the initial stage of the compressive loading, the dislocation density increases very slowly and consists of Shockley partial dislocation only. Upon continuous loading, the dislocation growth rate increases suddenly at a certain strain value (different value for different conditions) with a sharp declination of the stress-strain curve. Therefore, comparison amongst three different sample with no void, single void, and multiple voids in terms of dislocation density reveals that dislocation density is highest in the system with no-void, whereas the system with multiple-void has lowest dislocation density because of the dislocation interaction emerge from multiple void sites in different direction.

Between the two phases of nickel-based superalloy, gamma-prime (γ') is the hardest phase. Variation in the γ' phase i.e. volume fraction, number, size, and distribution can significantly affect the dislocation dynamics of the materials, hence influence the creep behavior. We have varied the number of total reinforcing phases and their distribution inside the material, keeping the volume fraction constant, which is 51%. Our analysis revealed that the higher number and highly distributed γ' phase increases the yield strength of the system and make the dislocation to evaluate later. While investigating the dislocation dynamics in the system with only one γ' cubes in the middle of the system, we found the dislocation to nucleate from the corner of the γ/γ' interface where the stress concentration highest. At the initial stage of loading, the dislocation network basically nucleates and expands in the γ matrix. As the loading continues, the dislocation network accumulates in the γ/γ' interphase creating a loop, makes the stress concentration very high at that location, ultimately cutting through the γ' phase.

Since the nickel-based superalloy is comprised of two phases and both are face-centered cubic structure, dislocations are found to move through the [111] plane, which is the most close-packed plane of a face-centered cubic structure, hence the slip plane. As a result, all the partial dislocation produces inside the system is of the same classification, no matter how we change the loading environment. However, the density of the different types of partial dislocation may changes with time and conditions. For face-centered cubic structure, Shockley partial dislocation is the most common partial dislocation, that takes place because of the stacking fault. Some other partial dislocation also appeared with lower density, such as Hirth partial dislocation, Frank partial dislocation, Stair-rod partial dislocation, and Perfect dislocation. The simulated results were consistent with those referred to work using experimental calculations. Our theoretical understanding and analysis of creep properties and microstructural evolution of nickel-based single crystal superalloys should help in designing and testing for structural applications.

In the later part of our dissertation, we have focused on the deformation mechanism of nickel-based polycrystalline superalloy. We have created four ultra-fine-grained polycrystalline samples using Voronoi tessellation method in Atomsk, with average grain size 16 nm, 9.54 nm, 7.5 nm, and 5 nm. This study which involves the use of fine-grained polycrystalline samples, under compressive loading, reveals that larger grains provide higher yield strength and better creep resistance. However, in practice and increase in hardness and yield strength with decreasing grain size is observed, which is referred by the Hall–Petch effect, and is known to occur by the formation of pile-up of dislocation into the grain boundaries, hence obstruct the motion of dislocations as the grains get smaller. The grain sizes in the present simulations are in the ultra-fine regime, where the Hall–Petch effect is observed to act reverse. Numerous researchers suggested several mechanisms for this reverse Hall–Petch effect, such as grain

boundary migration, grain boundary diffusion, suppression of dislocation pile-ups, grain boundary sliding, dislocation motion through multiple grains, and high diffusional creep in the grain boundaries. Thus, we inferred that the decrease in stresses with decreases grain size is the result of the inverse Hall-Patch effect and occurs due to the large contribution of deformation mechanisms from grain boundary diffusion or sliding. Grain boundary involvement in plasticity is higher for the fine grain-sized system because of the large grain boundary to volume ratio, resulting in a lower yield strength. With increased grain size, dislocations density from grain boundaries increases, which dominates the rather than the grain boundary, hence increase the yield strength. The obvious involvement of the grain boundary in the deformation for our fine-grained nickel-based polycrystalline sample can be observed from both the grain boundary thickening phenomenon and dislocation multiplication.

It is worth noting that our findings agree with the probable creep mechanisms suggested by some other researchers, that we have referred already in the corresponding sections while discussing our simulated results. These analyses also validate the important role of grain boundary diffusion and lattice diffusion in nanocrystalline nickel-based superalloy. We cannot, however, detect a traverse to the normal Hall–Petch regime from this inverse relationship at larger grain sizes in our simulations, due to the huge computational expense for larger sized grained samples. For the same reason, we cannot differentiate straight with the deformation mechanism of the bulk material. While comparing the simulated strain–stress curves and experimental curves, yield stress is the important parameter that is somewhat twice in the simulated curve than the curve from experiments on low-defected samples. In practice, producing ultra-fine-grained polycrystalline nickel-based superalloy is not easy. Additionally, experimentally fabricated nanocrystalline samples generally contain voids and surface defects,

resulting in a reduced yield strength of the material. An extensive caution should be taken while comparing the experimental and simulation results.

FUTURE WORK

Bicrystal Simulations

Grain boundaries are considered as very important features in materials because they can alter the mechanism responsible for the mechanical behavior. Between two crystals, many configurations of grain boundaries may exist. Amongst them, some predefined grain boundary configurations can be applied for simulation. For example, tilt boundaries have a large influence on the dislocation dynamics and the creep resistance of the bicrystal nickel-based superalloy. Additionally, we can incorporate a void at the grain boundary to compare dislocation dynamics on both the void surface and the grain boundary.

Simulation of Polycrystalline

Since we have already generated nickel-based nanocrystal superalloy structures using Atomsk for our present study, we can vary the grain size and create a plot showing the effect of grain size from a very larger size range to the very small grain size. Also, we can randomize grain orientations to analyze the difference in creep mechanism depending on the orientation. In that case, we should choose the size of the simulation domain as large as the computational capacity permits. The extension of a further study toward a varying degree of grain size will allow us to systematically evaluate the interplay between the role of grain boundaries (when the structure is of nano-scale) to the role of bulk portion (when the structure is of micro-meter size).

Strain Rate in Polycrystalline

Strain rates are seemed to affect the yield stress significantly in single crystals nickel-based superalloy. It would be interesting to see the deformation behavior of polycrystalline

structure at different strain rates, as a deformation mechanism might not be the same with increasing or decreasing strain rate.

Voids in Polycrystalline Structure

Another important endeavor is to study the creep mechanism of nanocrystalline samples that contain large amounts of porosity or voids within the structure, most importantly, inside the grain boundaries. These voids play a major role in the creep resistance and mechanical properties of the materials. Combining with the grain boundaries, these voids can influence the dynamics of the dislocations within the material. A comparison of MD simulations by incorporating voids inside the system, keeping other parameters constant, can allow an opportunity to understand the influence of voids on the strength of nickel-based polycrystalline superalloys.

Adding Alloying Elements

In this dissertation, we have worked with two phases of superalloy, whereas nickel-based superalloy can have some more phases also depending on the multi-components included in the alloys. We can add some additional alloying elements to observe the effect of additional phases and elements i.e. tertiary phases, carbides. Adding alloying elements should alter the dislocation dynamics and influence the creep mechanism in general, but presumably more so in the tertiary zone of the creep.

REFERENCES

[1] T. Murakumo, T. Kobayashi, Y. Koizumi, and H. Harada, "Creep behaviour of Ni-base single-crystal superalloys with various γ′ volume fraction," Acta Mater., vol. 52, no. 12, pp. 3737–3744, Jul. 2004.

[2] J. R. Davis and D. & Associates, "© 2000 ASM International. All Rights Reserved. ASM Specialty Handbook: Nickel, Cobalt, and Their Alloys (#06178G) www.asminternational.org," 2000.

[3] Y. Zhu, Z. Li, and M. Huang, "Atomistic modeling of the interaction between matrix dislocation and interfacial misfit dislocation networks in Ni-based single crystal superalloy," Comput. Mater. Sci., vol. 70, pp. 178–186, Apr. 2013.

[4] M. A. Meyers, A. Mishra, and D. J. Benson, "Mechanical properties of nanocrystalline materials," Prog. Mater. Sci., vol. 51, no. 4, pp. 427–556, May 2006.

[5] P. Erhart, E. M. Bringa, M. Kumar, and K. Albe, "Atomistic mechanism of shock-induced void collapse in nanoporous metals," Phys. Rev. B - Condens. Matter Mater. Phys., vol. 72, no. 5, pp. 2–5, 2005.

[6] E. M. Lehockey and G. Palumbo, "On the creep behaviour of grain boundary engineered nickel 1," Mater. Sci. Eng. A, vol. 237, no. 2, pp. 168–172, Sep. 1997.

[7] R. R. Unocic, G. B. Viswanathan, P. M. Sarosi, S. Karthikeyan, J. Li, and M. J. Mills, "Mechanisms of creep deformation in polycrystalline Ni-base disk superalloys," Mater. Sci. Eng. A, vol. 483–484, no. 1-2 C, pp. 25–32, 2008.

[8] D. Locq, P. Caron, S. Raujol, A. Coujou, and N. Clément, "on the Role of Tertiary Γ ′ Precipitates in the Creep Behaviour At 700 ° C of a Pm Disk Superalloy," 2004.

[9] G. B. Viswanathan, P. M. Sarosi, D. H. Whitis, and M. J. Mills, "Deformation mechanisms at intermediate creep temperatures in the Ni-base superalloy René 88 DT," Mater. Sci. Eng. A, vol. 400–401, pp. 489–495, Jul. 2005.

[10] S. Ha and K. Kim, "Void growth and coalescence in f.c.c. single crystals," Int. J. Mech. Sci., vol. 52, no. 7, pp. 863–873, Jul. 2010.

[11] Y. Alinaghian, M. Asadi, and A. Weck, "Effect of pre-strain and work hardening rate on void growth and coalescence in AA5052," Int. J. Plast., vol. 53, pp. 193–205, Feb. 2014.

[12] R. A. Lebensohn, J. P. Escobedo, E. K. Cerreta, D. Dennis-Koller, C. A. Bronkhorst, and

J. F. Bingert, “Modeling void growth in polycrystalline materials,” Acta Mater., vol. 61, no. 18, pp. 6918–6932, Oct. 2013.

[13] W. H. Liu, X. M. Zhang, J. G. Tang, and Y. X. Du, “Simulation of void growth and coalescence behavior with 3D crystal plasticity theory,” Comput. Mater. Sci., vol. 40, no. 1, pp. 130–139, Jul. 2007.

[14] M. J. Nemcko, H. Qiao, P. Wu, and D. S. Wilkinson, “Effects of void fraction on void growth and linkage in commercially pure magnesium,” Acta Mater., vol. 113, pp. 68–80, Jul. 2016.

[15] A. Srivastava and A. Needleman, “Effect of crystal orientation on porosity evolution in a creeping single crystal,” Mech. Mater., vol. 90, no. February, pp. 10–29, 2015.

[16] L. Farrissey, M. Ludwig, P. E. McHugh, and S. Schmauder, “An atomistic study of void growth in single crystalline copper,” Comput. Mater. Sci., vol. 18, no. 1, pp. 102–117, 2000.

[17] J. Segurado and J. LLorca, “Discrete dislocation dynamics analysis of the effect of lattice orientation on void growth in single crystals,” Int. J. Plast., vol. 26, no. 6, pp. 806–819, 2010.

[18] L. Xiong, D. L. McDowell, and Y. Chen, “Nucleation and growth of dislocation loops in Cu, Al and Si by a concurrent atomistic-continuum method,” Scr. Mater., vol. 67, no. 7–8, pp. 633–636, Oct. 2012.

[19] H. J. Chang, J. Segurado, and J. LLorca, “Three-dimensional dislocation dynamics analysis of size effects on void growth,” Scr. Mater., vol. 95, no. 1, pp. 11–14, 2015.

[20] Y. Zhang, S. Jiang, X. Zhu, and Y. Zhao, “Dislocation mechanism of void growth at twin boundary of nanotwinned nickel based on molecular dynamics simulation,” Phys. Lett. A, vol. 380, no. 35, pp. 2757–2761, Aug. 2016.

[21] M. F. Horstemeyer, M. I. Baskes, and S. J. Plimpton, “Length scale and time scale effects on the plastic flow of fcc metals,” Acta Mater., vol. 49, no. 20, pp. 4363–4374, 2001.

[22] G. P. Potirniche, M. F. Horstemeyer, G. J. Wagner, and P. M. Gullett, “A molecular dynamics study of void growth and coalescence in single crystal nickel,” Int. J. Plast., vol. 22, no. 2, pp. 257–278, 2006.

[23] L. Yuan, D. Shan, and B. Guo, “Molecular dynamics simulation of tensile deformation of nano-single crystal aluminum,” J. Mater. Process. Technol., vol. 184, no. 1–3, pp. 1–5, 2007.

[24] K. J. Zhao, C. Q. Chen, Y. P. Shen, and T. J. Lu, “Molecular dynamics study on the nano-void growth in face-centered cubic single crystal copper,” Comput. Mater. Sci., vol. 46, no. 3, pp. 749–754, 2009.

[25] E. M. Bringa, S. Traiviratana, and M. A. Meyers, “Void initiation in fcc metals: Effect of loading orientation and nanocrystalline effects,” Acta Mater., vol. 58, no. 13, pp. 4458–4477, 2010.

[26] C. Carry and J. . Strudel, “Apparent and effective creep parameters in single crystals of a nickel base superalloy—I Incubation period,” Acta Metall., vol. 25, no. 7, pp. 767–777, Jul. 1977.

[27] C. Mayr, G. Eggeler, and A. Dlouhy, “Analysis of dislocation structures after double shear creep deformation of CMSX6-superalloy single crystals at temperatures above 1000 °C,” Mater. Sci. Eng. A, vol. 207, no. 1, pp. 51–63, Mar. 1996.

[28] T. M. Pollock and A. S. Argon, “Creep resistance of CMSX-3 nickel base superalloy single crystals,” Acta Metall. Mater., vol. 40, no. 1, pp. 1–30, Jan. 1992.

[29] M. Feller-Kniepmeier and T. Link, “Correlation of Microstructure and Creep at Medium and High Temperatures in < 100> Oriented Crystals of Superalloy SPR 99,” Adv. Plast. 1989, pp. 353–356, Jan. 1989.

[30] D. F. Lahrman, R. D. Field, R. Darolia, and H. L. Fraser, “Investigation of techniques for measuring lattice mismatch in a rhenium containing nickel base superalloy,” Acta Metall., vol. 36, no. 5, pp. 1309–1320, May 1988.

[31] Z. T. Trautt, A. Adland, A. Karma, and Y. Mishin, “Coupled motion of asymmetrical tilt grain boundaries: Molecular dynamics and phase field crystal simulations,” Acta Mater., vol. 60, no. 19, pp. 6528–6546, 2012.

[32] L. Müller, U. Glatzel, and M. Feller-Kniepmeier, “Calculation of the internal stresses and strains in the microstructure of a single crystal nickel-base superalloy during creep,” Acta Metall. Mater., vol. 41, no. 12, pp. 3401–3411, Dec. 1993.

[33] V. Sass, U. Glatzel, and M. Feller-Kniepmeier, “Anisotropic creep properties of the nickel-base superalloy CMSX-4,” Acta Mater., vol. 44, no. 5, pp. 1967–1977, May 1996.

[34] A. KOSTKA, G. MÄLZER, and G. EGGELER, “High-temperature dislocation plasticity in the single-crystal superalloy LEK94,” J. Microsc., vol. 223, no. 3, pp. 295–297, Sep. 2006.

[35] A. Epishin and T. Link, “Mechanisms of high temperature creep of nickel base

superalloys," Superalloys, pp. 137–143, 2004.

[36] T. Link, A. Epishin, M. Klaus, U. Brückner, and A. Reznicek, "〈1 0 0〉 Dislocations in nickel-base superalloys: Formation and role in creep deformation," Mater. Sci. Eng. A, vol. 405, no. 1–2, pp. 254–265, Sep. 2005.

[37] G. Eggeler and A. Dlouhy, "On the formation of 〈010〉 -dislocations in the γ′-phase of superalloy single crystals during high temperature low stress creep," Acta Mater., vol. 45, no. 10, pp. 4251–4262, Oct. 1997.

[38] P. Caron, T. Khan, and P. Veyssière, "On precipitate shearing by superlattice stacking faults in superalloys," Philos. Mag. A, vol. 57, no. 6, pp. 859–875, Jun. 1988.

[39] M. Kamaraj, "Rafting in single crystal nickel-base superalloys — An overview," Sadhana, vol. 28, no. 1, pp. 115–128, 2003.

[40] R. . Fleischer, "Substitutional solution hardening," Acta Metall., vol. 11, no. 3, pp. 203–209, Mar. 1963.

[41] P. Lukáš, J. Čadek, V. Šustek, and L. Kunz, "Creep of CMSX-4 single crystals of different orientations in tension and compression," Mater. Sci. Eng. A, vol. 208, no. 2, pp. 149–157, Apr. 1996.

[42] V. Sass and M. Feller-Kniepmeier, "Orientation dependence of dislocation structures and deformation mechanisms in creep deformed CMSX-4 single crystals," Mater. Sci. Eng. A, vol. 245, no. 1, pp. 19–28, Apr. 1998.

[43] V. Sass, U. Glatzel, and M. Feller-Kniepmeier, "Anisotropic creep properties of the nickel-base superalloy CMSX-4," Acta Mater., vol. 44, no. 5, pp. 1967–1977, May 1996.

[44] G. R. Leverant and B. H. Kear, "The mechanism of creep in gamma prime precipitation-hardened nickel-base alloys at intermediate temperatures," Metall. Mater. Trans. B, vol. 1, no. 2, pp. 491–498, 1970.

[45] R. A. MacKay and R. D. Maier, "The influence of orientation on the stress rupture properties of nickel-base superalloy single crystals," Metall. Trans. A, vol. 13, no. 10, pp. 1747–1754, 1982.

[46] G. R. Leverant, B. H. Kear, and J. M. Oblak, "Creep of precipitation-hardened nickel-base alloy single crystals at high temperatures," Metall. Trans., vol. 4, no. 1, pp. 355–362, 1973.

[47] G. R. Leverant, B. H. Kear, and J. M. Oblak, "The influence of matrix stacking fault

energy on creep deformation modes in Γ' precipitation-hardened nickel-base alloys," Metall. Mater. Trans. B, vol. 2, no. 8, pp. 2305–2306, 1971.

[48] J. Svoboda and P. Lukáš, "Modelling of recovery controlled creep in nickel-base superalloy single crystals," Acta Mater., vol. 45, no. 1, pp. 125–135, Jan. 1997.

[49] M. Kolbe, K. Neuking, and G. Eggeler, "Dislocation reactions and microstructural instability during 1025 °C shear creep testing of superalloy single crystals," Mater. Sci. Eng. A, vol. 234–236, pp. 877–879, Aug. 1997.

[50] C. Mayr, G. Eggeler, G. A. Webster, and G. Peter, "Double shear creep testing of superalloy single crystals at temperatures above 1000 °C," Mater. Sci. Eng. A, vol. 199, no. 2, pp. 121–130, Aug. 1995.

[51] H. Y. Song, S. Li, and Q. Deng, "Coupling effects of thickness and aspect ratio on deformation behavior of Cu50Zr50 metallic glass," Comput. Mater. Sci., vol. 139, pp. 106–114, Nov. 2017.

[52] H. Y. Song, S. Li, Y. G. Zhang, Q. Deng, T. H. Xu, and Y. L. Li, "Atomic simulations of plastic deformation behavior of Cu50Zr50 metallic glass," J. Non. Cryst. Solids, vol. 471, pp. 312–321, Sep. 2017.

[53] W.-P. Wu, Y.-F. Guo, Y.-S. Wang, R. Mueller, and D. Gross, "Molecular dynamics simulation of the structural evolution of misfit dislocation networks at γ/γ′ phase interfaces in Ni-based superalloys," Philos. Mag., vol. 91, no. 3, pp. 357–372, Jan. 2011.

[54] P. Hirel, "Atomsk: A tool for manipulating and converting atomic data files," Comput. Phys. Commun., vol. 197, pp. 212–219, Dec. 2015.

[55] S. Plimpton, "Fast Parallel Algorithms for Short-Range Molecular Dynamics," J. Comput. Phys., vol. 117, no. 1, pp. 1–19, Mar. 1995.

[56] D. J. Evans and B. L. Holian, "The Nose–Hoover thermostat," J. Chem. Phys., vol. 83, no. 8, pp. 4069–4074, Oct. 1985.

[57] D. H. Tsai, "The virial theorem and stress calculation in molecular dynamics," J. Chem. Phys., vol. 70, no. 3, pp. 1375–1382, Feb. 1979.

[58] Y. Mishin, D. Farkas, M. J. Mehl, and D. A. Papaconstantopoulos, "Interatomic potentials for monoatomic metals from experimental data and ab initio calculations," Phys. Rev. B, vol. 59, no. 5, pp. 3393–3407, Feb. 1999.

[59] Y. Mishin, "Atomistic modeling of the γ and γ′-phases of the Ni–Al system," Acta Mater.,

vol. 52, no. 6, pp. 1451–1467, Apr. 2004.

[60] T. Shimokawa and M. Tsuboi, “Atomic-scale intergranular crack-tip plasticity in tilt grain boundaries acting as an effective dislocation source,” Acta Mater., vol. 87, pp. 233–247, Apr. 2015.

[61] D. Farkas, “Atomistic simulations of metallic microstructures,” Curr. Opin. Solid State Mater. Sci., vol. 17, no. 6, pp. 284–297, Dec. 2013.

[62] A. Stukowski, “Visualization and analysis of atomistic simulation data with OVITO–the Open Visualization Tool,” Model. Simul. Mater. Sci. Eng., vol. 18, no. 1, p. 15012, 2010.

[63] A. Stukowski, “Structure identification methods for atomistic simulations of crystalline materials,” Model. Simul. Mater. Sci. Eng., vol. 20, no. 4, p. 45021, 2012.

[64] P. M. Larsen, S. Schmidt, and J. Schiøtz, “Robust structural identification via polyhedral template matching,” Model. Simul. Mater. Sci. Eng., vol. 24, no. 5, p. 55007, 2016.

[65] C. L. Kelchner, S. J. Plimpton, and J. C. Hamilton, “Dislocation nucleation and defect structure during surface indentation,” Phys. Rev. B, vol. 58, no. 17, pp. 11085–11088, Nov. 1998.

[66] P. Features, “HAYNES ® 282 ® alloy Principal Features,” 2019.

[67] M. S. A. Karunaratne, S. Kyaw, A. Jones, R. Morrell, and R. C. Thomson, “Modelling the coefficient of thermal expansion in Ni-based superalloys and bond coatings,” J. Mater. Sci., vol. 51, no. 9, pp. 4213–4226, 2016.

[68] G. P. Potirniche, J. L. Hearndon, M. F. Horstemeyer, and X. W. Ling, “Lattice orientation effects on void growth and coalescence in fcc single crystals,” Int. J. Plast., vol. 22, no. 5, pp. 921–942, 2006.

[69] I. A. Khan and V. Bhasin, “On the role of secondary voids and their distribution in the mechanism of void growth and coalescence in porous plastic solids,” Int. J. Solids Struct., vol. 108, pp. 203–215, Mar. 2017.

[70] H. A. Wu, “Molecular dynamics simulation of loading rate and surface effects on the elastic bending behavior of metal nanorod,” Comput. Mater. Sci., vol. 31, no. 3–4, pp. 287–291, Nov. 2004.

[71] J. Marian, J. Knap, and M. Ortiz, “Nanovoid deformation in aluminum under simple shear,” Acta Mater., vol. 53, no. 10, pp. 2893–2900, Jun. 2005.

[72] J. P. Wang, Z. F. Yue, Z. X. Wen, D. X. Zhang, and C. Y. Liu, “Orientation effects on the tensile properties of single crystal nickel with nanovoid: Atomistic simulation,” Comput. Mater. Sci., vol. 132, pp. 116–124, May 2017.

[73] Z. X. Wen, J. Wang, Y. W. Wu, K. J. Zhou, and Z. F. Yue, “Atomistic simulation analysis of the effects of void interaction on void growth and coalescence in a metallic system,” Curr. Appl. Phys., vol. 18, Mar. 2018.

[74] N.-L. Li, W.-P. Wu, and K. Nie, “Molecular dynamics study on the evolution of interfacial dislocation network and mechanical properties of Ni-based single crystal superalloys,” Phys. Lett. A, vol. 382, no. 20, pp. 1361–1367, May 2018.

[75] J. Yu, S. Zhang, Q. Zhang, R. Liu, M. Tang, and X. Li, “Simulation study and experiment verification of the creep mechanism of a nickel-based single crystal superalloy obtained from microstructural evolution,” RSC Adv., vol. 6, no. 109, pp. 107748–107758, 2016.

[76] A. K. Mukherjee, J. E. Bird, and J. E. Dorn, “Experimental correlations for high-temperature creep,” 1968.

[77] K. Nie, W.-P. Wu, X.-L. Zhang, and S.-M. Yang, “Molecular dynamics study on the grain size, temperature, and stress dependence of creep behavior in nanocrystalline nickel,” J. Mater. Sci., vol. 52, no. 4, pp. 2180–2191, 2017.

[78] S. Saha and M. Motalab, “Nature of creep deformation in nanocrystalline Tungsten,” Comput. Mater. Sci., vol. 149, pp. 360–372, Jun. 2018.

[79] E. O. Hall, “The Deformation and Ageing of Mild Steel: II Characteristics of the L ders Deformation,” Proc. Phys. Soc. Sect. B, vol. 64, no. 9, pp. 742–747, 1951.

[80] PETCH and N. J., “The Cleavage Strength of Polycrystals,” J. Iron Steel Inst., vol. 174, pp. 25–28, 1953.

[81] S. J. A. Koh, H. P. Lee, C. Lu, and Q. H. Cheng, “Molecular dynamics simulation of a solid platinum nanowire under uniaxial tensile strain: Temperature and strain-rate effects,” Phys. Rev. B, vol. 72, no. 8, p. 85414, Aug. 2005.

[82] M. A. Meyers, A. Mishra, and D. J. Benson, “Mechanical properties of nanocrystalline materials,” Prog. Mater. Sci., vol. 51, no. 4, pp. 427–556, May 2006.

[83] J. R. Greer and J. T. M. De Hosson, “Plasticity in small-sized metallic systems: Intrinsic versus extrinsic size effect,” Prog. Mater. Sci., vol. 56, no. 6, pp. 654–724, Aug. 2011.

[84] J. R. Greer, D. Jang, and X. W. Gu, “Exploring Deformation Mechanisms in

Nanostructured Materials," JOM, vol. 64, no. 10, pp. 1241–1252, 2012.

[85] V. Yamakov, D. Wolf, S. R. Phillpot, A. K. Mukherjee, and H. Gleiter, "Dislocation processes in the deformation of nanocrystalline aluminium by molecular-dynamics simulation," Nat. Mater., vol. 1, no. 1, pp. 45–49, 2002.

[86] H. Van Swygenhoven, P. M. Derlet, and A. Hasnaoui, "Atomic mechanism for dislocation emission from nanosized grain boundaries," Phys. Rev. B, vol. 66, no. 2, p. 24101, Jun. 2002.

[87] H. Van Swygenhoven and P. M. Derlet, "Grain-boundary sliding in nanocrystalline fcc metals," Phys. Rev. B, vol. 64, no. 22, p. 224105, Nov. 2001.

[88] J. Monk and D. Farkas, "Tension–compression asymmetry and size effects in nanocrystalline Ni nanowires," Philos. Mag., vol. 87, no. 14–15, pp. 2233–2244, May 2007.

[89] D. Farkas, S. Mohanty, and J. Monk, "Strain-driven grain boundary motion in nanocrystalline materials," Mater. Sci. Eng. A, vol. 493, no. 1–2, pp. 33–40, Oct. 2008.

[90] M. Ke, S. A. Hackney, W. W. Milligan, and E. C. Aifantis, "Observation and measurement of grain rotation and plastic strain in nanostructured metal thin films," Nanostructured Mater., vol. 5, no. 6, pp. 689–697, Aug. 1995.

[91] G. Y. Wang, P. K. Liaw, Y. Yokoyama, A. Inoue, and C. T. Liu, "Fatigue behavior of Zr-based bulk-metallic glasses," Mater. Sci. Eng. A, vol. 494, no. 1–2, pp. 314–323, Oct. 2008.

[92] W. . Ashmawi and M. . Zikry, "Single void morphological and grain-boundary effects on overall failure in F.C.C. polycrystalline systems," Mater. Sci. Eng. A, vol. 343, no. 1–2, pp. 126–142, Feb. 2003.

[93] H. N. Jarmakani et al., "Molecular dynamics simulations of shock compression of nickel: From monocrystals to nanocrystals," Acta Mater., vol. 56, no. 19, pp. 5584–5604, Nov. 2008.

[94] E. M. Bringa et al., "Ultrahigh Strength in Nanocrystalline Materials Under Shock Loading," Science (80-.)., vol. 309, no. 5742, pp. 1838 LP – 1841, Sep. 2005.

[95] H. Van Swygenhoven and J. R. Weertman, "Deformation in nanocrystalline metals," Mater. Today, vol. 9, no. 5, pp. 24–31, May 2006.

[96] N. Q. Vo, R. S. Averback, P. Bellon, and A. Caro, "Limits of hardness at the nanoscale:

Molecular dynamics simulations," Phys. Rev. B, vol. 78, no. 24, p. 241402, Dec. 2008.

[97] Y. Tang, E. M. Bringa, and M. A. Meyers, "Inverse Hall–Petch relationship in nanocrystalline tantalum," Mater. Sci. Eng. A, vol. 580, pp. 414–426, Sep. 2013.

[98] H. Jónsson and H. C. Andersen, "Icosahedral Ordering in the Lennard-Jones Liquid and Glass," Phys. Rev. Lett., vol. 60, no. 22, pp. 2295–2298, May 1988.

[99] A. S. Clarke and H. Jónsson, "Structural changes accompanying densification of random hard-sphere packings," Phys. Rev. E, vol. 47, no. 6, pp. 3975–3984, Jun. 1993.

[100] H. J. Frost and M. F. Ashby, "Deformation mechanism maps," Pergamon Press. New york, vol. 20, pp. 887–897, 1982.

[101] B. Burton and G. W. Greenwood, "The Contribution of Grain-Boundary Diffusion to Creep at Low Stresses," Met. Sci. J., vol. 4, no. 1, pp. 215–218, Jan. 1970.

[102] M. Meraj and S. Pal, "The Effect of Temperature on Creep Behaviour of Porous (1 at.%) Nano Crystalline Nickel," Trans. Indian Inst. Met., vol. 69, no. 2, pp. 277–282, 2016.

[103] R. L. Coble, "A Model for Boundary Diffusion Controlled Creep in Polycrystalline Materials," J. Appl. Phys., vol. 34, no. 6, pp. 1679–1682, Jun. 1963.

[104] C. Herring, "Diffusional Viscosity of a Polycrystalline Solid," J. Appl. Phys., vol. 21, no. 5, pp. 437–445, May 1950.

[105] F. R. N. Nabarro, "Deformation of Single Crystals by the Motion of Single Ions," in Report of a Conference on the Strength of Solids (Bristol),(The Physical Soc., London, 1948), pp. 75–90.

[106] A. H. Chokshi, A. K. Mukherjee, and T. G. Langdon, "Superplasticity in advanced materials," Mater. Sci. Eng. R Reports, vol. 10, no. 6, pp. 237–274, Sep. 1993.

APPENDIX

A. LAMMPS input script

1. Structural minimization script

```
units          metal
boundary       p p p
atom_style     atomic
read_data poly4_5

mass     1  58.69
mass     2  26.98

# ---------- Calling the potential file----------------------
pair_style     eam/alloy
pair_coeff     * * NiAl2.txt Ni Al

delete_atoms overlap 1.9 all all

# ---------- Running NPT simulation----------------
timestep       0.0001
#velocity       all create 300 4928459 dist gaussian
dump           melt all atom 100 poly_dump_iso.dat
#restart        1000 restart.*
thermo         10
thermo_style    custom step temp etotal pe press vol lx ly lz pxx pyy pzz pyz pxz pxy

minimize 0.0 1.0e-8 1000 100000
#fix            1 all npt temp 300 300 0.1 iso 0.0 0.0 0.1
#run            5000
```

2. NPT simulation script

```
units          metal
boundary       p p p
atom_style     atomic
read_data NiAl_2

mass     1  58.69
mass     2  26.98

# ---------- Calling the potential file----------------------
```

```
pair_style      eam/alloy
pair_coeff      * * NiAl.txt Ni Al
# ---------- Running NPT simulation----------------
timestep        0.002
velocity        all create 300 4928459 dist gaussian
dump            melt all atom 100 NiAl_dump_aniso.dat
#restart        1000 restart.*
thermo          100
thermo_style    custom step temp etotal pe press vol lx ly lz pxx pyy pzz pyz pxz pxy
fix             1 all npt temp 300 300 0.1 iso 0.0 0.0 0.1
run             5000
```

3. Uniaxial compressive loading simulation script

```
# ------------------------ INITIALIZATION ----------------------------
units metal
dimension3
boundaryppp
atom_styleatomic
#variable latparam equal 3.52

# ----------------------- ATOM DEFINITION ----------------------------
#latticefcc ${latparam}
#regionwhole block 0 30 0 30 0 30
#create_box1 whole
#regionupper block INF INF INF INF INF INF units box
#lattice fcc ${latparam} orient x 1 0 0 orient y 0 1 0 orient z 0 0 1
#create_atoms1 region whole
read_data mega

region void sphere 13.0 13.0 13.0 5 side in
delete_atoms region void

# ------------------------ FORCE FIELDS -----------------------------
pair_styleeam/alloy
pair_coeff* * NiAl2.txt Ni Al

# ------------------------- SETTINGS ---------------------------------
compute csym all centro/atom fcc
compute peratom all pe/atom

#########################################
# EQUILIBRATION
reset_timestep0
```

```
timestep 0.001
velocity all create 300 12345 mom yes rot no
fix 1 all npt temp 300 300 1 iso 0 0 1 drag 1

# Set thermo output
thermo 1000
thermo_style custom step lx ly lz press pxx pyy pzz pe temp

# Run for at least 10 picosecond (assuming 1 fs timestep)
run 20000
unfix 1

# Store final cell length for strain calculations
variable tmp equal "lx"
variable L0 equal ${tmp}
print "Initial Length, L0: ${L0}"

##########################################
# DEFORMATION
reset_timestep0

fix1 all npt temp 300 300 1 y 0 0 1 z 0 0 1 drag 1
variable srate equal 5.0e9
variable srate1 equal "-v_srate / 1.0e12"
fix2 all deform 1 x erate ${srate1} units box remap x
#fix 2 all deform 1 x erate 0.01 units box remap x

# Output strain and stress info to file
# for units metal, pressure is in [bars] = 100 [kPa] = 1/10000 [GPa]
# p2, p3, p4 are in GPa
variable strain equal "(lx - v_L0)/v_L0"
variable p1 equal "v_strain"
variable p2 equal "-pxx/10000"
variable p3 equal "-pyy/10000"
variable p4 equal "-pzz/10000"
fix def1 all print 100 "${p1} ${p2} ${p3} ${p4}" file Ni_comp_100.def1.txt screen no

dump myDump all atom 200 dumppure1.atom


# Display thermo
thermo 1000
thermo_stylecustom step v_strain temp v_p2 v_p3 v_p4 ke pe press

run50000
```

```
########################################
# SIMULATION DONE
print "All done"
```

4. Edge dislocation generation script

```
# Variable definitions
variable initTemp equal 300.            # desired temperature
variable sigma equal 15000.         # applied stress in bar
variable material string Ni     # material symbol
variable atom_file string Ni.atoms.fcc.perfect.cubic # the configuration was generated by SG
with the preprocessor dislocation.f90

variable equilTime equal 10000          # number of increment to equilibrate the temperature
variable runTime equal 150000       # number of increment to calibrate the velocity
variable energyConv equal 1602191.7     # conversion factor


dimension 3
boundary p s p
units metal
atom_style atomic
read_data ${atom_file}

# store initial position of bottom and top planes along y
variable tmp0 equal "ylo+14."
variable ylo0 equal ${tmp0}
variable tmp1 equal "yhi-14.5"
variable yhi0 equal ${tmp1}

# variable for dumping
variable ymid1 equal "0.5*ylo + 0.5*yhi - 30.0"
variable ymiddlenegative equal ${ymid1}
variable ymid2 equal "0.5*(ylo + yhi) + 30.0"
variable ymiddlepositive equal ${ymid2}

# define potential
pair_style   meam
pair_coeff   * * ${material}.library.meam ${material} ${material}.parameter.meam ${material}

neighbor  2.0 bin
neigh_modify delay 5
# definition of the upper and lower blocks
region upper block INF INF ${yhi0} INF INF INF units box
```

```
region lower block INF INF INF ${ylo0} INF INF units box

# definition of the group
group upper region upper
group lower region lower
group mobile subtract all upper lower

# fix top and botton group
fix 1 lower setforce 0.0 0.0 NULL
fix 2 upper setforce 0.0 0.0 NULL

# compute specific quantities
compute pot_energy all pe/atom
compute stress all stress/atom NULL

dump 1 all custom 1000 dump.minimize id x y z c_pot_energy

# create the dislocation
timestep 0.010
minimize 0.0 1.0e-8 10000 100000

#########################################################
# step 2: equilibrate the temperature         #
#########################################################
timestep 0.001
undump 1
reset_timestep 0
unfix 1
unfix 2
# define temperature
compute temp1 mobile temp

# initialize the velocities
velocity mobile create ${initTemp} 16723 units box
velocity mobile zero linear
velocity mobile zero angular

# equilibrate the temperature
fix 1 mobile nve
fix 2 mobile temp/rescale 1 ${initTemp} ${initTemp} 1.0 0.5
fix_modify 2 temp temp1

# boundary condition
fix 3 lower setforce 0.0 0.0 NULL
fix 4 upper setforce 0.0 0.0 NULL
```

```
thermo 100
thermo_modify temp temp1

thermo_style custom step pe ke temp pxx pyy pzz pxy pyz pxz
dump 1 all custom 10000 dump.equilibration id x y z c_pot_energy c_stress[1] c_stress[2]
c_stress[3] c_stress[4] c_stress[5] c_stress[6]

run ${equilTime}


################################################################################
##########################
# step 3: MD at finite temperatute and with constant force                     #
# force (eV/angstrom) = stress (bar) * S (angstrom*angstrom) / (number of atoms in upper) /
1602191.7) #
################################################################################
##########################
unfix 1
unfix 2
unfix 3
unfix 4
undump 1
uncompute temp1
reset_timestep 0

timestep 0.002

# define the force to apply
variable nupper equal count(upper)
variable nuper1 equal ${nupper}
print "number of atoms in upper == ${nupper}"
variable tmp2 equal "lx"
variable tmp3 equal "lz"

variable tmp4 equal v_tmp2*v_tmp3/v_nupper*v_sigma/v_energyConv
variable appforce equal ${tmp4}

# define temperature
compute temp1 mobile temp

# define velocity on boundary
velocity upper set 0. 0. 0. units box
velocity lower set 0. 0. 0. units box

# define boundary conditions
fix 1 upper setforce NULL 0. NULL
```

```
fix 2 lower setforce 0. 0. NULL
fix 3 upper aveforce ${appforce} 0. 0.
fix 4 upper rigid group 1 upper

# no temperature control
fix 5 mobile nve

thermo 100
thermo_modify temp temp1

dump 1 all custom 5000 dump.shear id x y z
dump 2 all custom 500 dump.shear.unwrap id xu yu zu

run ${runTime}
```

B. Python code

```
from ovito import *
import numpy as np
import os

assert(version[0] >= 2 and version[1] >= 7)


def get_dislocation_position(frame, input, output):

    x_extent = output.cell.matrix[0,0]
    positions = output.particle_properties.position.marray #.copy()

    # Eliminate all periodic images
    positions[(positions[:,0] > x_extent),0] = positions[(positions[:,0] > x_extent),0] - x_extent
    # Edit positions to put dislocation all on same side
    if frame == 0:
        global core_spread
        core_spread = np.max(positions[:,0]) - np.min(positions[:,0])
        if core_spread > 0.5*x_extent:
            core_spread = None
    elif core_spread:
        ref = positions[0,0]
        for i,p in enumerate(positions):
            if i == 0:
                continue
            if (p[0] - ref) > core_spread*1.3:
                p[0] -= x_extent
```

```
            ref = np.mean(positions[0:(i+1),0])
        dislocation = np.mean(positions,0)[0]
        timestep = output.attributes['Timestep']

        while (pos[frame - 1] - dislocation) > 0.25*x_extent:
            dislocation += x_extent

        with open('posVStime.txt','a+') as f:
            f.write('{}\t{}\n'.format(timestep, dislocation))

        time[frame] = timestep
        pos[frame] = dislocation

    def initialize_data(num):
        global time, pos, core_spread
        time = np.zeros(num)
        pos = np.zeros(num)
        core_spread = None

        if os.path.exists('posVStime.txt'):
            data = np.loadtxt('posVStime.txt')
            time.put(range(len(data[:,0])),data[:,0])
            pos.put(range(len(data[:,1])),data[:,1])


    # If run from the command line setup required modifiers
    if __name__ == "__main__":

        from sys import argv

        if len(argv) < 2:
            raise   Exception("Filename required as an argument.")

        filename = argv[-1]

        # Parse input arguments
        # Default values
        if len(argv) > 2:
            keyargs = argv[1:-1]
            i = 0
            while (i < len(keyargs)):
                key = keyargs[i].split('-')[1]
                i += 1
                if (key is "h") or (key is "help"):
                    print("Usage: ovitos dis_mobility.py [OPTIONS] [FILENAME]\n\t-h,help\tThis help
    message\n")
```

```
        else:
            raise Exception("Unknown option: " + key)

# ### Setup ovitos ###
# Import file
if len([s for s in filename if s == '*']) > 0:
    node = io.import_file(filename)
else:
    node = io.import_file(filename, multiple_frames=True)

# Create CNA or PTM modifier
#   if version[1] = 7:
    #structure = modifiers.CommonNeighborAnalysisModifier()
    #elif version[1] > 7:
structure = modifiers.PolyhedralTemplateMatchingModifier()
node.modifiers.append(structure)
node.compute()

# Estimate bulk structure
nfcc = node.output.attributes['PolyhedralTemplateMatching.counts.FCC']
nbcc = node.output.attributes['PolyhedralTemplateMatching.counts.BCC']
nhcp = node.output.attributes['PolyhedralTemplateMatching.counts.HCP']
struct_ID = np.argmax([nfcc,nhcp,nbcc]) + 1

# Add expression select
y_extent = node.output.cell.matrix[1,1]
bulk = modifiers.SelectExpressionModifier(
    expression = 'StructureType == {} || Position.Y < {} || Position.Y > {}'.format(
        struct_ID,
        y_extent/2.0 - 30.0,
        y_extent/2.0 + 30.0))
node.modifiers.append(bulk)

# Add delete selected
delete = modifiers.DeleteSelectedParticlesModifier()
node.modifiers.append(delete)

numframes = node.source.num_frames
frames = range(numframes)

initialize_data(numframes)

for frame in frames:
    if frame < numframes:
        dataset.anim.current_frame = frame # Advance frame.
    else:
```

```
    continue
node.compute()
get_dislocation_position(frame, node.output, node.output)
```